Mono-static and Bi-static MIMO Radar: Targets Localisation

by

Nadeem Dar

A Thesis submitted in fulfilment of requirements for
the degree of Doctor of Philosophy (PhD)
and
the Diploma of Imperial College London (DIC)

July 2024

Supervisor: Prof. A. Manikas

Imperial College London

Department of Electrical and Electronic Engineering

Imperial College
London

Department of Electrical and Electronic Engineering

Abstract

This thesis explores the application of multiple-input multiple-output (MIMO) radar technology for enhanced parameter estimation in both monostatic and bistatic configurations. It leverages the combined power of spatial and waveform diversities, along with basic and extended array manifolds, to achieve superior performance.

It begins with an overview of recent advancements in MIMO radar technology, introducing and exploring core concepts critical for understanding the system's operation. The focus then shifts to a Saab monostatic MIMO experimental radar system. By modelling system blocks from transmitter to receiver, it analyses the performance of classical parameter estimation algorithms and compares these with novel virtual MIMO algorithms, highlighting their potential for improvement.

The thesis proposes innovative subspace-based algorithms designed for bistatic MIMO radar systems. These algorithms utilise fast and slow time coding to achieve waveform diversity and an extended observation space through extended manifolds. This enables accurate target parameter estimation even in environments with significant clutter and noise. The performance of these algorithms is evaluated using root-mean-square error (RMSE) in Monte Carlo simulations.

Furthermore, the thesis examines the theoretical performance limitations of the antenna arrays employed, comparing their performance with a uniform circular array (UCA) to highlight the trade-offs associated with different array geometries.

This thesis introduces novel algorithms and insights that advance MIMO radar parameter estimation, paving the way for improved target localisation in complex scenarios.

Declaration of Originality

I hereby declare that this thesis is my own work. Where other sources of information have been used, they have been acknowledged.

Copyright Declaration

[1]This PhD research was supported by Saab Innovation Centre UK under contract EESB P78823. Copies and redistribution of the work must adhere to the terms and conditions specified in the contract.

Acknowledgements

بسم الله، الحمد لله، والصلاة والسلام على رسول الله. أما بعد

With profound gratitude, I extend my heartfelt thanks to Allah, the Most Gracious and Most Merciful, for granting me the energy and opportunities that have enabled me to become a member of this esteemed institution and research group. This research endeavour would not have been feasible without the generous funding provided by Saab Group, Sweden/UK. I am deeply appreciative of the unwavering support and encouragement from Prof. Anders Silander and Mrs Malin Svahn at Saab, whose guidance has been invaluable throughout this journey.

I am indebted to Prof. Manikas, my supervisor, whose mentorship has been instrumental. His consistent support and wisdom have helped me navigate the complexities of this research endeavour. My deepest gratitude extends to my parents, whose boundless love, care, and sacrifices have profoundly shaped the person I am today. Their unwavering commitment to my well-being has been the cornerstone of my journey. However, it is with a heavy heart that I reflect on the passing of my mother after a courageous battle with cancer, which occurred just before I embarked on the journey of writing my thesis. Her absence during this pivotal time is deeply felt, and I carry her memory with me as a source of strength and inspiration.

To my beloved wife, Saima, whose unwavering companionship, support, and encouragement have been my refuge during moments of adversity. Her presence has served as a guiding light, steering me through life's challenges. My children, Moeed and Muskaan, have been a constant source of inspiration. Their radiant smiles provide me with the motivation to lead by example and strive for excellence. They are the silent champions behind my perseverance.

Contents

List of Figures

List of Tables

Publications Related to this Thesis

The following papers[2] were published or submitted for publication during the PhD:

1. Y. Liu, N. Dar and A. Manikas, "Multi-target Parameter Estimation in Bistatic MIMO Radar," 2022 IEEE International Symposium on Phased Array Systems & Technology (PAST), Waltham, MA, USA, October 10-14, 2022, pp. 01-06, doi: 10.1109/PAST49659.2022.9975001.

2. N. Dar and A. Manikas, “Multitarget Bistatic MIMO Radar.” 2024, [Online]. Available: https://arxiv.org/abs/2411.02072.

[2] Note that paper [1] is related to Chapter 3 and paper [2] is related to Chapter 4

Notation

a, A	Scalar
$\underline{a}$, $\underline{A}$	Column vector
$\mathbf{a}$, $\mathbb{A}$	Matrix
$(\cdot)^T, (\cdot)^H$	Transpose and Hermitian transpose
$(\cdot)^*, (\cdot)^\#$	Conjugate and pseudo-inverse
$\exp(\underline{A})$	Element by element exponential of vector $\underline{A}$
$\underline{A}^b$	Element by element power of vector $\underline{A}$
$\text{row}_k(\mathbb{A})$	k^{th} row of the matrix $\mathbb{A}$
$\|A\|$	Absolute value or magnitude of A
$\\|\underline{A}\\|$	Euclidean norm of vector $\underline{A}$
$\text{trace}(\mathbb{A})$	Sum of the diagonal elements of matrix $\mathbb{A}$
$\mathcal{E}\{\cdot\}$	Expectation operator
$\odot, \otimes$	Hadamard and Kronecker product
$\oplus$	Kronecker sum
$\circledast$	Convolution
$\forall$	For all
$\underline{0}_N$	Column vector of N zeros
$\underline{1}_N$	Column vector of N ones
$\mathbb{I}_N$	$N \times N$ Identity matrix
$\mathbb{O}_{N \times M}$	$N \times M$ matrix of zeros
$\mathcal{R}$, $\mathcal{C}$	Set of real & complex numbers respectively
$\underline{\text{diag}}(\mathbb{A})$	A column vector of the diagonal elements of matrix $\mathbb{A}$
$\text{diag}(\underline{a})$	A square matrix with the elements of $\underline{a}$ on the main diagonal and zeros elsewhere

Abbreviations

ADC	Analogue-to-Digital Converter
AIC	Akaike Information Criteria
AML	Approximate Maximum Likelihood
APES	Amplitude and Phase Estimation
AWGN	Additive White Gaussian Noise
CAML	Capon and AML algorithms
CAPES	Capon and APES algorithms
CDMA	Code Division Multiple Access
CRB	Cramer Rao Bound
DAC	Digital-to-Analogue Converter
DOA	Direction of Arrival
DOD	Direction of Departure
DOF	Degrees of Freedom
ESPRIT	Estimation of Signal Parameters via Rotation Invariance Techniques
KR	Khatri-Rao
LHS	Left Hand Side
LMS	Least Mean Squares
LOS	Line of Sight
LRAM	L-band Rocket Artillery Mortar
MDL	Minimum Descriptor Length
MIMO	Multiple-Input Multiple-Output
ML	Maximum Likelihood
MSE	Mean Square Error
MUSIC	MUltiple SIgnal Classification

MVDR	Minimum Variance Distortionless Response
NFR	Near Far Ratio
NLOS	Non-Line of Sight
pdf	probability density function
PN	Pseudo-random Noise
RADAR	Radio Detection And Ranging
RF	Radio Frequency
RHS	Right Hand Side
RMSE	Root Mean Square Error
Rx	Receiver
SCR	Signal-to-Clutter Ratio
SIMO	Single-Input Multiple-Output
SNIR	Signal-to-Noise-plus-Interference Ratio
SNR	Signal-to-Noise Ratio
TDL	Tapped Delay Line
TDMA	Time Division Multiple Access
TOA	Time of Arrival
Tx	Transmitter
UAV	Unmanned Aerial Vehicle
UCA	Uniform Circular Array
ULA	Uniform Linear Array

Chapter 1

Introduction

This chapter introduces radar systems, beginning with a brief history and an overview of various types and classifications. It outlines fundamental radar parameters and concepts, including radar pulses, Pulse Repetition Interval (PRI), the 3D data cube, and fast and slow time samples. The chapter then discusses target parameters such as direction, range, Doppler, and Radar Cross Section (RCS). Key challenges in radar systems, such as detection, localisation, tracking, reception, and classification, are also introduced.

Furthermore, the chapter covers different system configurations, including SISO (Single Input Single Output), SIMO (Single Input Multiple Output), MISO (Multiple Input Single Output), and MIMO (Multiple Input Multiple Output). It explains the role of antenna arrays and array geometries in radar systems. Given that the thesis primarily focuses on monostatic and bistatic radars, a conceptual architecture for these radar types is also presented. Finally, the motivation, problem description, as well as the research objectives and contributions are outlined.

1.1 Overview of Radar Systems

Radar systems have become ubiquitous across a vast array of applications, serving as the lifeblood of national defence, air traffic control, weather forecasting, and autonomous vehicle navigation [1, 2]. Their origin story can be traced back to the early 20th century, with significant advancements driven by the urgency of

World War II. During this conflict, radar played a pivotal role in detecting and tracking enemy aircraft, offering a significant advantage to allied forces [3–5]. Since then, radar technology has undergone a remarkable metamorphosis, evolving from rudimentary continuous-wave (CW) and pulsed radar systems to sophisticated, multi-functional platforms capable of tackling a multitude of tasks with exceptional precision [6, 7].

Beyond military applications, MIMO radar technology is finding increasing use in civilian domains. It is integral to intelligent transportation systems that monitor and manage traffic flow and advanced driver-assistance systems, offering a clearer picture of surroundings for safer autonomous vehicles [8–11]. Additionally, MIMO radars enhance ground-penetrating radar for tasks like infrastructure inspection [12, 13] and detecting landmines or unexploded ordnance [14–16]. The concept of spectrum sharing between radar and communication systems is gaining traction due to the need for efficient utilisation of the limited radio frequency spectrum [17–19]. Furthermore, MIMO radars excel at tracking small objects like drones, making them valuable for airspace security [20–22]. They also contribute detailed weather data on precipitation, wind, and atmospheric conditions, improving weather monitoring and prediction [23–25]. As MIMO radar technology evolves, we can expect even more innovative civilian applications to emerge.

1.1.1 Radar Classifications

Radar systems can be classified in various ways. Figure 1.1 below illustrates a top-level classification hierarchy. If a radar system includes its own transmitter for emitting a probing signal, it is classified as active radar. The radar receiver measures the delays between direct and reflected signal paths to estimate the range to a target. Conversely, a radar system that only includes a receiver is termed passive radar [26]. Passive radar can operate using signals of opertunity, such as TV, radio, or telecom broadcast signals.

The radar architecture presents another significant classification of radar systems. Monostatic radars, the most common type, feature both the transmitter and receiver collocated at a single site, having a common Cartesian system. This

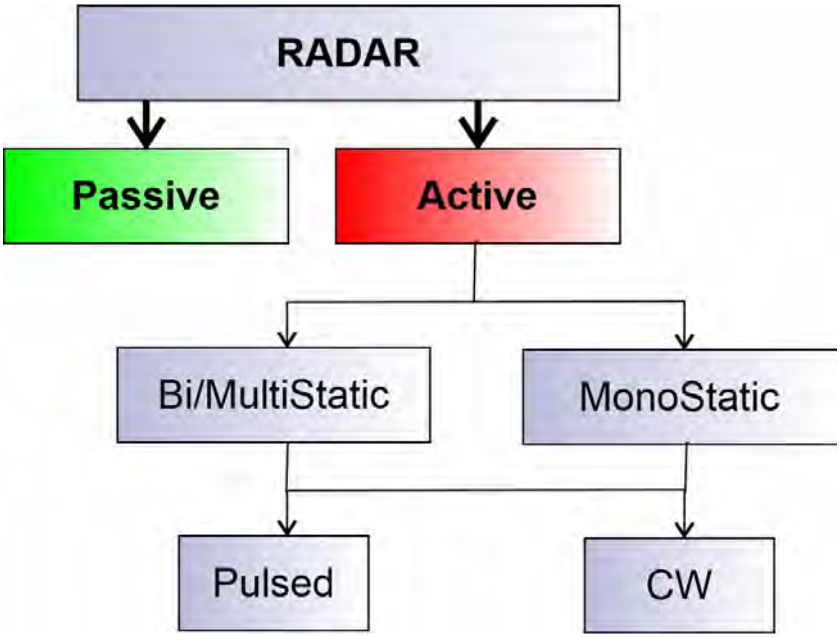

Figure 1.1: Radar classifications

results in identical direction of departure (DOD) and direction of arrival (DOA) [27]. This straightforward architecture facilitates ease of deployment and operation. However, certain applications, such as stealth target tracking in cluttered environments, benefit from bistatic radars. In bistatic radar systems, the transmitter and receiver sites are spatially separated, offering additional insights into stealthy target motion and potentially mitigating the impact of clutter [7]. Moreover, bistatic radars provide enhanced resilience against jamming compared to monostatic radars, as the receiver site's location remains undisclosed [28–30].

Multistatic radar systems introduce a more complex arrangement, leveraging multiple transmitter-receiver pairs distributed across a broad geographical expanse. This distributed configuration not only amplifies coverage, particularly for tracking objects over expansive areas, but also bolsters resistance against jamming and other forms of interference, rendering them indispensable for military applications [26, 31].

The foundational radar systems can be categorised based on their wave transmission characteristics. The CW radar operates by transmitting a continuous sine wave signal, differentiating it from pulsed radar systems that emit discrete bursts [32, 33]. This type of radar typically relies on the Doppler shift principle to detect moving targets. The Doppler shift refers to the change in frequency of a wave caused by the relative motion between the source and observer.

To measure both range and the relative velocity of moving targets, CW radars often employ Frequency Modulated Continuous Wave (FMCW) techniques. In FMCW, the transmitted waveform's frequency is continuously varied over time. This allows for calculating the range based on the time difference between the transmitted signal and the received echo, while the Doppler shift provides information on the target's relative velocity [34]. Additionally, CW radar utilises separate antennas or arrays for transmitting and receiving signals. This separation aids in differentiating between the transmitted and received signals, facilitating accurate target detection and velocity measurement.

The pulsed radars operate by transmitting short bursts of high-powered electromagnetic energy. By measuring the time delay between the transmitted and received pulses, these systems determine the target's range with high accuracy [32].

A radar system (or any wireless system) can also be classified based on the number of sensors/antennas used in both the transmitter (Tx) and receiver (Rx). Figure 1.2 illustrates the configurations for SISO, SIMO, MISO, and MIMO systems. These terms are abbreviations where "S" stands for single, "I" stands for input, "O" stands for output, and "M" stands for multiple. These radar configurations provide system designers with the flexibility to trade-off between various parameters to achieve specific objectives. While passive radars can be classified as bistatic or multistatic, this research focuses solely on active pulsed monostatic and bistatic MIMO radars. This type of radar leverages multiple transmit and receive antennas to exploit spatial diversity. This technique enhances target detection and parameter estimation capabilities by utilising variations in the signal received by each antenna, resulting in a richer dataset for analysis [35–39].

MIMO radar systems are particularly well-suited for challenging scenarios with multiple targets or complex environments where traditional radars might struggle, such as differentiating closely spaced targets or mitigating clutter interference. Leveraging physically separated antenna arrays, these setups unlock the power of angular diversity, achieving a much higher spatial resolution than what's limited by

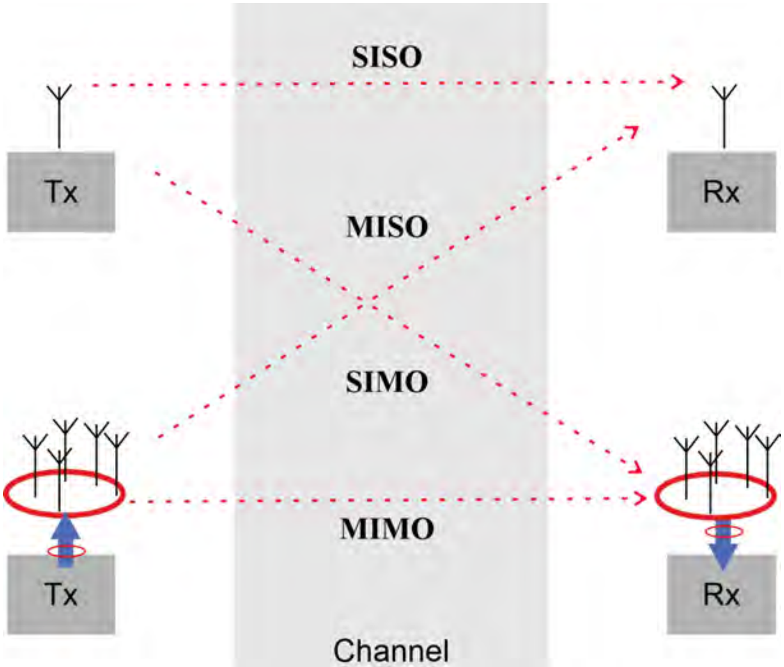

Figure 1.2: Radar classifications based on Tx and Rx channels

the system's bandwidth. This translates to improved detection and classification of smaller objects, such as drones or unmanned aerial vehicles (UAVs) [40–43].

1.1.2 Radar Parameters

In pulsed radar systems, short bursts of electromagnetic energy, called pulses, are transmitted with a duration of T_p. These pulses then reflect off a target in the environment and are received by the radar with a time delay of τ. A crucial concept in pulse radar design is the relationship between pulse duration and bandwidth. The minimum required bandwidth, expressed in Hertz (Hz), to transmit a pulse with duration T_p is inversely proportional to the pulse duration. This relationship can be summarized as: $B \geq \frac{1}{T_p}$, where B represents the minimum required bandwidth.

The concept of pulse duration and bandwidth applies equally to a train of pulses transmitted at regular intervals, known as the PRI. As illustrated in Figure 1.3 (see below), the relationship between the repeated pulses, their autocorrelation function (ACF), and power spectral density (PSD) is described by the Wiener-Khinchin Theorem [44].

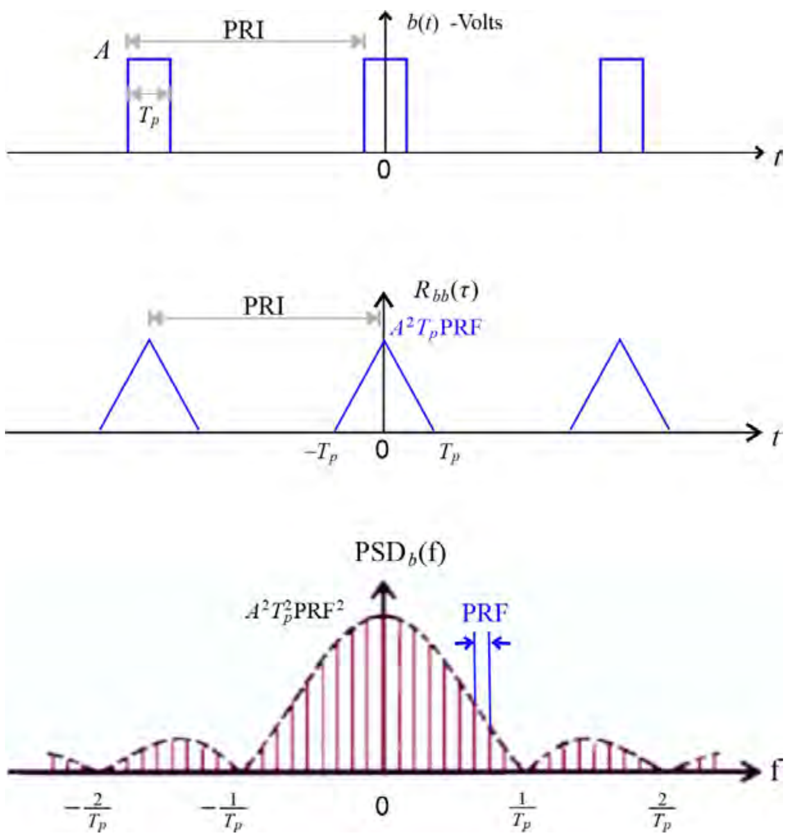

Figure 1.3: Tx pulses, PRI and PSD relationship

The Pulse Repetition Frequency (PRF) is the reciprocal of the PRI, expressed as PRF $= \frac{1}{\text{PRI}}$ and Doppler bandwidth is also equals to PRF i.e. B_{Dop} =PRF. The vertical axis on the PSD plot represents the power spectral density, while the horizontal axis represents frequency. The figure prominently displays discrete lines on the PSD at specific positions: 0, ±PRF, ±2PRF, and so on. These lines correspond to the harmonics of the PRF and arise due to the periodic nature of the pulse train.

The concept of Doppler shift, which is crucial for target velocity estimation, is also relevant here. The figure suggests that the Doppler information is confined within the range of -PRF/2 to +PRF/2. This interval is often referred to as the Doppler ambiguity interval. It essentially represents the range of target velocities that can be uniquely distinguished by the radar system, given the chosen PRF. Values outside this interval will appear aliased within the -PRF/2 to +PRF/2 range.

The baseband signal, denoted as $b(t)$, representing this pulse train, has a discrete PSD with the shape of a sinc function squared. This results from the periodic nature of the pulse train. Due to this repetition, the Fourier Transform (FT) of $b(t)$ gives rise to a "comb" function, a series of impulses spaced at multiples of the PRF weighted by a sinc square function. Squaring the magnitude of the FT, which provides the power distribution across frequencies, yields the PSD(f), representing the spectrum of the baseband signal $b(t)$. This PSD plot we discussed previously represents the signal in the baseband. When these pulses are modulated with a carrier frequency, F_c, the entire spectrum of the signal, including the discrete lines from the pulse repetition, is shifted by F_c. As a result, the center of the spectrum moves from zero frequency to F_c.

The duration of the transmitted pulse, denoted by T_p, directly affects the radar's range resolution. This relationship can be expressed as $\Delta R \geq \frac{cT_p}{2}$, where ΔR is the range resolution, c is the speed of light, and the greater than or equal to sign ($\geq$) indicates a theoretical minimum. In simpler terms, shorter pulses provide better range resolution, allowing the radar to distinguish between targets that are closer together.

However, there's a trade-off: shorter pulses also have a shorter power-time integral. This means the target is illuminated for a shorter duration, which can reduce the maximum detectable range. To address this limitation, pulse compression techniques are employed. These techniques utilise a wider pulse (with longer potential range) that is modulated by a pseudo–random noise (PN) code sequence. This code sequence has a much shorter chip interval, T_c. By employing the PN code, the wider pulse's power is effectively distributed across the shorter chip intervals, enabling both long range and improved range resolution.

A MIMO radar receiver continuously collects data snapshots for each of its N receive streams. These snapshots are acquired at a sampling interval denoted by T_s. For simplicity, we assume that the sampling interval is equal to the chip interval ($T_s = T_c$). However, in practice, the chip interval can be oversampled by a factor of q ($T_s = \frac{T_c}{q}$).

Each PRI contains L snapshots, also referred to as fast-time samples. These represent the received signal variations within a single PRI. A collection of N_{PRI}

PRIs is then assembled into a frame, also known as slow-time samples. The size of the frame, N_{PRI}, is determined by the coherent processing interval (CPI). The CPI represents the time interval over which a target can be assumed to be stationary.

The receiver gathers these snapshots and assembles them into a three-dimensional data cube, as illustrated in Figure 1.4 (see below). This data cube provides a comprehensive representation of the received signals across different receive streams, fast-time variations within a single PRI, and slow-time variations across multiple PRIs.

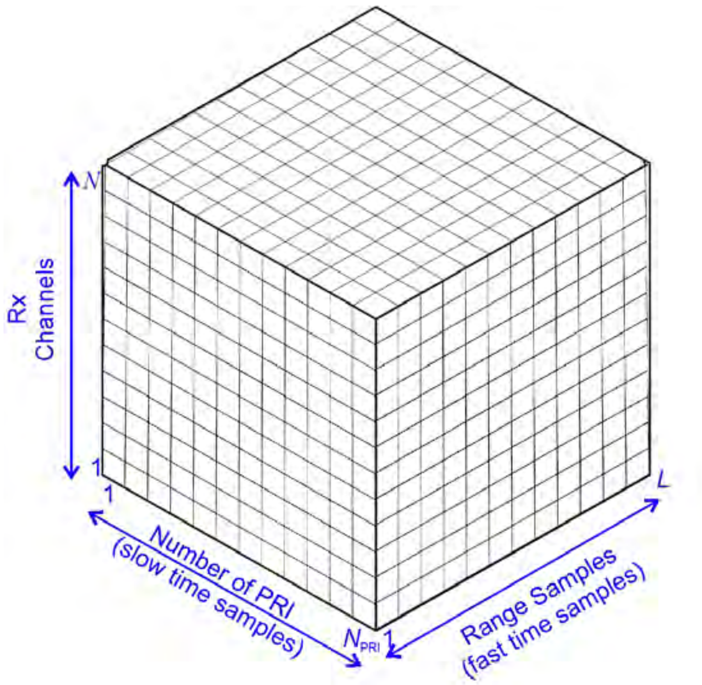

Figure 1.4: Radar Rx 3D data cube

Radars typically operate in environments filled with noise and clutter. Clutter refers to unwanted radar echoes originating from objects other than the target of interest. This can include natural features like mountains, trees, or rain, as well as man-made structures or even flocks of birds. Clutter echoes behave similarly to random noise, with their strength influenced by factors like transmitted power, antenna gain, target range, and the shape and material of the reflecting object.

The radar transmits a signal that illuminates the target. This signal interacts with the target and is then scattered back towards the receiver. In essence, the target behaves like a secondary antenna. The strength of the reflected signal is characterised by a parameter called the RCS [45], denoted by σ. It can be understood as the ratio of the scattered electric field intensity (E_s) from the target to the intensity of the incident electric field (E_i) that illuminated the target.

Another crucial factor to consider is the target's location relative to the radar's antennas or arrays. This is referred to as the near-field and far-field region. When the target range, denoted by R, is greater than a specific distance, it is considered to be in the far-field region. This distance can be calculated as $\frac{D}{\lambda/2}$, where D represents the aperture (size) of the antenna array and λ represents the wavelength of the transmitted signal. Under the far-field assumption, plane wave propagation can be applied for mathematical modelling.

Conversely, if the target is located closer to the radar than the far-field boundary, it is considered to be in the radiating near-field (Fresnel or near-far field) region. In this region, spherical wave propagation is a more accurate model for calculations. The selection of the appropriate wave propagation model (plane wave or spherical wave) is critical for accurate radar signal processing and target parameter estimation, considering the specific geometry of the antenna array and the target's range.

Radar systems address various research problems, including target detection, localisation, classification, tracking, and reception [46]. Detection involves determining the number of targets present within the radar's observed range bin. In a MIMO system utilising a basic array manifold, the achievable detection performance is limited by the dimensionality of the observation space offered by the number of receive antenna elements (N). Consequently, the maximum number of uniquely detectable targets is typically less than N. To enhance detection probability, various signal processing techniques involving pulse and PRI integration are commonly employed. However, this research focuses on leveraging concepts of extended array manifolds to augment the observation space, aiming to surpass the limitations imposed by the number of physical receive antennas.

Following target detection, the next stage involves estimating key target parameters such as range, velocity (derived from Doppler estimates), and direction (including DOD and DOA). These parameters are crucial for target localisation and tracking, especially for non-stationary targets. Target tracking involves continuously estimating a target's state (position and velocity) over time as it moves.

Radar performance can vary significantly depending on the environment. In stationary environments, where the radar platform remains static and targets are assumed to be relatively stable within a short observation window known as the CPI [47], the radar collects multiple snapshots of the scene during each CPI. This repetitive localisation approach, facilitated by CPIs, enhances target position estimation through signal averaging and clutter reduction [48]. Within each CPI, various localisation algorithms estimate the targets' positions based on these snapshots. This approach is utilised in Chapters 2, 3, and 4 of this thesis.

Conversely, in non-stationary environments, such as when the radar is mounted on a moving platform, target locations change rapidly. In these scenarios, tracking algorithms must account for the dynamic environment and update target positions on a snapshot-by-snapshot basis [49]. Classical filtering methods, such as the Kalman filter [50], which statistically estimates the state of a system, combined with a model for target movement, can be used to refine these estimated locations (measurements) and improve tracking accuracy [51]. For example, a comparison of the extended Kalman filter (EKF) tracking with velocity information for MIMO radars, as well as alternative methods applicable to conventional radars, which do not use the velocity vector is presented in [50].

In modern MIMO radar systems, target classification presents another significant challenge, and various studies have explored effective solutions [46, 52–54]. For example, [55] compares the performance of random forest algorithms and deep learning networks for radar target classification based on High-Resolution Radar Range Profile (HRRP) measurements. Additionally, reference [56], demonstrates the use of high-fidelity electromagnetically-simulated RCS responses for target recognition within a cognitive radar platform. However, the focus of this thesis will be on methods beyond target detection, excluding tracking, classification, or recognition.

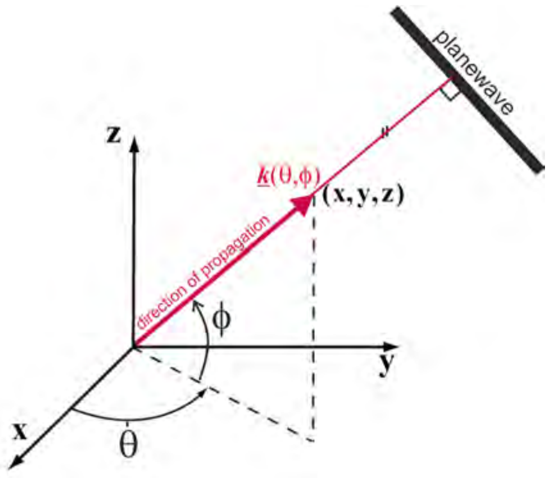

Figure 1.5: Cartesian coordinates of an array and directional parameters.

1.1.3 Antenna Array

An antenna array is a collection of individual antennas operating together as a single unit [57]. These array elements are combined to provide specific advantages, addressing various critical challenges in communication and radar applications. Consider an array of N antennas, and the locations of these antennas in a real 3-D space relative to their local reference point. The antenna reference point $(r_x, r_y, r_z = 0, 0, 0)$ can be defined arbitrarily, but commonly chosen as the centre of the array or the first element of the array for convenience and minimal impact on calculations.

Consider the array operating in the presence of multiple far-field targets. The far-field condition implies that the radius of propagation is sufficiently large such that the wavefronts arriving at the antenna elements can be approximated as plane waves. This simplification is illustrated in Figure 1.5.

The propagation delay between the n-th array element and the array reference point can be expressed as a function of the direction of arrival (θ, ϕ), representing the azimuth and elevation angles, respectively.

1.1.4 Array Manifold

Signals received by the array elements contain both temporal (time-based) and spatial (position-based) information about the surrounding environment [58, 59].

However, this environment is typically contaminated by background noise and sensor noise. Therefore, the main objective of array processing is to extract and then exploit this spatio-temporal information to the fullest extent possible. This allows us to estimate the parameters of interest within the array signal environment [60].

When a signal from k-th target reaches the N receiving antennas (array), it is sampled and converted into a complex vector (for a single sampling interval). This vector, known as the array manifold vector for the k-th target, represents the array's response to a plane wave with unit amplitude arriving from a specific direction (θ, ϕ). The manifold vector for a particular direction encodes all the information about the array's geometry relevant to a wave coming from that direction [60].

By recording how these manifold vectors change with direction, we create a "continuum" (a continuous geometrical object like a curve or surface) within an N-dimensional space. This geometrical object, formed by the locus (collection) of manifold vectors, is called the array manifold. Notably, the array manifold can be calculated (and stored) based solely on the known locations and directional characteristics of the sensors in the array. In essence, the array manifold fully characterizes an array. It acts as a representation of the real array within a complex N-dimensional space [60].

The concept of the array manifold is crucial when considering subspace-based algorithms for estimating target parameters. These algorithms essentially search the array manifold for response vectors that meet specific criteria. For instance, in the MUltiple SIgnal Classification(MUSIC) algorithm, the search focuses on identifying array manifold vectors that are nearly orthogonal to the estimated noise subspace. By finding these "near-orthogonal" vectors, the MUSIC algorithm can pinpoint the directions of the target signals [60]. In this thesis, we primarily focus on subspace algorithms as well.

Modern radars face significant challenges in dense urban environments, where clutter and noise levels are high. A key factor influencing performance in such scenarios is the degrees of freedom (DOF). In a standard radar system with a single antenna element (transmitting and receiving), the DOF are limited to one dimension -the time delay between the transmitted pulse and the received echo. This limitation allows the radar to distinguish targets based solely on their distance or range. The DOF represents the radar's ability to differentiate between multiple targets and are directly linked to the observation space, defined by the number of sensors (N) in the antenna array.

There are two main strategies to improve DOF:

- Increase the number of antennas (streams): This expands the observation space, allowing for the detection of more targets. However, this approach requires more hardware resources, leading to higher system costs and increased power consumption.

- Exploit additional parameters to extend the array manifold: This strategy utilises parameters like PN-codes, Doppler shifts, and polarisation to extend the basic array manifold. In this thesis, we will focus on this approach.

The concept of massive MIMO relies on increased hardware resources (more Tx/Rx streams and antennas) to enhance the system's DOF and estimation performance. In contrast, the extended array concept achieves these benefits with minimal additional hardware, relying instead on increased computational complexity. In this thesis, we adopt the latter approach, assuming that the system cannot add more hardware resources but that additional computational power is available.

Understanding array bounds, which represent the theoretical limits of the array performance influenced by factors like array geometry, noise levels, and signal-to-noise ratio is another critical area of study [31, 61, 62]. By considering these bounds, radar system designers can ensure optimal performance within a realistic constraints [63,64]. For instance, a radar system deployed in an urban environment with high levels of background noise might require a different array configuration compared to a system designed for long-range target detection in open terrain.

1.1.5 Monostatic and Bistatic MIMO Radar

Figure 1.6 presents a conceptual block diagram architecture applicable to both monostatic and bistatic MIMO radar systems. The key difference lies in the Tx and Rx antenna arrays. In monostatic systems, these arrays share a common reference point. Conversely, bistatic systems employ Tx and Rx arrays located at distinct reference points (or locations).

This figure provides a high-level overview of the system's components and their interactions, aiding in understanding the technical workings of any modern radar system. The figure depicts the signal flow through the system's Tx and Rx paths. The left-hand side (LHS) branch represents the Tx path, where signals flow upwards. The right-hand side (RHS) branch represents the Rx path, where signals flow downwards.

The *blue*-arrows in the diagram represent "vectors" of digital signals, indicating that the system is fully digital. This means that the Tx employs a Digital Up-Converter (DUC) and a Digital-to-Analogue Converter (DAC), while the Rx utilises a Digital Down-Converter (DDC) and an Analogue-to-Digital Converter (ADC). These paths will be detailed in the following sections.

The baseband signal vector, $\underline{m}(t)$, originates from Point-A, a crucial component responsible for signal and waveform generation. This block allows for the configuration and generation of various coded waveforms, pulse durations, and PRIs. At Point-Â, the received baseband signal vector, $\underline{x}(t)$, is processed by the "Baseband Signal Processor" (BSP), often referred to as the "brain" of the radar system. The BSP executes various target detection algorithms alongside MIMO localisation and tracking algorithms. This research will focus on the functionalities and potential advancements within the BSP by utilising various Tx waveforms. All the algorithms presented in this thesis will be located in this block.

1.1.5.1 Radar Signal Flow: Tx and Rx

- **Tx, Point-A**: At Point-A, the baseband signal generator creates an $\overline{N} \times 1$ snapshot vector, denoted by $\underline{m}(t_l) \in \mathcal{C}^{N\times 1}, \forall l$, at each time instant t_l (for $l = 1, 2, ...$). This vector controls the timing, frames, and modulation scheme

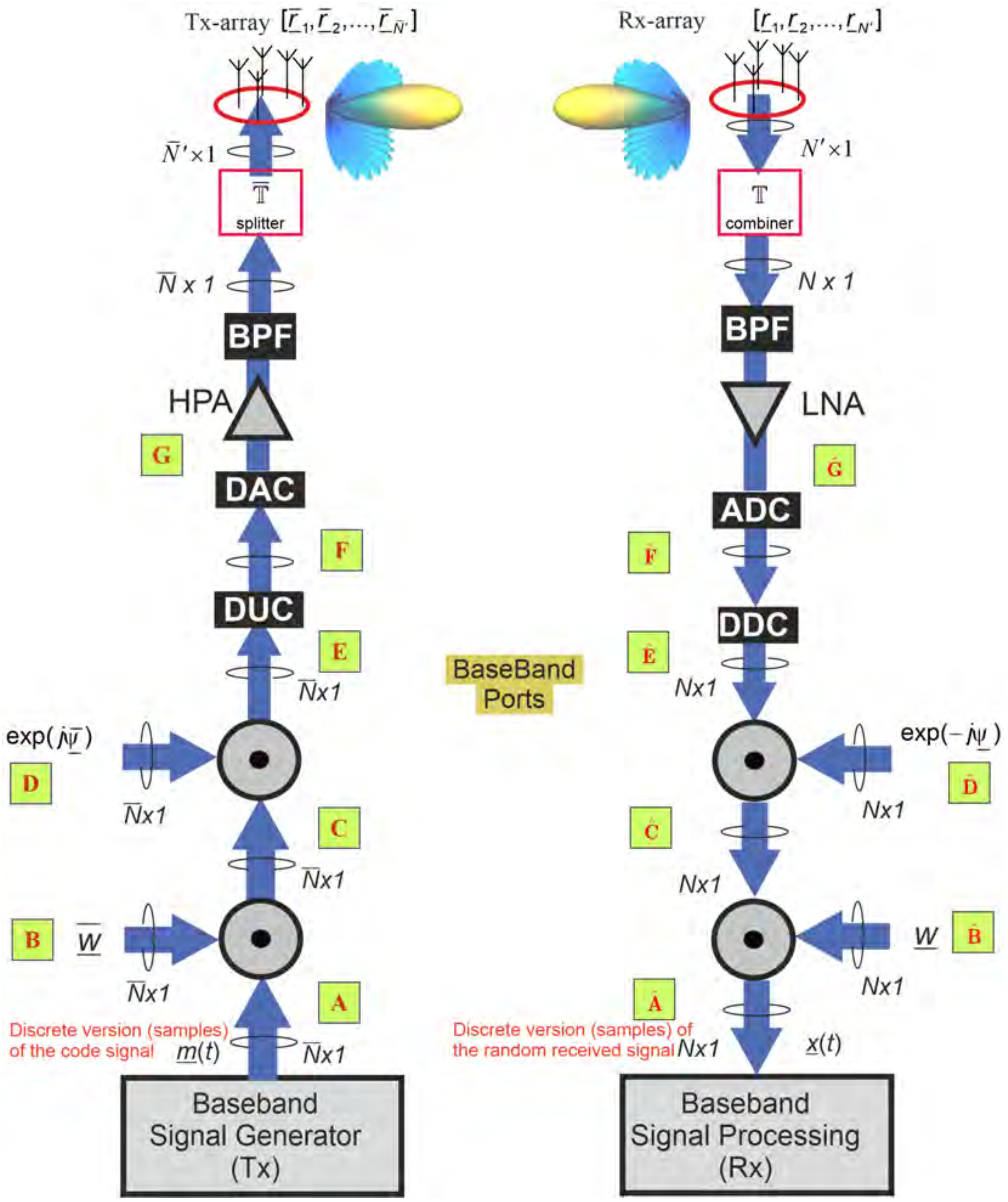

Figure 1.6: Monostatic and bistatic MIMO radar system architecture

depending on the chosen configuration. Additionally, $\overline{N}$ code-signals (e.g., Hadamard codes, PN-codes, gold sequences, m-sequences) are generated and represented by $\underline{m}(t_l)$ for each snapshot l.

- **Tx, Point-B and Point-D**:
  The Tx beamforming at Point-B is represented by the weight-vector $\overline{\underline{w}} \in \mathcal{C}^{\overline{N}\times 1}$ and the steering-vector at Point-D by the vector $\exp(j\overline{\underline{\psi}}) \in \mathcal{C}^{\overline{N}\times 1}$ where $\overline{\underline{\psi}}$ is a vector of "phase-shifters".

- **Tx, Point-E**: At this point the signal will be

$$\underline{m}(t_l) \odot \overline{\underline{w}} \odot \exp(j\overline{\underline{\psi}}), \forall l \tag{1.1}$$

However, the experiments presented in Chapter 2, there are no Tx beamformers and Tx phase shifters, which implies that

$$\overline{\underline{w}} = \underline{1}_{\overline{N}} \text{ and } \overline{\underline{\psi}} = \underline{0}_{\overline{N}} \tag{1.2}$$

Consequently, the signal at Point-A and Point-E will be same i.e. the baseband discrete vector-signal

$$\underline{m}(t_l), \forall l \tag{1.3}$$

- **Tx, Point-F**:
  The discrete baseband signal $\underline{m}(t_l)$,$\forall l$, will be converted to an RF snapshot after passing through a DUC. Thus, at Point-F we will observe the following bandpass signal

$$\underline{m}(t_l)\exp(j2\pi F_c t_l), \forall l \tag{1.4}$$

- **Tx, Point-G:**
  The DAC output is supplied with the input signal from Equation 1.4. This output is a time-continuous bandpass pulse signal

$$\underline{m}(t)\exp(j2\pi F_c t), \forall t \tag{1.5}$$

- **Tx, Point-H**: The analogue RF section of the radar includes a high-power amplifier (HPA) and a band-pass filter (BPF). At the output of the bandpass filter, the signal can be modelled as follows:

$$\sqrt{P_{Tx}}\underline{m}(t)\exp(j2\pi F_c t), \forall t \tag{1.6}$$

where P_{Tx} is the Tx power. Figure 1.7 shows an example of one of the elements of the vector signal $\underline{m}(t)$ at Point-H. This is a continuous pulse-signal, with each pulse containing a code-signal of $\mathcal{N}_c$ code-symbols (example: $\mathcal{N}_c = 80$).

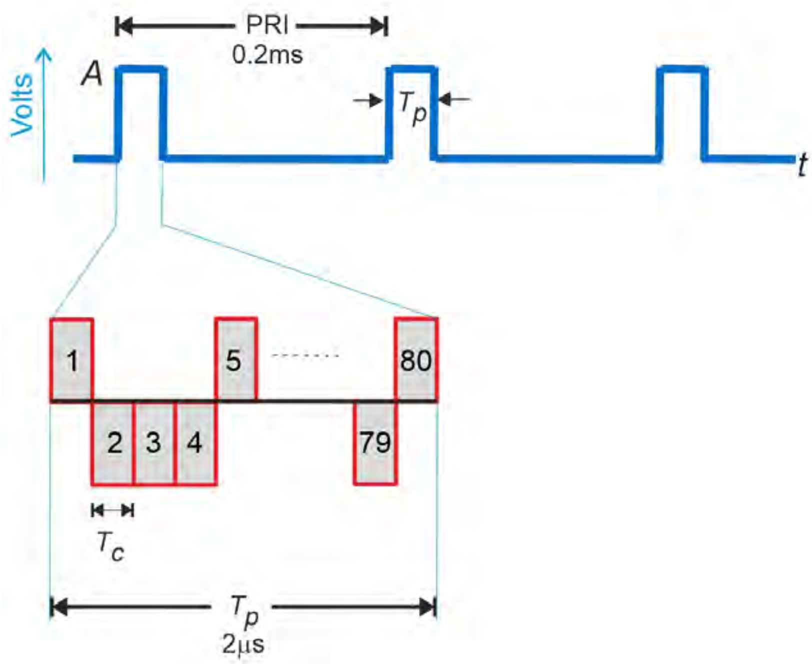

Figure 1.7: One element of the baseband vector-signal $\underline{m}(t)$, with $\mathcal{N}_c = 80$.

- **Tx, Point-T, Splitter's output**: The input to the splitter is an $\overline{N}$ element vector-signal, given by Equation 1.6, while its output is transformed by the "splitter" into a vector-signal of $\overline{N}'$ elements, which can be expressed as follows

$$\sqrt{P_{Tx}}\mathbb{T}\underline{m}(t)\exp(j2\pi F_c t), \forall t \tag{1.7}$$

where the matrix $\overline{\mathbb{T}}$ in Figure 1.6 models the "splitter" with

$$\overline{\mathbb{T}} \triangleq \frac{1}{2}\left[\mathbb{I}_{\overline{N}}, \quad \mathbb{I}_{\overline{N}}\right]^T \tag{1.8}$$

where the factor 1/2 denotes a two-branch splitter and $\mathbb{I}_{\overline{N}}$ represents an $\overline{N} \times \overline{N}$ identity matrix. We will refer to the splitter transformation as the "$\bar{\mathbb{T}}$-transformation", which maps the $\overline{N}$ transmit streams to the $\overline{N}'$ Tx antenna elements.

- **Tx-Antenna-Array**: The matrix with columns $\underline{\overline{r}}_1$, $\underline{\overline{r}}_2$, etc., shown next to the Tx antenna array in Figure 1.6, includes all the Cartesian coordinates of the Tx antenna array. The antenna array will transform the electrical vector-signal $\sqrt{P_{Tx}}\overline{\mathbb{T}}\underline{m}(t)\exp(j2\pi F_c), \forall t$ (see Point-T) to electromagnetic waves that will propagate in our 3D-dimensional physical space.

- **Rx, Point-$\hat{\mathbf{T}}$**:

  In Figure 1.6 the Rx is on the RHS branch with signals flowing downward. Likewise, the Rx antenna array will convert the electromagnetic wave into an electrical signal.

  At the output of the Rx antenna array, we can observe a band-pass received signal which may include the echoes from targets (if present), clutter and bandpass noise. This is a vector-signal of N' elements and can be expressed as

$$\underline{y}(t)\exp(j2\pi F_c t) \in \mathcal{C}^{N' \times 1} \tag{1.9}$$

  where $\underline{y}(t) \in \mathcal{C}^{N' \times 1}$ is the baseband part of the observed signal. The structure/modelling of this signal will be presented later in this document.

- **Rx, Point-$\hat{\mathbf{H}}$**:

  The input to the "combiner" is an N' vector-signal and at Point-$\hat{\mathrm{H}}$ we observed an N vector-signals which can be written as

$$\underline{x}(t)\exp(j2\pi F_c t)$$

$$= \underbrace{\mathbb{T}\underline{y}(t)}_{=\underline{x}(t)} \exp(j2\pi F_c t) \tag{1.10}$$

where $\underline{x}(t) \in \mathcal{C}^{N\times 1}$ is the baseband signal observed at Point-Ĥ. The transformation matrix $\mathbb{T}$ shown in Figure 1.6 models the "combiner" and it is defined as

$$\mathbb{T} \triangleq \left[\mathbb{I}_N, \quad \mathbb{I}_N\right] \tag{1.11}$$

We will refer to the combiner transformation as the "$\mathbb{T}$-transformation", which combines the signals from the N' Rx antenna elements into N receiver streams. In this document, we will refer to the overall transformations due to both "splitter" and "combiner" as the "$\bar{\mathbb{T}}/\mathbb{T}$-transformation".

- **Rx, Points from $\hat{\mathbf{F}}$ to $\hat{\mathbf{A}}$:**

  The signal at Point-F̂ is the discretised version of the continuous vector-signal at Point-Ĥ. That is

$$\underline{x}(t_l)\exp(j2\pi F_c t_l) \in \mathcal{C}^{N\times 1}, \forall l, l = 1, 2, ... \tag{1.12}$$

Then the carrier is removed by the DDC[1] and, thus, at Point-Ê we get the baseband vector-signal $\underline{x}(t_l) \in C^{N\times 1}, \forall l$. The phase-shifters $\exp(j\underline{\psi}) \in \mathcal{C}^{N\times 1}$and the beamforming weights $\underline{w} \in \mathcal{C}^{N\times 1}$are then applied to the $\underline{x}(t_l)$ and finally at Point-Â we have:

$$\underline{x}(t_l) \odot \exp(j\underline{\psi}) \odot \underline{w}, \forall l, \tag{1.13}$$

However, by assuming that there are no weights $\underline{w}$ and no phase shifters, i.e.

$$\underline{w} = \underline{1}_N \text{ and } \underline{\psi} = \underline{0}_N, \tag{1.14}$$

Equation 1.13 simplifies to $\underline{x}(t_l), \forall l$, which implies that Point-Â equals Point-Ê.

[1]DDC is equivalent to a multiplication with $\exp(-j2\pi F_c t_l), \forall l$, where t_l is the time instant of the l-th snapshot with l=1,2,3,...

1.2 Motivation and Problem Description

1.2.1 Motivation

MIMO radar systems offer significant advantages over conventional radars, particularly in scenarios involving multiple targets, complex environments, and the need for accurate target parameter estimation. This research is motivated by the potential of MIMO radars to:

- Enhance Target Detection and Separation: By utilising multiple antennas for transmission and reception, MIMO radars can improve the ability to detect and distinguish closely spaced targets.
- Reduce Clutter Interference: MIMO systems can leverage advanced signal processing techniques to suppress clutter and isolate desired target signals.
- Improve Target Parameter Estimation: The additional information provided by multiple antennas allows for more accurate estimation of target parameters such as range, velocity, and direction (DOA and DOD).
- Enable Advanced Applications: MIMO radars pave the way for novel applications such as target classification and tracking in challenging environments.

1.2.2 Problem Description

Despite the benefits of MIMO radars, several challenges remain that limit their full potential. This research focuses on addressing the following key problems:

- Effective Utilisation of Array Manifolds: The basic array manifold's limits the system's DOF to the number of antenna elements. This research explores the concept of extended array manifolds, aiming to surpass this limitation and achieve enhanced DOF.
- Selection and Performance Analysis of MIMO Algorithms: A wide range of MIMO algorithms exist, each with its own strengths and weaknesses. This research aims to evaluate the performance of classical and subspace-based algorithms in real-world scenarios.

- Bistatic MIMO Radar Design: While monostatic MIMO radar systems have been extensively studied [65–67], bistatic configurations offer additional advantages [68]. This research investigates the design and implementation of bistatic MIMO radars with extended array manifolds achieved through slow-time and fast-time coding techniques.

- Understanding Array Bounds: Array bounds define the theoretical limitations on target localisation and parameter estimation accuracy in MIMO systems. This research delves into the analysis of array bounds to guide the design of optimal MIMO radar configurations.

By addressing these problems, this research aims to contribute to the advancement of MIMO radar technology and its practical applications in various domains.

1.3 Research Objectives and Contributions

1.3.1 Objectives

This research investigates the capabilities of multitarget monostatic and bistatic MIMO radar systems. The primary objectives are:

- Exploration of Array Manifolds: This objective delves into the concepts of basic array manifolds and explores the potential of extended array manifolds for enhancing MIMO radar performance.

- Evaluation of MIMO Algorithms: This objective focuses on a comparative analysis of classical and subspace-based MIMO algorithms to determine their effectiveness in target detection and parameter estimation.

- Experimental Data Analysis: This objective leverages data acquired from Saab's experimental monostatic MIMO radar to assess the performance of classical MIMO algorithms in a real-world setting.

- Bistatic MIMO Radar Design with Slow-Time Codes: This objective investigates the design and implementation of a bistatic MIMO radar system that leverages extended array manifolds achieved through the use of slow-time codes.

- Bistatic MIMO Radar Design with Fast-Time Codes: Building upon the previous objective, this objective explores the design of a bistatic MIMO radar that further expands the array manifold by utilising fast-time coding techniques.

- Array Bounds Investigation: This objective focuses on a comprehensive analysis of array bounds, which represent theoretical limitations on target localisation and parameter estimation accuracy in MIMO radar systems.

1.3.2 Contributions

Through the extensive exploration and analysis conducted in this thesis, several significant contributions have been made towards the advancement of MIMO radar technology, spanning system architectures, parameter estimation algorithms, and theoretical performance limitations. The following list summarizes these contributions:

- Studied the Saab's experimental monostatic MIMO radar.

- Developed detailed models for the Saab's experimental monostatic MIMO radar.

- Analysed two sets of radar data obtained from distinct experiments.

- Applied classical MIMO algorithms to the collected radar data.

- Employed virtual algorithms and conducted comparative performance analyses with classical algorithms.

- Investigated and proposed a novel algorithm tailored for bistatic MIMO radars, leveraging slow time codes to expand the observation space and enhance estimation performance.

- Explored and proposed another novel algorithm for bistatic MIMO radars, utilising fast time codes and virtual-spatiotemporal array manifold concepts to significantly extend the observation space and improve estimation performance.

- Analysed various array geometries utilised in this thesis and assessed their performance against theoretical lower bounds.

1.4 Structure of the Thesis

This thesis focuses on MIMO pulsed radar employing antenna arrays at both transmitter and receiver ends, encompassing both monostatic and bistatic/multistatic MIMO radar architectures. The study embarks on experimental exploration, commencing with classical MIMO estimating algorithms and progressing to subspace algorithms enhanced by virtual antenna array concepts. Acknowledging the pivotal role of antenna arrays in MIMO systems, the research will delve into investigating and contrasting the theoretical performance bounds of the arrays utilised in this study. The thesis unfolds as follows:

Chapter 2 presents the Saab's experimental monostatic MIMO radar, elucidating its conceptual model inclusive of transmitter, receiver, and multi-target channel models. Within this chapter, a suite of classical MIMO algorithms will be introduced and subsequently applied to two sets of real radar data for parameter estimation. Detailed information regarding these radar data sets, encompassing their respective environments, targets, array configurations, and system specifications, will be provided. The discussion will extend to the analysis of estimated parameters and their performance, to highlight any system-related challenges. In the pursuit of enhancing estimation performance, the thesis will introduce and implement virtual MIMO Radar concepts for both experimental setups. Ultimately, the performance of classical MIMO algorithms versus virtual MIMO algorithms in both experimental configurations will be compared and summarised

Chapter 3 introduces innovative subspace-based algorithms designed to estimate the parameters of multiple moving or static targets in bistatic MIMO radar systems. The system described utilises a fast-time PN-code (FTC) along with $\overline{N}$ slow time Hadamard codes (STC) to achieve orthogonality between PRIs and sub-frames. The parameters of interest encompass delay/range, DOA, DOD, Doppler frequency, complex path coefficients, and the target's bistatic RCS. Drawing upon parametric bistatic pulse MIMO radar signal models and leveraging the concept of extended array manifolds, this algorithm aims to estimate these parameters effectively, circumventing the challenge of estimates association. The efficacy of the proposed algorithm is scrutinised through rigorous computer simulation studies.

Chapter 4 introduces a novel subspace algorithm tailored for bistatic MIMO Radars, integrating virtual spatiotemporal array manifold concepts to estimate various multitarget parameters amidst clutter and noise. The system leverages $\overline{N}$ PN-codes (FTC) to ensure orthogonality within PRIs. Parameters of interest encompass the DOD, DOA, range, and velocity, with a unique algorithm proposed for their estimation, drawing upon the principles of the "array manifold" and "manifold extenders". The effectiveness of the proposed algorithm is assessed through comprehensive Monte Carlo simulation studies.

Chapter 5 scrutinises the theoretical performance limitations of the antenna arrays utilised in Chapters 2, 3, and 4 within the framework of MIMO radar. The analysis centres on two pivotal aspects vital for precise target tracking and localisation: the Cramer-Rao Lower Bound (CRB) and the Resolution threshold. Additionally, this chapter introduces the concept of the "uncertainty sphere", which serves as the foundation for understanding these bounds.

Chapter 6 concludes this thesis by summarising its key findings and outlining potential future research directions. It highlights the main contributions made in advancing MIMO radar technology and offers suggestions for further exploration in the field. This chapter aims to provide both a reflection on the study's achievements and a roadmap for future investigations.

Chapter 2

Monostatic MIMO Radar Algorithms Based on Experimental LRAM Data

This chapter delves into the L-band Rocket Artillery Mortar (LRAM) experimental radar system which is currently configured as a monostatic MIMO radar. However, it can be reconfigured for bistatic operation with some modifications. Here, we focus on the LRAM's antenna arrays and channel models for the monostatic configuration, considering real experimental radar scenarios with single and multiple targets.

Two monostatic MIMO radar experiments were conducted during this research. In this chapter MIMO parameter estimation algorithms will be investigated using two experimental datasets provided by Saab.

2.1 Saab's LRAM Experimental MIMO Radar

The Saab's digital radar technology, exemplified by the LRAM system employed in this study, represents a generic implementation of MIMO radar. Operating within the L-band frequency spectrum, the LRAM system features $\overline{N}'$ transmit antennas and N' receive antennas, offering configurational flexibility and enabling the collection of received data for subsequent offline analysis. In this research, the

LRAM system is configured as a monostatic MIMO radar, where the DOD and DOA coincide. However, with modifications, it could be reconfigured for bistatic operation.

While detailed information about the LRAM system is limited due to its ongoing development, available information suggests that it is a modular and flexible/scalable system architecture. This architecture reflects Saab's experimental system operation using generic radar blocks facilitates the understanding of subsystem/component interactions, and allows for the reconfiguration of the two antenna arrays into different geometrical shapes for various experiments.

2.2 LRAM Radar's Antenna Array

Figure 2.1 shows the antenna array block of the LRAM system. This block is an 8×12 grid planar matrix containing omnidirectional antenna elements spaced 10 cm apart. The grid offers various configuration options and can be divided into both transmit and receive arrays. The experimental datasets provided by Saab, and used in this chapter, have been collected by their monostatic LRAM based on the 96 antennas of Figure 2.1.

Figure 1.6 fully represents Saab's LRAM experimental MIMO radar where $\overline{N} = N = 12$. In one experiment, which provided data Set-A, $\overline{N}' = N' = 24$ antennas were employed for both Tx and Rx. In the second experiment (data Set-B), $\overline{N}' = \overline{N} = 12$ antennas were employed by the Tx array and $N' = N = 24$ antennas by the Rx array.

Remember that the symbols $\overline{N}'$ and N' denote the number of Tx and Rx antennas, respectively. Similarly, $\overline{N}$ and N denote the number of Tx and Rx streams, respectively. In general, the number of Tx/Rx streams ($\overline{N}$, N) may not equal the number of antennas ($\overline{N}'$, N'). The current system has a maximum number of Tx and Rx streams of $\overline{N} = N = 12$.

It is clear that in Table-2.1 the algorithms use the vector $\underline{\overline{S}}(\theta) \in \mathcal{C}^{\overline{N} \times 1}$ and $\underline{S}(\theta) \in \mathcal{C}^{N \times 1}$ which are the manifold vectors of the Tx array and the Rx array, respectively. These two vectors are defined as follows:

$$\underline{S}(\theta,\phi) \triangleq \exp(-j[\underline{r}_1, \underline{r}_2, .., \underline{r}_N]^T \underline{k}(\theta,\phi)) \tag{2.1}$$

$$\overline{\underline{S}}(\theta,\phi) \triangleq \exp(+j[\overline{\underline{r}}_1, \overline{\underline{r}}_2, .., \overline{\underline{r}}_N]^T \underline{k}(\theta,\phi)) \tag{2.2}$$

$$\text{with } \underline{k}(\theta,\phi) \triangleq \frac{2\pi}{\lambda}[\cos\theta\cos\phi, \sin\theta\cos\phi, \sin\phi]^T \tag{2.3}$$

Note that the vector $\underline{k}(\theta,\phi) \in \mathcal{R}^{3\times 1}$ is the wavenumber vector associated with the direction of propagation (θ,ϕ) of the electromagnetic wave.

(a) SAAB's actual array of 96 antennas

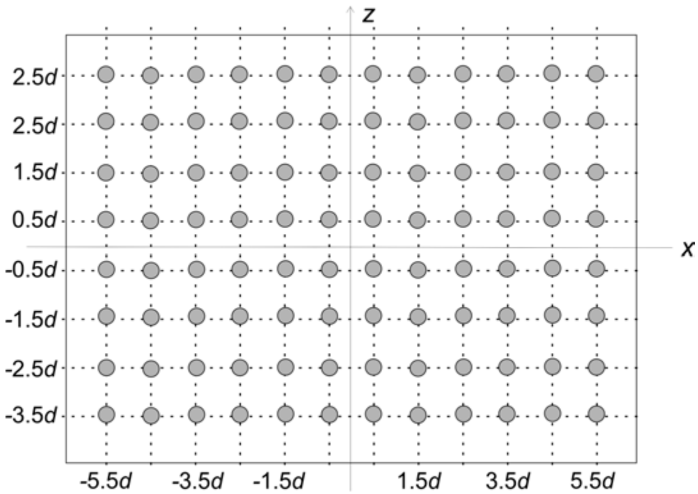

(b) Conceptual diagram of array with Cartesian coordinates

Figure 2.1: The LRAM radar's antenna array block, $d = 10$ cm

2.3 Monostatic MIMO Radar Channel Modelling

This section focuses on modelling the received signal vector $\underline{x}(t)$, which is essential for the operation of MIMO radar algorithms. To achieve this, we need to model the MIMO radar channel, which can be divided into two main categories:

- Single-Target Channel: This will be discussed in detail in Section 2.3.1.
- Multi-Target Channel: This will be presented in Section 2.3.2.

2.3.1 Single-Target MIMO Modelling

Consider that the radar operates in the presence of a single target with a radial velocity v and a range R and direction (θ, ϕ). Since the LRAM radar is a monostatic system, the DOD of the electromagnetic waves from the Tx array to the target and the DOA of the waves from the target to the Rx array are identical ($\overline{\theta} = \theta$ and $\overline{\phi} = \phi$). This model is also applicable to a bistatic radar, where the Tx and Rx antenna arrays are located at different sites with their local reference points, leading to non-identical DOD and DOA ($\overline{\theta} \neq \theta$ and $\overline{\phi} \neq \phi$).

Figure 2.2 presents the modelling of a single-target MIMO radar wireless channel (see "grey" square) together with the main blocks of Tx and Rx, ignoring ADC/DAC, HPA and BPF that are shown in Figure 1.6.

The vector signal at the output of the splitter (see Point-T in Figure 2.2) will be transformed by the Tx antenna array into a vector of $\overline{N}$ electromagnetic waves (one per antenna) which will propagate through our 3D physical space. The various "displacements" of these electromagnetic waves at the Tx antennas are a function of:

- the Tx-array geometry, and
- their direction of propagation.

These electromagnetic "displacements" for the target's direction $(\overline{\theta}, \overline{\phi})$ are modelled by the Tx manifold vector $\underline{\overline{S}}(\overline{\theta}, \overline{\phi}) \in \mathcal{C}^{\overline{N} \times 1}$ which is defined in Equation 2.2.

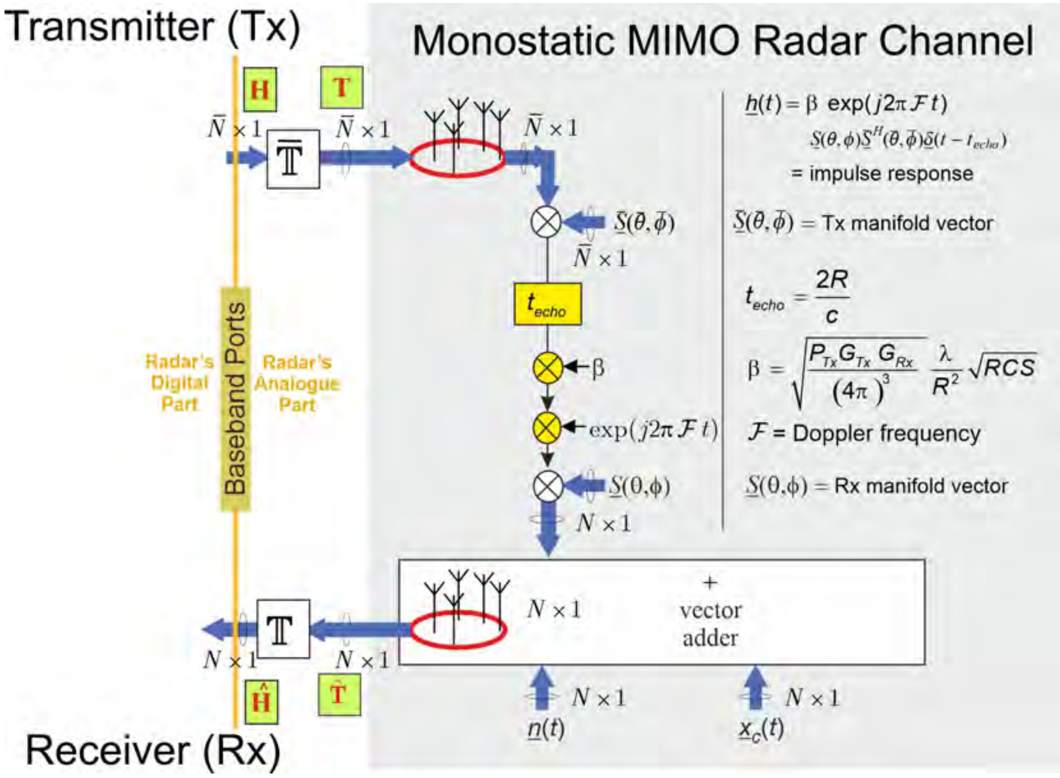

Figure 2.2: Single-target monostatic MIMO radar channel.

The target will reflect the transmitted electromagnetic waves, and the radar's Rx antenna array will receive the echo after a propagation time t_{echo}. Figure 2.2 shows the delay t_{echo}, the path weight β and the effects of the target's Doppler frequency $\mathcal{F}$. Note that the parameter β in Figure 2.2 is expressed, with the help of the radar's equation, as a function of:

- the target's RCS,
- the antenna gains of the Tx and Rx, i.e. G_{Tx} and G_{Rx} respectively,
- the target's range R, and
- the power of the transmitted signal P_{Tx}.

Furthermore, the various "displacements" of the electromagnetic waves arriving at the Rx antenna array are modelled by the Rx manifold vector $\underline{S}(\theta, \phi)$. Overall, the "impulse response" of a MIMO single target radar channel is the $N \times 1$ complex vector $\underline{h}(t)$ which can be expressed as

$$\underline{h}(t) = \beta \exp(j2\pi\mathcal{F}t)\underline{S}(\theta,\phi)\overline{\underline{S}}^H(\overline{\theta},\overline{\phi})\underline{\delta}(t-t_{echo}) \tag{2.4}$$

as this is also shown in Figure 2.2.

It is important to point out that the impulse response vector $\underline{h}(t)$ and the Rx manifold vector $\underline{S}(\theta,\phi)$ are[1] "collinear". This implies that the Rx manifold vector plays a significant role in the channel's impulse response, while the Tx manifold vector $\overline{\underline{S}}(\overline{\theta},\overline{\phi})$ is transformed to a less important "scalar" quantity, i.e. $\overline{\underline{S}}^H(\overline{\theta},\overline{\phi})\underline{\delta}(t-t_{echo})$. That is, Equation 2.4 may be rewritten as follows:

$$\underline{h}(t) = \underbrace{\beta \exp(j2\pi\mathcal{F}t)\overline{\underline{S}}^H(\overline{\theta},\overline{\phi})\underline{\delta}(t-t_{echo})}_{scalar}\underline{S}(\theta,\phi) \tag{2.5}$$

Based on the above modelling, the received vector-signal $\underline{y}(t) \in \mathcal{C}^{N\times 1}$ at Point-$\hat{\mathrm{T}}$ can be written as

$$\begin{aligned} \underline{y}(t) &= \underline{h}(t) \circledast \sqrt{P_{Tx}}\overline{\mathbb{T}}\underline{m}(t) + \underline{x}_c(t) + \underline{n}(t) && \text{(2.6a)} \\ &= \underbrace{\sqrt{P_{Tx}}\beta \exp(j2\pi\mathcal{F}t)\overline{\underline{S}}^H(\overline{\theta},\overline{\phi})\overline{\mathbb{T}}\underline{m}(t-t_{echo})}_{\text{scalar signal}}\underline{S}(\theta,\phi) \\ &\quad + \underline{x}_c(t) + \underline{n}(t) && \text{(2.6b)} \end{aligned}$$

where $\circledast$ denotes "convolution", $\underline{x}_c(t)$ represented the "clutter" effects and $\underline{n}(t)$ is the complex additive white Gaussian noise (AWGN).

Finally, at Point-$\hat{\mathrm{H}}$ (baseband ports) we receive the vector signal $\underline{x}(t) \in \mathcal{C}^{N\times 1}$

$$\begin{aligned} \underline{x}(t) &= \mathbb{T}\underline{y}(t) \\ &= \underbrace{\sqrt{P_{Tx}}\beta \exp(j2\pi\mathcal{F}t)\overline{\underline{S}}^H(\overline{\theta},\overline{\phi})\overline{\mathbb{T}}\underline{m}(t-t_{echo})}_{\text{scalar}}\mathbb{T}\underline{S}(\theta,\phi) \\ &\quad + \mathbb{T}\underline{x}_c(t) + \mathbb{T}\underline{n}(t). && \text{(2.7)} \end{aligned}$$

[1] Note: both $\underline{h}(t)$ and $\underline{S}(\theta,\phi)$ are embedded in an N dimensional complex observation space.

2.3.2 Multi-Target MIMO Modelling

In this section, the signal flow up to the Point-A in Figure 1.6 is also provided for a multi-target MIMO radar channel (see Equation 2.11). If the radar operates in the presence of M targets, then the radar channel impulse response (Equation 2.4) can be generalised as follows:

$$\underline{h}(t) = \sum_{\ell=1}^{M} \beta_\ell \exp(j2\pi\mathcal{F}_\ell t)\ \underline{S}_\ell\ \underline{\overline{S}}_\ell^H \underline{\delta}(t - \tau_{echo,\ell}) \tag{2.8}$$

where the subscript ℓ has been added to the channel/target parameters (defined in Section 2.3.1) to associate them with the ℓ-th target. Indeed, for the ℓ-th target, the various MIMO channel parameters included in Equation 2.8 are:

$$\begin{aligned}
\underline{\overline{S}}_\ell &= \underline{\overline{S}}(\overline{\theta}_\ell, \overline{\phi}_\ell) = \text{Tx-array manifold vector} \\
\underline{S}_\ell &= \underline{S}(\theta_\ell, \phi_\ell) = \text{Rx-array manifold vector} \\
\theta_\ell &= \text{Azimuth angle} \\
\phi_\ell &= \text{Elevation angle} \\
\tau_{echo,\ell} &= \text{the time from Tx to Rx for the } \ell\text{-th target's returned signal} \\
\mathcal{F}_\ell &= \frac{2v_\ell F_c}{c} : \text{Doppler frequency shift due to } \ell\text{-th target's velocity } v_\ell \\
& \quad\ \text{with} \begin{cases} v_\ell = \text{target's radial velocity} \\ F_c = \text{carrier frequency} \\ c = \text{speed of light} \end{cases}
\end{aligned}$$

Furthermore, the single target MIMO radar channel, shown in the "grey" square of Figure 2.2, can be extended to multi-target by adding parallel "branches" - one branch per target (M branches in total) - as this is shown in Figure 2.3. Based on the above, the received baseband signal $\underline{y}(t) \in \mathcal{C}^{N\times 1}$ at Point-$\hat{\mathrm{T}}$, shown in Figure 2.3, can be represented as follows:

$$\begin{aligned}
\underline{y}(t) &= [y_1(t), y_2(t), ..., y_N(t)]^T && (2.9a) \\
&= \underline{h}(t) \circledast \sqrt{P_{Tx}}\mathbb{T}\underline{m}(t) + \underline{x}_c(t) + \underline{n}(t) && (2.9b)
\end{aligned}$$

$$= \sum_{\ell=1}^{M} \sqrt{P_{Tx}}\beta_\ell \exp(j2\pi\mathcal{F}_\ell t)\underline{S}_\ell \underbrace{\overline{\underline{S}}_\ell^H \overline{\mathbb{T}}\underline{m}(t-\tau_{echo,\ell})}_{\text{scalar signal}}$$
$$+\underline{x}_c(t)+\underline{n}(t) \tag{2.9c}$$

where $\circledast$ denotes "convolution".

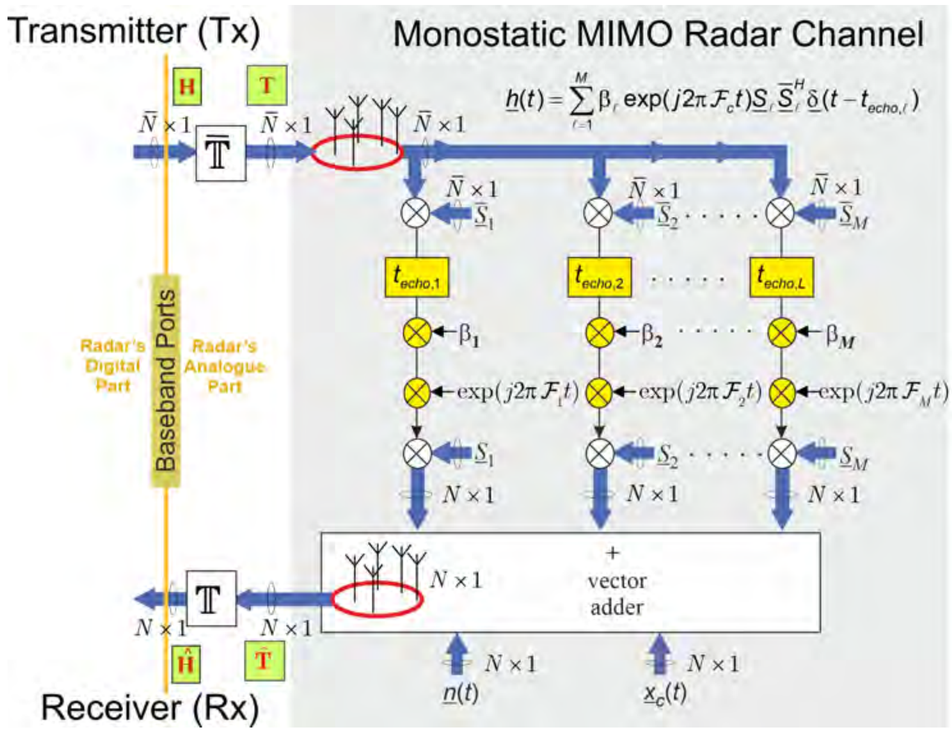

Figure 2.3: Multi-target monostatic MIMO radar channel.

Then, at Point-Ĥ (baseband ports) we have the $(N \times 1)$ vector-signal,

$$\underline{x}(t) = [x_1(t), x_2(t), ..., x_N(t)]^T \tag{2.10a}$$
$$= \mathbb{T}\underline{y}(t) \tag{2.10b}$$
$$= \sum_{\ell=1}^{M} \sqrt{P_{Tx}}\beta_\ell \exp(j2\pi\mathcal{F}_\ell t)\mathbb{T}\underline{S}_\ell \underbrace{\overline{\underline{S}}_\ell^H \overline{\mathbb{T}}\underline{m}(t-\tau_{echo,\ell})}_{\text{scalar signal}}$$
$$+\mathbb{T}\underline{x}_c(t)+\mathbb{T}\underline{n}(t) \tag{2.10c}$$

At Point-Ê, we obtain "snapshots" of $\underline{x}(t)$. Assuming there are no weights $\underline{w}$ and no phase shifters $\underline{\psi}$ (see Equation 1.14), then, at Point-Â (which, in this case, is the same as Point-Ê), we also obtain "snapshots" of the continuous vector signal $\underline{x}(t)$, as given by Equation 2.10a. That is,

$$\underline{x}(t_l), \forall l \tag{2.11}$$

As mentioned in the previous section, the multi-target model is also applicable to a bistatic radar. In a bistatic configuration, the Tx and Rx antenna arrays are located at different sites with their local reference points, leading to non-identical DOD and DOA ($\overline{\theta} \neq \theta$ and $\overline{\phi} \neq \phi$).

2.4 Monostatic MIMO Algorithms

In the "Baseband Signal Processor" of the LRAM, the following "classical" MIMO radar localisation algorithms are employed for this research; Least Square (LS), Capon, Amplitude and Phase Estimation (APES), Capon and AML algorithm (CAML) and MUSIC algorithms [69], [70]. Table-2.1 shows the main cost functions of these algorithms:

Table 2.1: MIMO localisation algorithms

Algorithm	Main Cost Function (variable: azimuth angle)
LS	$\beta(\theta) = \frac{\underline{S}^H(\theta)\mathbb{R}_{xm}\underline{\overline{S}}(\theta)}{N\overline{N}}$
Capon	$\beta(\theta) = \frac{\underline{S}^H(\theta)\mathbb{R}_{xx}^{-1}\mathbb{R}_{xm}\underline{\overline{S}}(\theta)}{\overline{N}\underline{S}^H(\theta)\mathbb{R}_{xx}^{-1}\underline{S}(\theta)}$
APES	$\beta(\theta) = \frac{\underline{S}^H(\theta)\mathbb{Q}^{-1}\mathbb{R}_{xm}\underline{\overline{S}}(\theta)}{\overline{N}\underline{S}^H(\theta)\mathbb{Q}^{-1}\underline{S}(\theta)}$ where $\mathbb{Q} = \mathbb{R}_{xx} - \frac{1}{\overline{N}}\mathbb{R}_{xm}\underline{\overline{S}}(\theta)\underline{\overline{S}}^H(\theta)\mathbb{R}_{xm}^H$
CAML	$\underline{\beta}(\underline{\theta}) = \left[\left(\mathbb{S}^H(\underline{\theta})\mathbb{Q}^{-1}\mathbb{S}(\underline{\theta})\right) \odot \left(\overline{\mathbb{S}}^H(\underline{\theta})\mathbb{R}_{mm}\overline{\mathbb{S}}(\underline{\theta})\right)^T\right]^{-1}$ $.\underline{\mathrm{diag}}\left\{\mathbb{S}^H(\underline{\theta})\mathbb{Q}^{-1}\mathbb{R}_{xm}\overline{\mathbb{S}}(\underline{\theta})\right\}$ where $\mathbb{Q} = \mathbb{R}_{xx} - \mathbb{R}_{xm}\overline{\mathbb{S}}(\underline{\theta})\left(\overline{\mathbb{S}}^H(\underline{\theta})\mathbb{R}_{mm}\overline{\mathbb{S}}(\underline{\theta})\right)^{-1}$ $.\overline{\mathbb{S}}^H(\underline{\theta})\mathbb{R}_{xm}^H$
MUSIC	$\xi(\theta) = \frac{\underline{S}^H(\theta)(\mathbb{I}_N - \mathbb{E}_n\mathbb{E}_n^H)\underline{S}(\theta)}{\underline{S}^H(\theta)\underline{S}(\theta)}$ or equivalently, $\xi(\theta) = \frac{\underline{S}^H(\theta)\underline{S}(\theta)}{\underline{S}^H(\theta)\mathbb{E}_n\mathbb{E}_n^H\underline{S}(\theta)}$ where $\mathbb{E}_n$ = "noise" subspace eigenvectors

where $\mathbb{R}_{xx}$, $\mathbb{R}_{xm}$, $\mathbb{R}_{mm}$ are covariance or correlation matrices[2] based on the signals $\underline{x}(t)$ and $\underline{m}(t)$. In practice, the signals $\underline{x}(t)$ and $\underline{m}(t)$ are observed over a finite period of L snapshots, which are then used to estimate the practical covariance or correlation matrices by

$$\mathbb{R}_{xx} = \frac{1}{L}\sum_{l=1}^{L}\underline{x}\left(t_l\right)\underline{x}^H\left(t_l\right); \quad \mathbb{R}_{xm} = \frac{1}{L}\sum_{l=1}^{L}\underline{x}\left(t_l\right)\underline{m}^H\left(t_l\right); \quad \mathbb{R}_{mm} = \frac{1}{L}\sum_{l=1}^{L}\underline{m}\left(t_l\right)\underline{m}^H\left(t_l\right). \tag{2.13}$$

2.4.1 Classical MIMO Algorithms

In this section, the radar target's parameter estimation based on classical MIMO algorithms will be introduced. These are called:

1. LS

   The Least Squares algorithm is a fundamental technique used to find the best-fit line or curve for a set of data points. It achieves this by minimizing the sum of the squared vertical distances between the data points and the fitted line/curve. This ensures the line/curve passes as close to the data points as possible. The concept might have existed earlier, the first clear publication on the method was by Adrien-Marie Legendre in 1805 [71].

2. Capon

   The Capon algorithm is named after its inventor, J. Capon, who published the method in 1969 [72]. His work built upon earlier research in spectral analysis and array processing. The Capon algorithm, also known as the Minimum Variance Distortionless Response (MVDR) beamformer, is a high-resolution technique used for estimating the DOA of multiple sources impinging on an antenna array. It works by designing a spatial filter that maximises the signal-to-noise ratio (SNR) in the desired direction while minimising the

[2] The theoretical covariance/correlation matrices for an infinite observation period are defined as follows

$$\mathbb{R}_{xx} = \mathcal{E}\left\{\underline{x}(t)\underline{x}^H(t)\right\}; \mathbb{R}_{xm} = \mathcal{E}\left\{\underline{x}(t)\underline{m}^H(t)\right\}; \mathbb{R}_{mm} = \mathcal{E}\left\{\underline{m}(t)\underline{m}^H(t)\right\} \tag{2.12}$$

noise power from other directions [73]. This allows for accurate identification of the source locations, even when multiple signals are present closely together. Note that Capon is an extension of LS by an addition of a Rx beamformer.

3. APES

   The APES algorithm is a spectral estimation technique used to estimate the complex amplitude of the power spectrum of a random process. It utilises a bank of adaptive filters tuned to specific frequencies to analyse the signal and derive estimates of both amplitude and phase components [58]. While the exact origin of the APES algorithm is unclear, its development likely stems from research in spectral estimation during the latter half of the 20th century. Early work on adaptive filter-based spectral estimation methods laid the foundation for the APES approach. This beamformer aims to find an output that closely resembles the desired signal. It achieves this through a constrained optimisation problem, which shares similarities with the solution obtained by Capon's MVDR beamformer.

4. CAPES and CAML methodologies, as discussed in [58, 74, 75], leverage the strengths of Capon and APES algorithms for achieving accurate estimates of target parameters. Capon demonstrates superior performance in estimating the DOA, while APES excels in providing precise estimates of the parameter β. By combining these algorithms in different configurations, superior estimates of both DOA and β can be obtained. For instance, CAPES utilises Capon for DOA estimation and APES for β estimation, whereas CAML employs CAPES for DOA and Approximate Maximum Likelihood (AML) for β estimation. CAML has been shown to yield more accurate β estimates compared to individual methods. The key distinction lies in the optimisation process: Capon minimizes variance, whereas CAML approximates the maximum likelihood function, potentially offering computational advantages as well [74, 76].

5. MUSIC

   The MUSIC algorithm, often regarded as a super-resolution technique, serves the purpose of estimating the DOA for multiple sources incident upon an antenna array [75]. This algorithm capitalises on the orthogonality between the signal and noise subspaces $\mathcal{L}\mathbb{E}_s \perp \mathcal{L}\mathbb{E}_n$, respectively, within the eigen-decomposed covariance matrix of the received signals. Suppose there are K targets present in the received data snapshots, where $K < N$. Let $\mathbb{E}_s \in \mathcal{C}^{N\times K}$ and $\mathbb{E}_n \in \mathcal{C}^{N\times N-K}$ denote the eigenvector matrices, and $\mathbb{D}_s \in \mathcal{C}^{K\times K}$ and $\mathbb{D}_n \in \mathcal{C}^{N-K\times N-K}$ represent the diagonal matrices of eigenvalues corresponding to the signal and noise subspaces, respectively. To distinguish the signal subspace from the noise subspace, a threshold can be established. Commonly used methods for this purpose include Akaike Information Criteria (AIC) or Minimum Descriptor Length (MDL) [77].

   Typically, targets occupy different range bins, rendering them uncorrelated with each other. Consequently, the signal subspace can be adequately characterised by the Rx array manifold vectors $\mathbb{S} = \left[\underline{S}(\theta_1),\ \ \underline{S}(\theta_2),\ \ \ldots,\ \ \underline{S}(\theta_K)\right] \in \mathcal{C}^{N\times K}$. This implies that $\mathcal{L}\mathbb{S} = \mathcal{L}\mathbb{E}_s$ and also $\mathcal{L}\mathbb{S} \perp \mathcal{L}\mathbb{E}_n$. In other words, projecting the Rx array manifold vector from a target's direction onto the noise subspace yields a zero vector $\mathbb{P}_{\mathbb{E}_n}\underline{S}(\theta_k) = \underline{0}_N, \forall k = 1, 2, \ldots, K$. Hence, sweeping the directional parameter θ enables the generation of the spatial spectrum using the MUSIC algorithm.

The first four algorithms, LS, Capon, APES and CAML, share the capability of estimating both the DOA and the complex path gain (β) for multiple targets. This allows them to construct a complete spatial spectrum of $\beta(\theta)$, representing the strength and direction of the received signals. In contrast, the MUSIC algorithm primarily focuses on DOA estimation. It utilises the inherent properties of the covariance matrix to identify the signal subspace, which contains information about the source directions. While it can indirectly provide insights into the relative strengths of the sources based on the signal subspace structure, it doesn't directly estimate the complex path gain values for each target.

2.5 Monostatic MIMO Radar Experiments based on Saab's LRAM

Two experiments were conducted using the aforementioned LRAM monostatic MIMO radar system. These experiments employed different system designs and configurations. Saab provided the resulting data sets, labelled *data Set-A* and *data Set-B*. The data from both sets correspond to Point-Â, Figure 1.6, with the assumption that no beam-formers or phase-shifters are employed. The signal processing algorithms are located in the "baseband signal processing Rx", shown in Figure 1.6. The array manifold employed for the Tx and Rx array in *data Set-A* and the Rx array in *data Set-B* is given by Equation 2.22, with the Tx array manifold for *data Set-B* given by Equation 2.16 in the following sections.

2.5.1 First Experiment's Description

Data Set-A from the first experiment is concerned with received data at Point-$\widehat{A}$ (discrete version of signal $\underline{x}(t)$) of the LRAM MIMO radar architecture, shown in Figure 1.6. The environment for this experiment is shown in Figure 2.4.

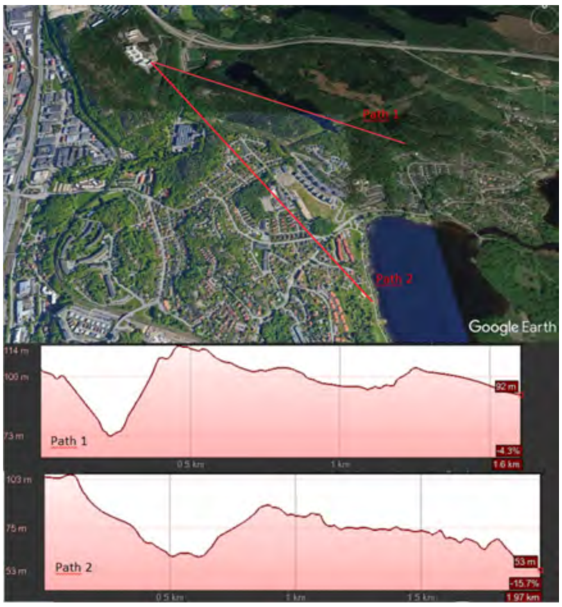

Figure 2.4: Map of the experiment test site in Gothenburg.

It uses the Tx/Rx array geometries of Figure 2.5 and MIMO radar channel model described in Figures 2.3. The experiment considers $M = 2$ UAV targets, both moving away from the radar at different velocities and trajectories, over a period covered by 22 frames.

Figure 2.5 shows the Tx/Rx Array Geometry used for the *data Set-A*.

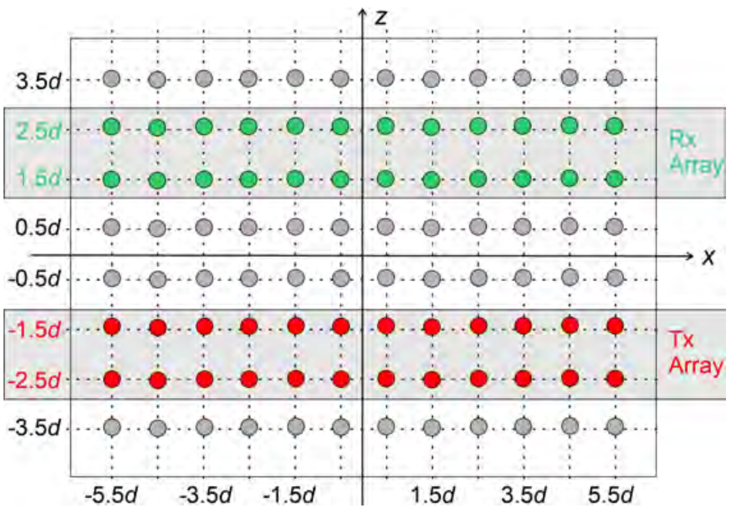

Figure 2.5: Data Set-A Tx and Rx antenna array geometries.

The $\overline{N}' = 24$ "red" antennas of the Figure 2.5 form the Tx array, while the "green" antennas represent that Rx antenna arrays of $N' = 24$ antennas. From Figure 2.5 the Cartesian coordinates of the Rx array geometry, prior to the $\overline{\mathbb{T}}/\mathbb{T}$-transformation for a "planar" array, used in *data Set-A* and are given by the following matrix

$$[\underline{r}_1, \underline{r}_2, .., \underline{r}_{24}] \triangleq d \begin{bmatrix} \overbrace{\begin{matrix} -5.5, & -4.5, & ..., & +5.5 \end{matrix}}^{\text{upper-row (12-antennas) of Rx-array}} & \overbrace{\begin{matrix} -5.5, & -4.5, & ..., & +5.5 \end{matrix}}^{\text{lower-row (12-antennas) of Rx-array}} \\ \begin{matrix} 0, & 0, & ..., & 0 \end{matrix} & \begin{matrix} 0, & 0, & ..., & 0 \end{matrix} \\ \begin{matrix} +2.5, & +2.5, & ..., & +2.5 \end{matrix} & \begin{matrix} +1.5, & +1.5, & ..., & +1.5 \end{matrix} \end{bmatrix}. \tag{2.14}$$

now, after the "$\mathbb{T}$-transformation" is applied (defined in Equation 1.11), the Rx array coordinates for *data Set-A* are given by

$$[\underline{r}_1, \underline{r}_2, .., \underline{r}_{12}] \triangleq d \begin{bmatrix} -5.5, & -4.5, & ..., & +4.5, & +5.5 \\ 0, & 0, & ..., & 0, & 0 \\ 0, & 0, & ..., & 0, & 0 \end{bmatrix} \tag{2.15}$$

where the inter-antenna spacing d remains fixed and equal to 10 cm for Tx and Rx arrays.

The following equations describe the process to transfer from a planar array to a linear array. The planar array geometry shown in Figure 2.5 is used in both date sets A and B and corresponds to the array manifold vector $\underline{S}(\theta, \phi)$, known also as the *array response vector,*

$$\underline{S}(\theta, \phi) \triangleq \exp(-j[\underline{r}_1, \underline{r}_2, .., \underline{r}_{24}]^T \underline{k}(\theta, \phi)) \tag{2.16}$$

As the number of Rx antennas $N' = 24$ is greater than the 12 data streams, a combiner is employed which is represented by the following matrix

$$\mathbb{T} \triangleq \begin{bmatrix} \mathbb{I}_N, & \mathbb{I}_N \end{bmatrix} \tag{2.17}$$

This matrix $\mathbb{T}$ is applied to the received radar signals and consequently transforms the array manifold vector $\underline{S}(\theta, \phi)$ as follows:

$$\begin{aligned} \underline{a}(\theta, \phi) &= \mathbb{T}\underline{S}(\theta, \phi) && (2.18) \\ &= \exp(-j\frac{2\pi}{\lambda}\underline{r}_x \cos\theta\cos\phi)\underbrace{(\underline{1}_2^T \exp(-j\frac{2\pi}{\lambda}\underline{r}_z \sin\phi))}_{\text{scalar directional gain}=g(\phi)} \\ &= g(\phi)\exp(-j\frac{2\pi}{\lambda}\underline{r}_x \cos\theta\cos\phi) && (2.19) \end{aligned}$$

where,

$$\underline{r}_x \triangleq d\ [-5.5, -4.5, \ldots, -0.5, 0.5, \ldots, 4.5, 5.5]^T \in R^{12\times 1} \tag{2.20}$$

is the transformed geometry, due to the "$\mathbb{T}$-transformation" of the combiner, and

$$\underline{r}_z \triangleq d\ [2.5, 1.5]^T \in R^{2\times 1} \tag{2.21}$$

with resulting Rx linear array manifold vector

$$\begin{aligned} \underline{a}(\theta, 0^\circ) &= \mathbb{T}\underline{S}(\theta, 0^\circ) \\ &= 2\exp(-j\frac{2\pi}{\lambda}\underline{r}_x \cos\theta) && (2.22) \end{aligned}$$

Note that on the transmitter's side, based on the "$\bar{\mathbb{T}}$-transformation" of the splitter, similar results can be provided for a planar Tx array of $\overline{N}' = 24$ antennas, with Tx manifold vector $\underline{\overline{S}}(\theta, \phi)$, and a linear array of $N' = 12$ antennas with Tx manifold vector $\underline{\overline{a}}(\theta, \phi)$.

The range-Doppler contour diagram shown in Figure 2.6 is an example produced by analysing the provided raw data. The strongest energy signal is around zero Doppler frequency ($\mathcal{F} \approx 0$), which is echo from static clutter. With reference to the test site in Figure 2.4, this clutter is most likely ground clutter originating from the wooded areas. The energy signal from the two targets is visible at -95 Hz and -65 Hz indicating the targets are receding. By computing the range-Doppler spectrum, the clutter and noise can be removed to provide a clearer picture of the desired targets.

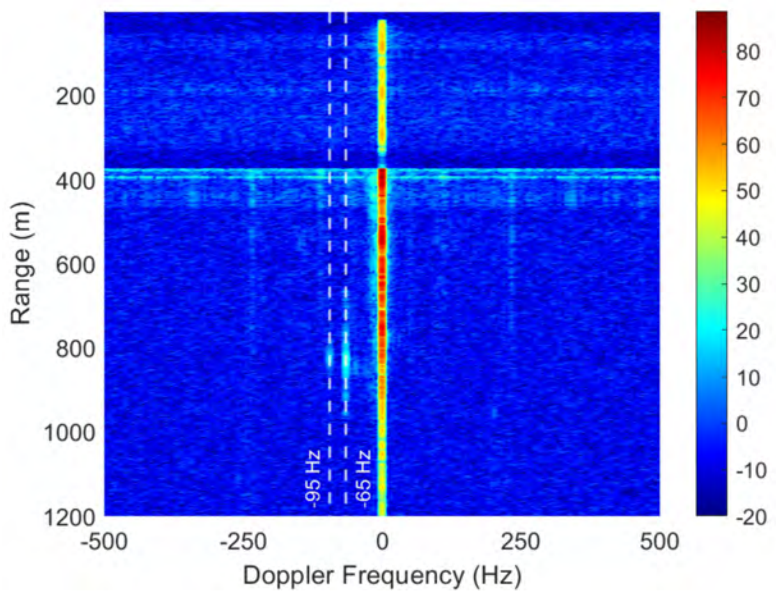

Figure 2.6: Range-Doppler contour plot for data Set-A, Frame 5

Data Set-A (as provided by Saab) includes 12 codes of 80 chips per code (160 numbers per code, due to "oversampling"), these are the codes $\underline{m}(t)$ generated at Point-A in Figure 1.6. However, the 2nd - 12th codes were produced by a delayed version of the 1st code. This presents various challenges for signal processing as,

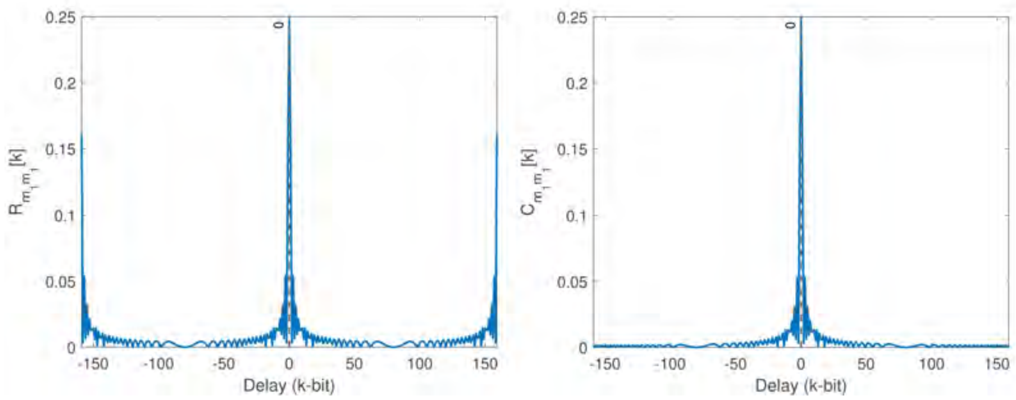

Figure 2.7: Auto-correlation of the 1st code from data Set-A: LHS shows periodic, RHS shows aperiodic.

independent of the definition of periodic or aperiodic correlation[3], the cross and auto-correlation between the streams are similar, which makes target discrimination difficult, especially if the targets are very close together in range.

Figure 2.7 shows the *periodic* and *aperiodic* auto-correlation functions, and Figure 2.8 the equivalent cross-correlations of the provided codes for waveforms 1 and 6. Clearly, the cross-correlation is a delayed version $(-10T_c)$ of the auto-correlation function in both cases. It is understood that Saab's implementation of these codes on the radar's Tx is *aperiodic*.

[3] Definitions: periodic cross-correlation (or simply cross-correlation) of length $\mathcal{N}_c$:

$$R_{m_i m_j}[k] \triangleq \sum_{n=1}^{N_c} m_i[n]\ m_j[n+k] \tag{2.23}$$

aperiodic cross-correlation:

$$C_{m_i m_j}[k] \triangleq \begin{cases} \sum\limits_{n=1}^{N_c-k} m_i[n]\ m_j[n+k], & 0 \leq k \leq \mathcal{N}_c - 1 \\ \sum\limits_{n=1}^{N_c-k} m_i[n-k]\ m_j[n], & 1-\mathcal{N}_c \leq k \leq 0 \\ 0 & \|k\| \geqslant \mathcal{N}_c \end{cases} \tag{2.24}$$

N.B.: there are similar expressions for the auto-correlation functions
Reference: Prof A. Manikas, EE401 Lecture Notes on Advanced Communication Theory, Imperial College London, 1997.

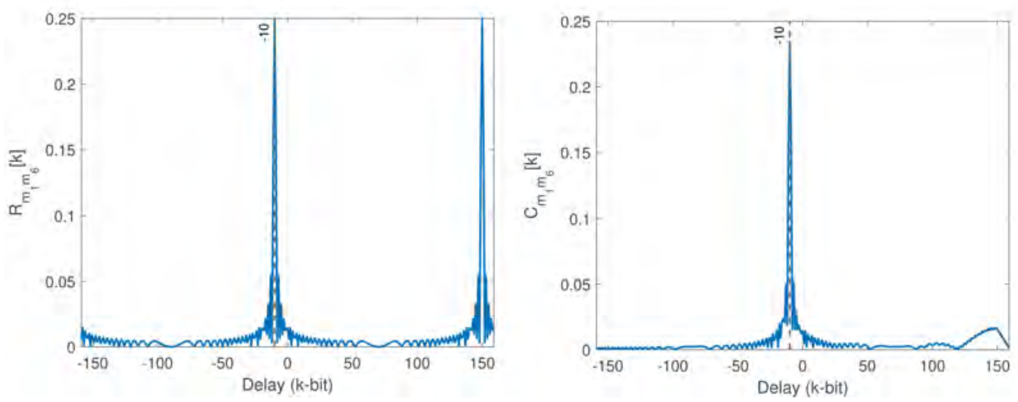

Figure 2.8: Cross-correlation of codes 1 and 6 from data Set-A: LHS shows periodic, RHS shows aperiodic.

2.5.2 Second Experiment's Description

Data Set-B, resulting from the second experiment, is received at Point-$\widehat{A}$ (samples of $\underline{x}(t)$) of Figure 1.6. This data set utilises the MIMO radar channel for a *single-target* detailed in Figure 2.2 and the Tx/Rx array geometry in Figure 2.9.
The experiment was conducted with a single UAV that is $M = 1$, moving away from the radar and a constant velocity for a period covered by 4 frames.

The 12 "red" antennas of Figure 2.9 form the Tx array $\overline{N}' = 12$, while the "green" antennas represent the Rx antenna arrays of $N' = 24$ antennas. From this figure the Cartesian coordinates of the Rx array geometry, prior to the $\overline{\mathbb{T}}/\mathbb{T}$-transformation for a "planar" array, used in *data Set-B* and are given by the following matrix

$$[\underline{r}_1, \underline{r}_2, .., \underline{r}_{24}] \triangleq d \begin{bmatrix} \overbrace{\begin{matrix} -5.5, & -4.5, & ..., & +5.5 \\ 0, & 0, & ..., & 0 \\ +3.5, & +3.5, & ..., & +3.5 \end{matrix}}^{\text{upper-row (12-antennas) of Rx-array}} & \overbrace{\begin{matrix} -5.5, & -4.5, & ..., & +5.5 \\ 0, & 0, & ..., & 0 \\ +2.5, & +2.5, & ..., & +2.5 \end{matrix}}^{\text{lower-row (12-antennas) of Rx-array}} \end{bmatrix}. \tag{2.25}$$

The Rx array coordinates for *data Set-B,* after the transformation

$$[\underline{r}_1, \underline{r}_2, .., \underline{r}_{12}] \triangleq d \begin{bmatrix} -5.5, & -4.5, & ..., & +4.5, & +5.5 \\ 0, & 0, & ..., & 0, & 0 \\ 0, & 0, & ..., & 0, & 0 \end{bmatrix}. \tag{2.26}$$

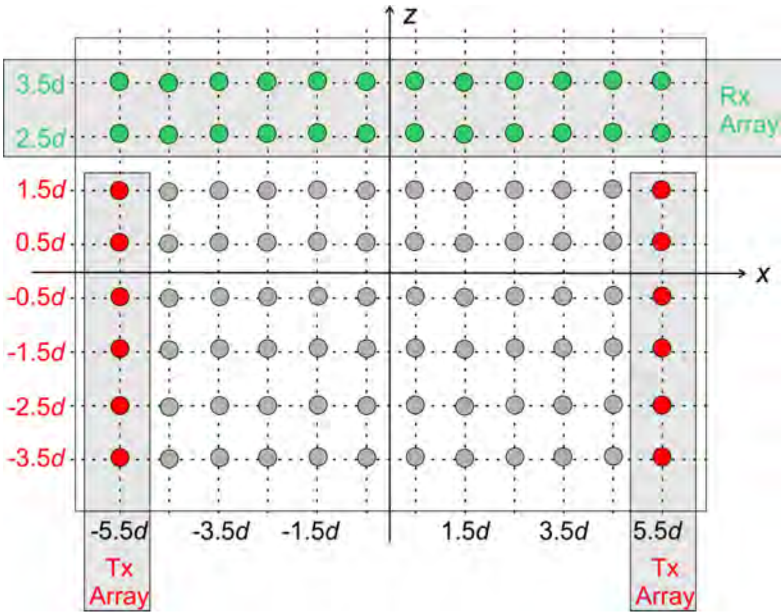

Figure 2.9: Tx and Rx array geometries for data Set-B.

where inter-antenna spacing d remains fixed and equal to 10 cm for Tx and Rx arrays. Note that this is the same as that of *data Set-A.*

This experiment was undertaken at the same location as in *data Set-A,* shown in Figure 2.4. However, as it was conducted several months later, the range-Doppler contour plot has been computed again and an example for the first frame is shown in Figure 2.10. Here, the clutter region around $\mathcal{F} \approx 0$ is wider than in *data Set-A*. This notwithstanding, the effects for *data Set-B* are similar to those described for the *data Set-A* range-Doppler contour plot, with the target visible at -78.13 Hz.

The snapshots of $\underline{m}(t)$, at Point-A in Figure 1.6 for *data Set-B* (as provided by Saab) correspond to 12 Gold sequences, of length $\mathcal{N}_c = 2^9 - 1 = 511$, which all together provide a better code design than the single delayed sequence used to provide all the 12 codes in *data Set-A*.

Figure 2.11 shows the auto-correlation of the Gold sequence used for waveform 6, while an example of the cross-correlation can be seen between waveforms 1 and 6, in Figure 2.12 using *periodic* and *aperiodic* correlators. Note that, as expected, for periodic Gold sequences the cross-correlation is "3-valued", while the aperiodic is "random".

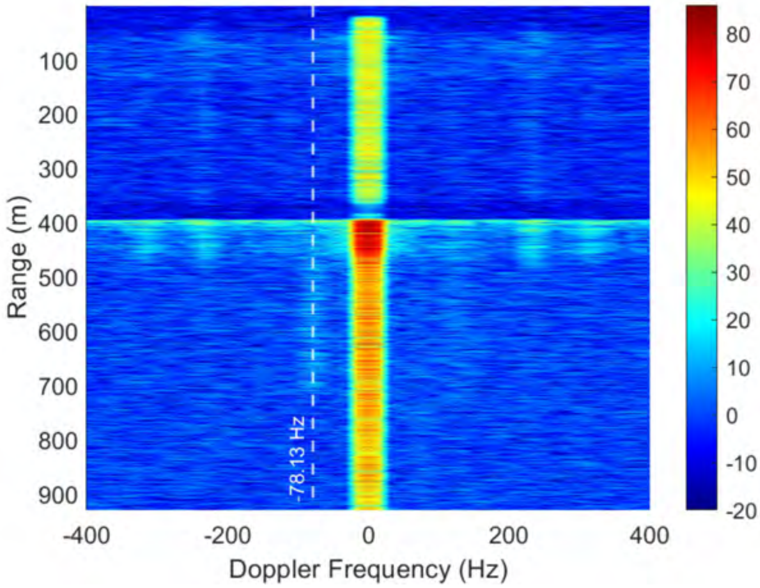

Figure 2.10: Range-Doppler contour plot for data Set-B, Frame 1

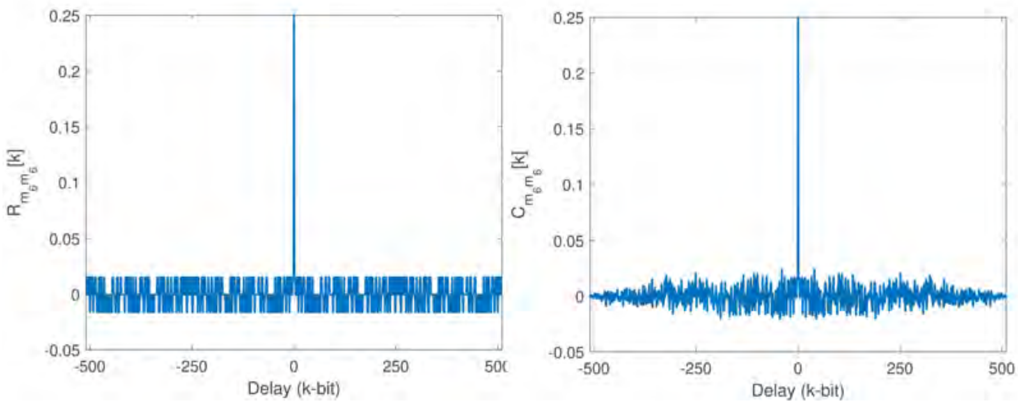

Figure 2.11: Auto-correlation function of the 6th code from data Set-B: LHS shows periodic, RHS shows aperiodic.

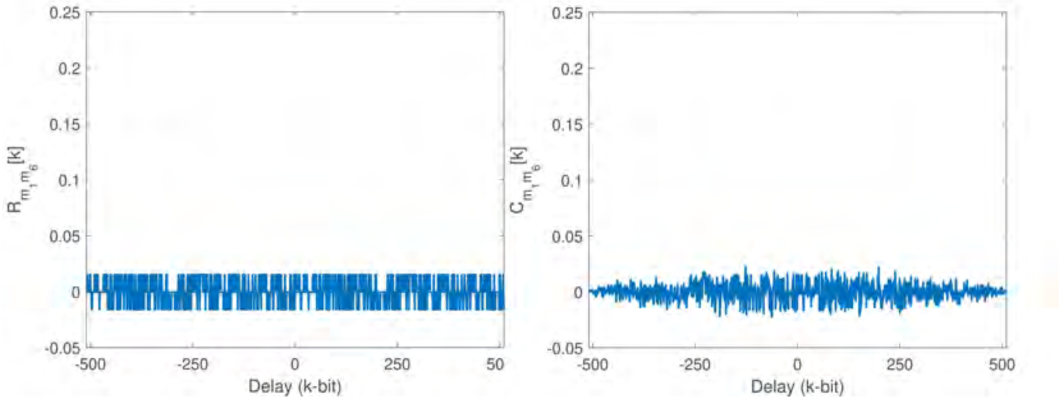

Figure 2.12: Cross-correlation of codes 1 and 6 from data Set-B: LHS shows periodic, RHS shows aperiodic.

2.5.3 Steps of the Estimation Procedure

For processing all sets of data, the general approach taken is provided in the following steps

- Step-1: Select received data $\underline{x}(t_\ell)\forall\ell \in \mathcal{C}^{N\times 1}$ for all 12-Rx streams in the data set; if there are calibration data available, remove antenna array uncertainties
- Step-2: identify the code data sets of snapshots $\underline{m}(t_\ell)\forall\ell$ define the necessary radar parameters, relevant to each data set;
- Step-3: perform a Fast Fourier Transform (FFT) to show the range-Doppler contour plot[4];
- Step-4: process the range-Doppler data for clutter removal;
- Step-5: compute the threshold for target detection in any given range bin;
- Step-6: implement the desired localisation algorithm. The main cost functions, for these MIMO localisation algorithms are detailed[5] in Table 2.1, and are listed here for convenience

[4] Other techniques may also be used for clutter filtering (see, for instance, [31]).

[5] Due to the "splitter" and "combiner" employed in the LRAM MIMO radar, the manifold vectors $\underline{S}$ and $\overline{\underline{S}}$ used in the cost functions of the algorithms given in Table-2.1, should be replaced as follows:

$$\text{data Set-A} \quad : \quad \begin{cases} \text{Tx: replace } \overline{\underline{S}} \text{ with } \overline{\underline{a}} = \overline{\mathbb{T}}\ \overline{\underline{S}} \\ \text{Rx: replace } \underline{S} \text{ with } \underline{a} = \mathbb{T}\ \underline{S} \end{cases}$$

  - LS,
  - Capon,
  - APES,
  - CAML,
  - MUSIC.

- Step-7: repeat the above steps for all frames.

Each algorithm estimates the DOA, that is azimuth (θ) and elevation (ϕ) angles, of the target to a precision of 1° for each data set, with the only exception being the MUSIC algorithm which has been adjusted/optimised to provide a very high precision. MUSIC is the only real super resolution algorithm from the list and, although it is not designed for MIMO systems, but a significant effort is made to adapt its operation to a MIMO radar environment.

The range resolution is different for each data set and is detailed in the relevant sections. It is a function of the duration T_c of a "chip", which is defined in the LRAM system specification, and hence cannot be improved in post-processing.

2.6 Experimental Signal Processing Results

In this section, figures showing representative results for DOA, range and velocity estimation, relating to each data set for selected algorithms and frames, along with complete tables of results are provided. Each subsection details any departures in array geometry from previously stated geometries and includes relevant details pertaining to parameters used in generating waveforms and relevant radar parameters.

$$\text{data Set-B} \quad : \quad \begin{cases} \text{Tx: use } \overline{\underline{S}} \text{ (no transformation)} \\ \text{Rx: replace } \underline{S} \text{ with } \underline{\mathrm{a}} = \mathbb{T}\,\underline{S} \end{cases}$$

where

- the matrix $\overline{\mathbb{T}}$ models the "splitter"
- the matrix $\mathbb{T}$ models the "combiner"

2.6.1 UAV Range & Azimuth Results for Data Set-A

With reference to Figure 1.6, at Point-Â, the signal data $\underline{x}(t_\ell)\forall\ell$ for $N = 12$ Rx streams is provided and for each channel there are 1000 radar pulses with PRI= 0.2 ms, forming a single frame. This is repeated to provide a total of 22 frames for *data Set-A*. Within each PRI, there are more than 400 range bins supplied (a number were removed by Saab), each providing a range resolution of 3.74741 m. The MIMO monostatic radar wireless channel model for a *multi-target* system is outlined in Figure 2.3 (see the "grey" area) and remains the model for *data Set-A*, for $M = 2$.

Figure 2.13 present the frame-by-frame estimated range[6] and DOA (azimuth only) for all 22 frames. The algorithms listed in Table 2.1 were employed for the estimation. The range axis is zoomed in to highlight the regions of interest only.

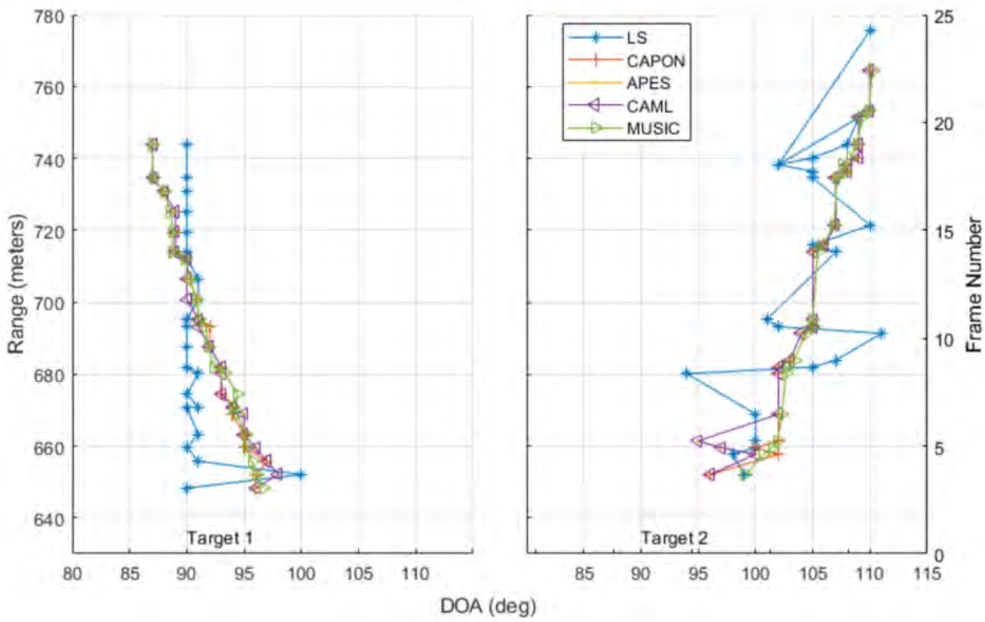

Figure 2.13: Range vs DOA, frame-by-frame estimates produced by all algorithms for data Set-A.

While the overall trend across the 22 frames appears accurately captured, the range estimates in some frames may suffer from reduced accuracy. This could

[6]For data set-A, there are 2 samples per T_c. That is, the sampling interval $T_s = T_c/2$ and the minimum range increment is 1.873705 m. However, the range resolution "unit" is T_c, which is twice that minimum increment (i.e. 3.74741 m).

be attributed to two factors: (1) limitations in the correlation properties of the code-set used in the first experiment, and (2) potential bias introduced due to the removal of data/range bins by Saab. Comparing the results in Figure 2.13, we observe consistent performance from the APES, Capon, MUSIC, and CAML algorithms, which instils confidence in the estimates. However, the LS algorithm consistently exhibits the poorest performance.

2.6.2 UAV Range & Azimuth Results for Data Set-B

With reference to Point-Â in Figure 1.6, received signal data $\underline{x}(t_\ell)\forall\ell$ for $N = 12$ Rx streams is provided. For each channel, there are 256 radar pulses with PRI= 0.25 ms, forming a single frame, repeated to provide a total of 4 frames for *data Set-B*. Within each PRI there are now 2000 range bins, each equating to a range resolution of 0.625 m. The model for the *single-target* MIMO radar wireless channel is provided in Figure 2.2 (see the "grey" area). The Tx array geometry for the LRAM-Radar in this experiment has been altered by Saab, and can be found in Figure 2.9.

The results for target localisation of a *single-target* using MIMO radar, for all the algorithms described above, are shown in Figure 2.14 for all 4 available frames.

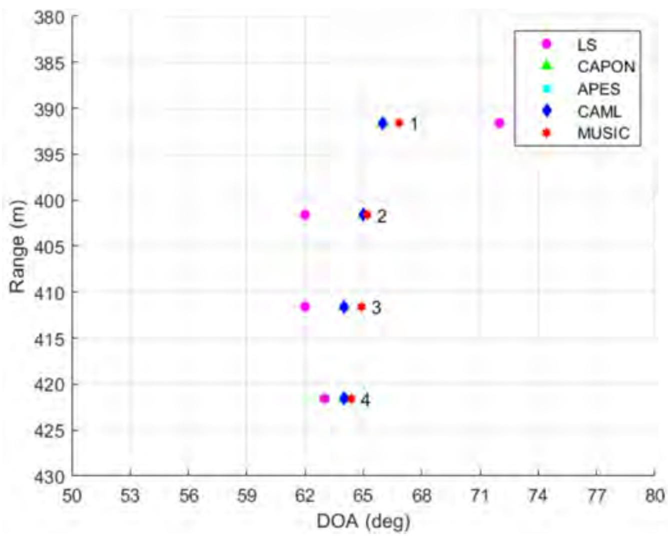

Figure 2.14: Frame-by-frame localisation of all algorithms for data Set-B over all 4 frames.

The results in Figure 2.14 demonstrate successful frame-by-frame localisation of a single target for four frames using the employed signal processing algorithms (APES, Capon, CAML, and MUSIC). All algorithms achieved consistent target locations across all frames. Similarly, in the results of *data set-A*, the LS algorithm again provides the poorest performance result. That is, estimates diverge from the other algorithms, with the divergence increased when the target is closer to the Rx array. However, with four of the five algorithms aligning to within 1° at each frame, there is a high degree of confidence in the accuracy of these results.

2.6.3 Virtual MIMO Radar for all Data Sets

In the "baseband signal processing" block (bottom right corner of Figure 1.6) the concept of the "extended manifolds" is introduced in [78], by including in the Rx manifold vector some additional system parameters such as orthogonal codes, delays, polarisation, etc. This concept has been utilised in [31] and [32] in MIMO radar - in the form of "virtual arrays" known as "virtual MIMO".

In particular, the baseband signal processor will transform the signal at Point-Â (see Equation 2.11) in a such a way that the new signal corresponds to the signal received by a larger Rx antenna array of "virtual" antennas (virtual array) with geometry given by the following equation:

$$\underbrace{[\underline{r}^v_1, \underline{r}^v_2, ..., \underline{r}^v_{\overline{N}N}]}_{\text{virtual-array geom.}} = \underbrace{[\underline{\overline{r}}_1, \underline{\overline{r}}_2, ..., \underline{\overline{r}}_{\overline{N}}]}_{\text{Tx-array geom.}} \otimes \underline{1}^T_N + \underline{1}^T_{\overline{N}} \otimes \underbrace{[\underline{r}_1, \underline{r}_2, ..., \underline{r}_N]}_{\text{Rx-array geom.}} \tag{2.27}$$

Equation 2.27 is known as "spatial convolution" between the Tx and the Rx antenna array geometries. The result is a virtual array with $\overline{N}N$ virtual antennas having a much larger aperture (i.e. more powerful) than the real Rx antenna array. However, considerable design planning for the Tx and Rx array geometries is required to utilise the full potential of the "virtual array", as the spatial convolution may result in "overlapping" virtual antennas.

The concept of the virtual array in a MIMO radar can be visualised as the virtual transfer of the Tx antennas from the transmitter, via the channel, to the receiver [79]. This can be done using a number of equivalent operations based on the three basic rules for addition and multiplication: the "Commutative", the "Distributive" and the "Associative" rules.

It is important to point out that the virtual array of Equation 2.27 has a manifold vector (virtual manifold vector $\underline{S}_v$) which is related to the Tx and Rx manifold vectors of the real MIMO system as follows:

$$\underline{S}_{\text{virtual}} \triangleq \overline{\underline{S}}^* \otimes \underline{S} \tag{2.28}$$

By suitably transforming the received signal $\underline{x}(t)$ at Point-Â in Figure 2.3 (given by Equation 2.11 which is the discretised version of Equation 2.10a) we can produce another signal $\underline{x}_v(t)$ which is known as "virtual" signal. This signal is a function of the virtual manifold vector $\underline{S}_v$ given by Equation 2.28 that corresponds to the "virtual" array geometry of Equation 2.27. In this case the virtual radar channel can be modelled as shown[7] in Figure 2.15 where, now, all the vector-signals ("blue" arrows) have $\overline{N}N$ scalar virtual elements equal to the number of elements of the virtual antenna array. There are several ways to transform $\underline{x}(t)$ to the virtual $\underline{x}_v(t)$. In this section, the property of "orthogonality" of the code signal $\underline{m}(t)$ is used, to implement the concept of the "virtual MIMO".

In virtual MIMO radar signal processing, transforming the received signal $\underline{x}(t)$ into the virtual signal $\underline{x}_v(t)$ increases the dimensionality of the observation space, which inevitably leads to higher computational complexity compared to classical MIMO localisation algorithms (Table 2.1). This approach is applicable to both monostatic and bistatic configurations. However, in bistatic scenarios, the physical separation of Tx and Rx antennas prevents a true virtual array. Instead, a virtual array manifold (characterised by Equation 2.28) is utilised to achieve similar benefits. These benefits include:

- increased array aperture
- capable of handling targets more than the number of Rx antennas N
- improved localisation accuracy

[7] For simplicity, in Figure 2.15 the blocks of the splitter $\overline{\mathbb{T}}$ and the combiner $\mathbb{T}$ have been ignored.

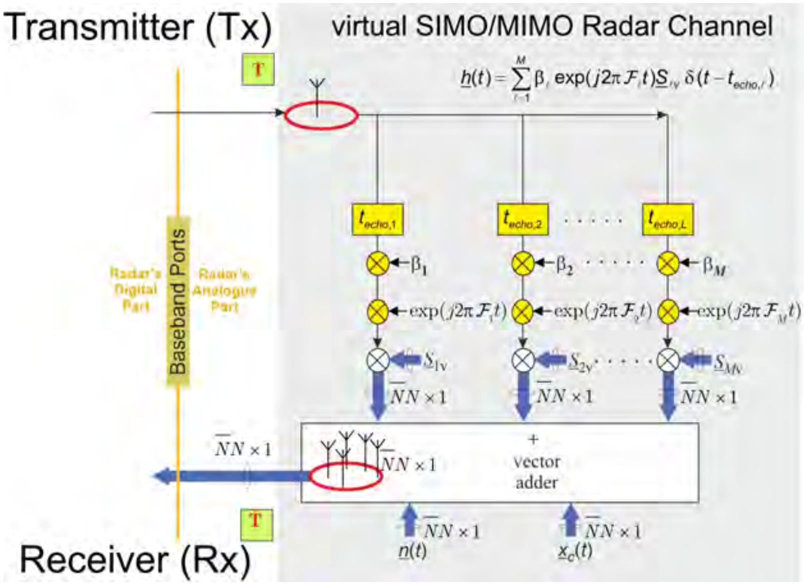

Figure 2.15: Multi-target virtual radar channel

In this section, the concept of the virtual array will be used in conjunction with selected virtual MIMO algorithms. This implies that firstly the Rx signal $\underline{x}(t) \in \mathcal{C}^{N\times1}$ should be transformed to the virtual signal $\underline{x}_v(t) \in \mathcal{C}^{\overline{N}N\times1}$. More specifically, the Rx snapshots $\underline{x}(t_\ell)\forall\ell$ should be transformed to the virtual signal snapshots $\underline{x}_v(n)\forall n$ by the Rx baseband signal processor, shown in Figure 1.6. As stated before, there are several ways to transform $\underline{x}(t)$ to the virtual $\underline{x}_v(t)$. In this section, the "orthogonality" property of the code signal $\underline{m}(t)$ will be used.

In simple terms, without any proof, this means

$$\underbrace{\underline{x}_v(t)}_{\overline{N}\cdot N\times1} = \underbrace{\underline{x}(t)}_{N\times1} \otimes \underbrace{\underline{m}(t)}_{\overline{N}\times1} \tag{2.29}$$

and then apply one of the "virtual" algorithms, the cost functions of which are given in Table-2.2. In all data sets:

1) the number of targets is smaller than the number of Rx antenna array elements N and, consequently, the problem of more targets than the number of Rx antenna elements cannot be examined; and

2) the improved localisation accuracy cannot be shown as the true target location is unknown.

Table 2.2: Virtual MIMO localisation algorithms

Algorithm	Main Cost Function (variables: azimuth θ and elevation ϕ)
Virtual Steering Vector	$\xi(\theta,\phi) = \dfrac{\underline{S}_v^H(\theta,\phi)\mathbb{R}_{x_v x_v}\underline{S}_v(\theta,\phi)}{(\overline{N}N)^2}$
Virtual Capon	$\xi(\theta,\phi) = \dfrac{1}{\underline{S}_v^H(\theta,\phi)\mathbb{R}_{x_v x_v}^{-1}\underline{S}_v(\theta,\phi)}$
Virtual MUSIC	$\xi(\theta,\phi) = \dfrac{\underline{S}_v^H(\theta,\phi)(\mathbb{I}_N - \mathbb{E}_{n_v}\mathbb{E}_{n_v}^H)\underline{S}_v(\theta,\phi)}{\underline{S}_v^H(\theta,\phi)\underline{S}_v(\theta,\phi)}$ or equivalently $\xi(\theta,\phi) = \dfrac{\underline{S}_v^H(\theta,\phi)\underline{S}_v(\theta,\phi)}{\underline{S}_v^H(\theta,\phi)\mathbb{E}_{n_v}\mathbb{E}_{n_v}^H\underline{S}_v(\theta,\phi)}$ where $\mathbb{E}_{n_v}$ = virtual "noise" subspace eigenvectors

Hence, here it is demonstrated that the elevation angle (ϕ), together with the azimuth angle (θ), in the cases where the "classical" MIMO algorithms failed. This can be done only for the case that the virtual array is a non-linear array. This implies that the elevation angle for data sets B can be estimated, as its virtual array geometry is "planar" (see Figure 2.24 in Appendix B).

Figures 2.16a and 2.16b present the estimated values obtained using the three virtual MIMO algorithms listed in Table 2.2. These algorithms were applied to *data Set-B*. The results, which are summarised in Table 2.3, show close agreement between the virtual MIMO algorithms for all four available frames.

Table 2.3: MIMO Radar Dataset B: Summary of Localization Results

Algorithm	**Frame**	**Range Bin**	**Range (m)**	**DOA (θ)**	**DOA (ϕ)**
Virtual Steering Vector	1	627	391.60	65.9°	3.6°
	2	643	401.60	65.3°	3.3°
	3	659	411.59	64.7°	3.5°
	4	675	421.58	64.0°	3.8°
Virtual Capon	1	627	391.60	65.9°	3.9°
	2	643	401.60	65.3°	3.6°
	3	659	411.59	64.7°	3.8°
	4	675	421.58	64.0°	4.2°
Virtual MUSIC	1	627	391.60	65.93°	3.86°
	2	643	401.60	65.34°	3.51°
	3	659	411.59	64.74°	3.70°
	4	675	421.58	64.04°	4.09°

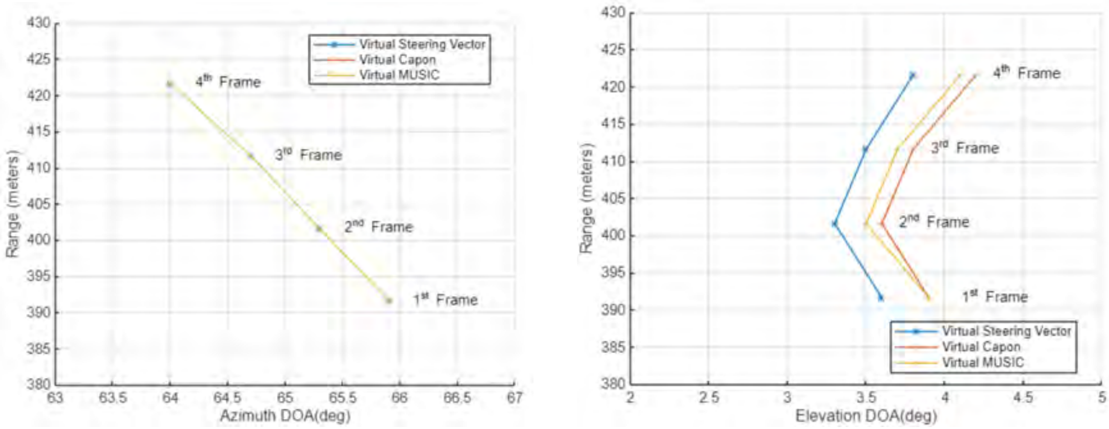

(a) Range vs DOA(Azimuth) (b) Range vs DOA(Elevation)

Figure 2.16: Virtual algorithms Range vs DOA frame-by-frame estimates (all frames, data Set-B)

2.7 Summary

This chapter explores the Saab LRAM MIMO Radar, examining the radar system architecture in detail and providing models for the baseband signal processor and wireless MIMO radar channel. The chapter investigates a range of established MIMO signal processing algorithms, alongside three innovative "virtual" MIMO algorithms, including a virtual adaptation of the MUSIC algorithm. It systematically guides through the estimation of target parameters (azimuth, elevation, range, and velocity) with illustrative results.

The chapter begins with a detailed introduction to Saab's LRAM experimental radar, followed by an overview of the LRAM antenna array. It elaborates on the monostatic MIMO radar channel model, starting with single-target scenarios and expanding to multi-target cases. Established MIMO radar algorithms for parameter estimation are then discussed. The chapter also provides a detailed account of MIMO radar experiments conducted by Saab, including the setup, experimental environment, and procedures for extracting DOA and range estimates. Challenges encountered with the PN-code used in one data set are analysed, and the advantages of using Gold sequences in another are highlighted.

The results from applying MIMO algorithms to both data sets are presented, showing the consistent performance of Capon, APES, CAML, and MUSIC algorithms, particularly after the 5th frame, and noting the underperformance of the LS algorithm. The concept of virtual arrays is introduced, explaining their significance and applicability, and demonstrating the efficacy of three virtual MIMO algorithms in estimating target azimuth and elevation.

This research explores the potential of virtual MIMO for radar target localisation and parameter estimation. The results pave the way for further investigation into the development and application of virtual MIMO algorithms in radar systems.

2.8 Appendices

Appendix 2.A: UAV Velocity Results for all Data Sets

To estimate the velocity of the UAVs, firstly the Doppler Spectrum is computed in the interval [-PRF/2, +PRF/2], where PRF/2 is the Doppler bandwidth. In particular, the FFT of the "slow time" samples of the received data $\underline{x}(t_\ell)\forall\ell$ (related to a particular range bin in a single frame), will provide the Doppler Spectrum in the interval [-PRF/2, +PRF/2], which is partitioned in a number of Doppler-bins. If the target is present in a given range bin then it will appear in the Doppler Spectrum corresponding to that range bin. It is from this Doppler frequency that the velocity can be estimated.

For *data Set-A,* a representative example of velocity estimation of the two UAVs is given in Figure 2.17. This has been produced by using the data for Frame-5 and for a range bin where the echo signals of two UAVs targets overlap with each other (around 830 m). Note that Figure 2.17 is a horizontal slice of the contour map plot shown in Figure 2.6. From Figure 2.17, the UAVs' velocities can be easily estimated from the two strong peaks at Doppler frequencies -65 Hz and -95 Hz. The terrestrial clutter is also shown around 0 Hz in the top figure, which has been removed from the bottom figure. Note that the Doppler Spectrum interval, which should be between -2.5 kHz and $+2.5$ kHz (as the PRF is 5 kHz for *data Set-A*) has been truncated in Figure 2.17 to between -250 Hz and 250 Hz, as the Doppler bandwidth is unnecessarily large. Due to high value for the clutter, the vertical axis has also been truncated to better visualise the target response.

A similar representative example is also given for the *data Set-B* (Frame-1, range bin around 530 m) in Figure 2.18 - before and after clutter filtering. In his case, the estimated Doppler frequency is -78.13 Hz. Again the Doppler Spectrum has been truncated in the region -1 kHz to $+1$ kHz (the PRF for *data Set-B* is 4 kHz) while the vertical axis has been also truncated to better visualise the target response. Figure 2.19 presents the velocity estimates of two targets for all 22 frames, for *data Set-A*. It can be seen the velocities of both targets in *data Set-A* are increasing, however for *data Set-B*, the velocity of the target remains constant at -9.0082 m/s for all 4 available frames and this is shown in Figure 2.20. Note that the minus sign indicates that the targets are moving away from the radar platform for both data sets.

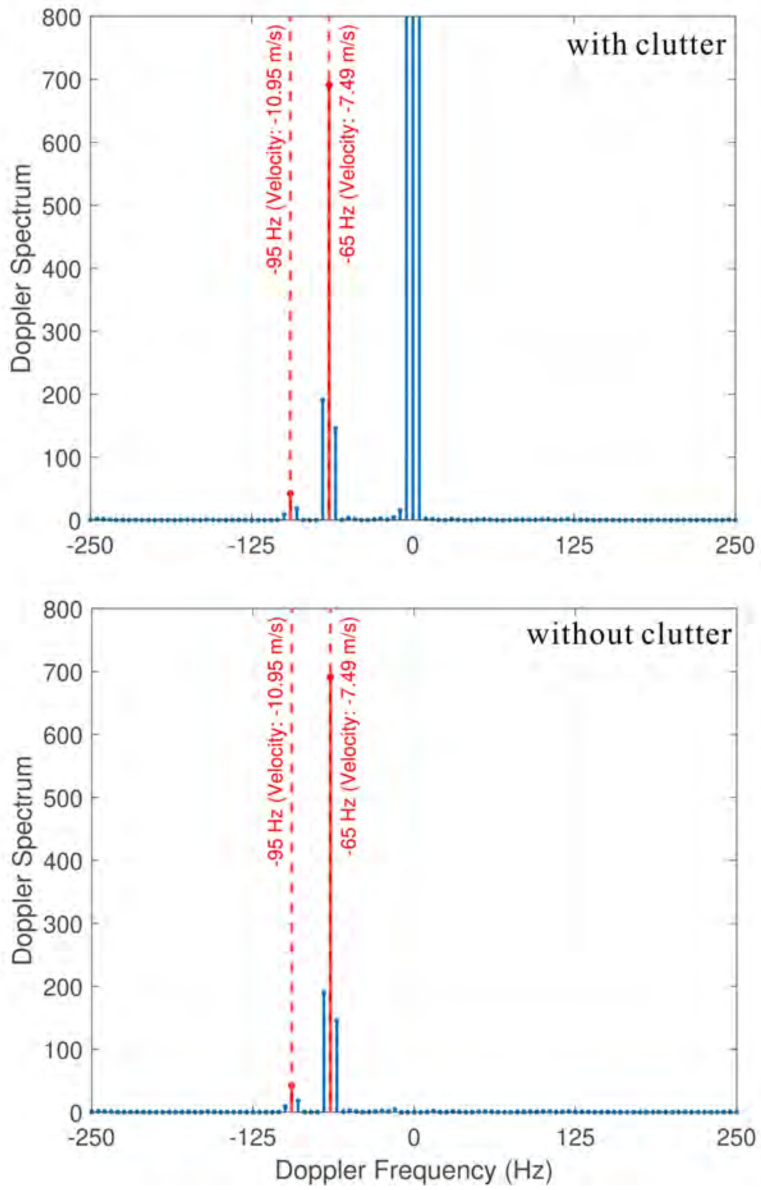

Figure 2.17: Data Set-A Doppler spectrum (for a range bin around 830m in Frame-5).

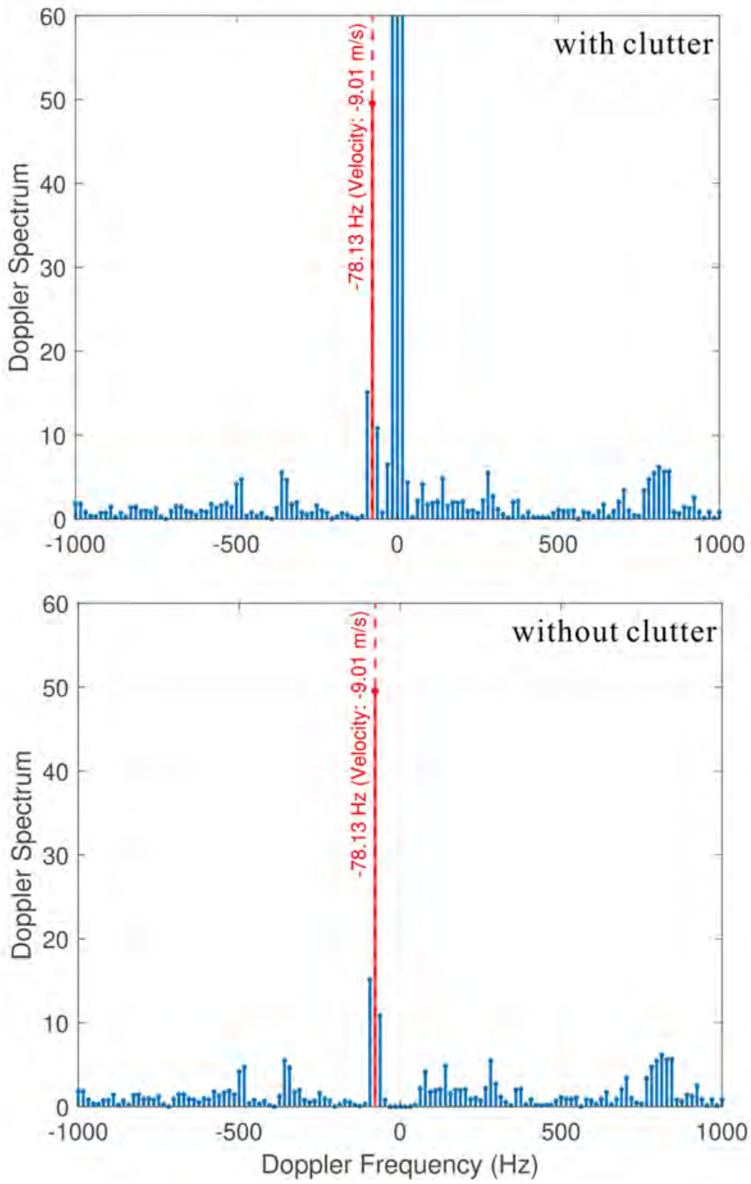

Figure 2.18: Data Set-B Doppler spectrum (for a range bin around 530m in Frame-1).

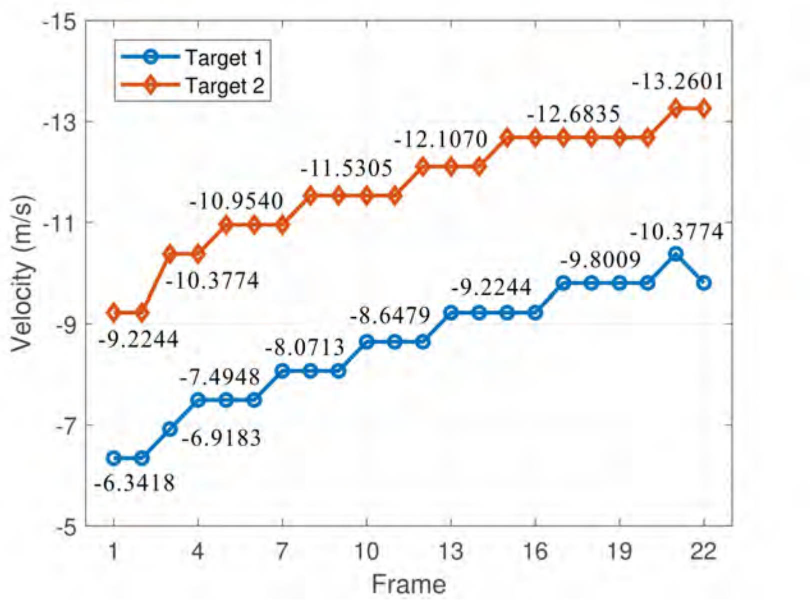

Figure 2.19: Velocity estimation of the two targets across 22 frames in data Set-A.

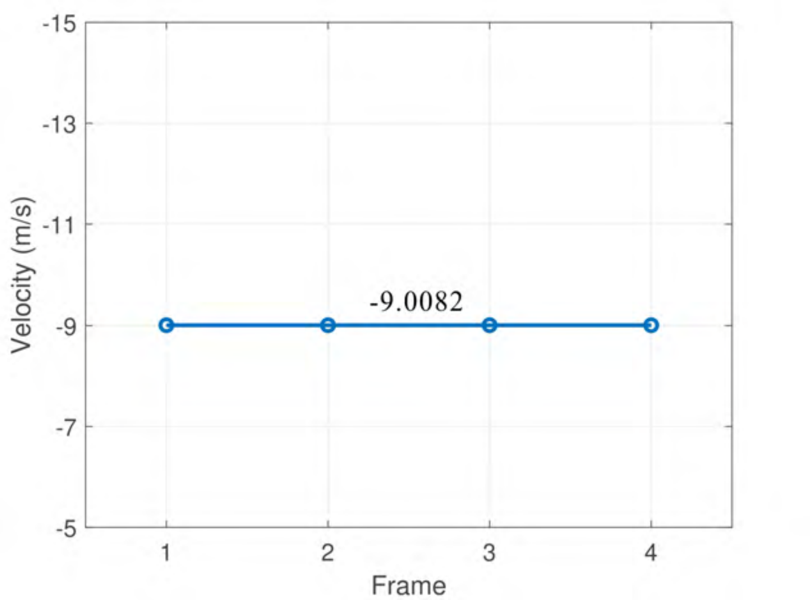

Figure 2.20: Velocity estimation of the single UAV across 4 frames in data Set-B.

Appendix 2.B: Virtual Antenna Array Formation

The antenna array configuration used for the *data Set-A* is shown in Figure 2.5. This is a planar array with an equal number of Tx and Rx antennas $\bar{N}' = N' = 24$ and fixed inter-element spacing $d = 10$ cm. This means each Tx and Rx chain is connected with two antennas through a splitter and combiners network. The splitting and combining process is modelled through the transformation matrices $\overline{\mathbb{T}}$ and $\mathbb{T}$ - the $\overline{\mathbb{T}}/\mathbb{T}$ transformation will henceforth be referred to as Splitter/Combiner (S/C) transformation. According to Equation 2.27, the virtual array geometry can be directly investigated. Before the S/C transformation stage, the virtual array is formed as shown in Figure 2.21. The expected array size is $\bar{N}' \times N' = 24 \times 24 = 576$ elements, however, Figure 2.21 shows only 69 elements of the planar array and the rest are overlapping elements i.e. share the exact location. This virtual antenna array geometry is undesirable: resulting in many overlapping virtual elements, is a poor allocation of resources, offering a reduced degree of freedom and loss of resolution. Figure 2.22 shows the virtual array after the S/C-transformation stage and expects $\overline{N} \times N = 12 \times 12 = 144$ elements but only 23 are visible for the reasons just outlined. It is important to point out, although this virtual array has increased aperture, it is still of linear geometry and hence remains incapable of estimating the elevation angles. For *data Set-B*, the array configuration is shown in Figure 2.9 with $\overline{N}' = 12$, $N' = 24$ and spacing $d = 10$ cm. This array has half the number of Tx antennas which are divided into two columns separated by $10 \times d$ along the x-axis. The virtual array has $\overline{N} \times N = 12 \times 24 = 288$ elements but with many overlapping elements.

In Figure 2.23 only $23 \times 7 = 161$ are shown before the S/C-transformation stage as the rest are overlapping - having the same locations. The virtual array after the S/C-transformation, shown in Figure 2.24, has $\overline{N} \times N = 12 \times 12 = 144$ elements but only $23 \times 6 = 138$ are shown are the rest are overlapping.

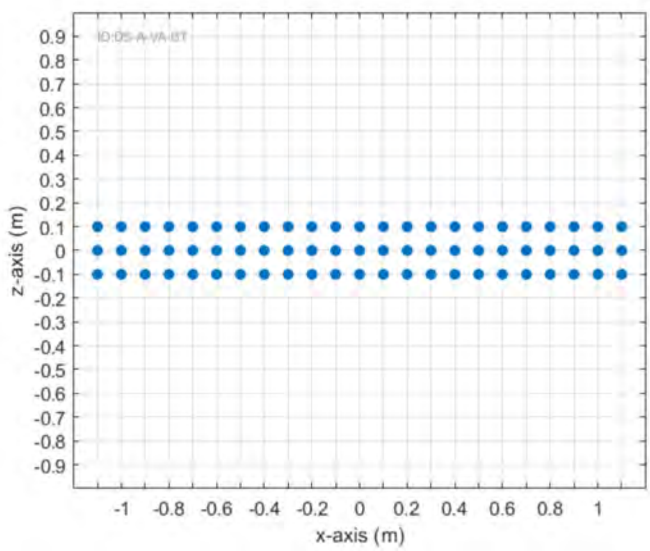

Figure 2.21: Data Set-A virtual antenna array geometry with $\overline{N}' = N' = 24$ (before S/C-transformation). $N_{virtual} = 576$.

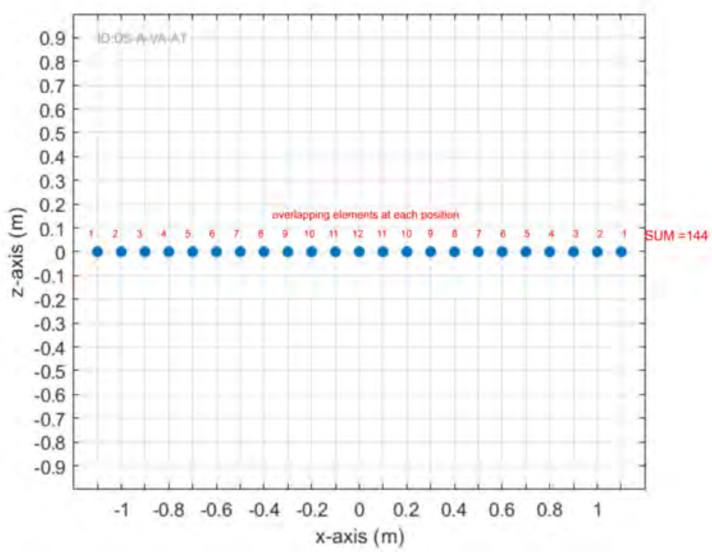

Figure 2.22: Data Set-A virtual antenna array geometry with $\overline{N} = N = 12$ (after S/C-transformation). $N_{virtual} = 144$

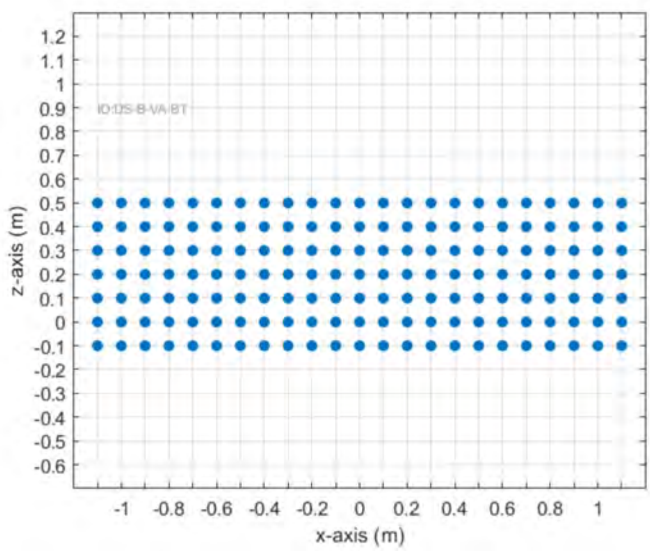

Figure 2.23: Data Set-B virtual antenna array geometry with $\overline{N}' = 12$ and $N' = 24$ (before S/C-transformation).

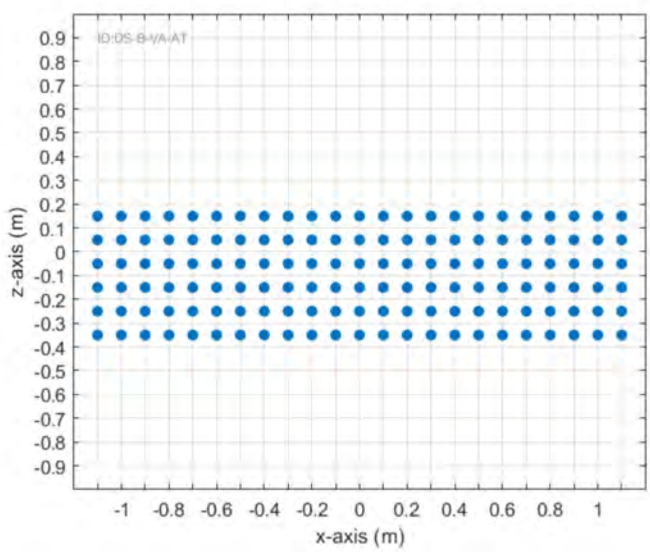

Figure 2.24: Data Set-B virtual antenna array geometry with $\overline{N} = 12$ and $N = 12$ (after transformation).

Chapter 3

Bistatic MIMO Radar: Localisation Using Tx Slow Time Codes

In this chapter, innovative subspace-based algorithms employing Slow Time Codes (STC) are introduced for estimating parameters of multiple moving or static targets in bistatic MIMO radar systems. The target's parameters of interest include delay/range, DOA, DOD, Doppler frequency and complex path coefficient, which is a function of the target's bistatic RCS. Based on parametric bistatic pulse MIMO radar signal models in conjunction with the concept of extended array manifolds, subspace-based algorithms are proposed for estimating these parameters without suffering from estimates association problem. The performance of the proposed algorithms is evaluated using computer simulation studies.

3.1 Introduction

Modern radar systems such as MIMO radars in both monostatic [31, 70, 80] and bistatic/multi-static architectures are designed with goals of achieving superior target parameter identifiability, estimation accuracy, and super resolution capabilities. In this chapter, the bistatic MIMO radar is employed which has many obvious advantages over its monostatic counterpart, such as undetectable receivers, counter-stealth capabilities, reduced susceptibility to jamming, etc [81][82]. Most importantly, as the transmitter and receiver of a bistatic MIMO radar are far away from each other, they view each target from different perspectives, and the DOD is different from the DOA. In monostatic MIMO radar, the DOA and DOD are equal, and thus the DOA is important to be estimated from the received data.

In bistatic MIMO radar, both the DOA and DOD are important and should be estimated from the received data. In [83], a 2-dimensional (2D) Capon spectrum is proposed for joint DOA and DOD estimation, which belongs to the family of beamforming and suffers from low spatial resolution. In addition, the ML estimator, though optimum, requires to address the computational prohibitive higher order nonlinear optimisation problem [84]. Another wide range of algorithms is subspace-based, thus possessing super-resolution capabilities [85–88]. In [85], a reduced-dimension (RD) MUSIC algorithm is proposed. The Estimation of Signal Parameters Via Rotational Invariance Techniques (ESPRIT) algorithm is extended in [86] to an iterative algorithm with improved reliability and parameter identifiability. Special non-uniform linear arrays have also been exploited to incorporate more DOFs, thus improving the overall performance [87][88]. By stacking the received (processed) slow-time data in a tensor format, Parallel Factor (PARAFAC) decomposition based techniques can also be used [89][90]. It is worth pointing out that all the aforementioned algorithms were developed assuming the absence of relative target path delays.

In this chapter, parametric signal models for a bistatic pulse MIMO radar are developed which support the inclusion of Tx and Rx array geometries, operational frequency, PRI, target's delay, DOA, DOD, Doppler frequency and complex path coefficient. Based on multiple received PRI data matrices, a novel array "manifold extender", which follows the theoretical framework of [78], is employed which incorporates the target's DOD, Doppler frequency and the transmit vector symbols into the Rx manifold vector. Then, subspace-based algorithms are proposed to estimate various parameters of each target in sequential order. It should be noted that the proposed estimation approach automatically associates different estimated parameters to the same target, thus avoiding the estimates' association difficulties.

This chapter is organised as follows. In Section 3.2, the transmit and receive signal models are presented. In Section 3.3, a novel array "manifold extender" is proposed by vertically concatenating PRI data matrices to form an "extended" Rx data matrix. Then, based on the extended data matrix, subspace-based algorithms are proposed in Section 3.4 using the concept of the extended array manifold vectors for estimating DOA, DOD, Doppler frequency, delay/range, and complex path coefficient of all the targets. Computer simulation studies are presented in Section 3.5 demonstrating the performance of the proposed algorithms. Finally, the chapter is concluded in Section 3.6.

3.2 Signal Modelling

Consider a bistatic pulse MIMO radar system which employs a Tx array of $\overline{N}$ antennas and a Rx array of N antennas. Without loss of generality, both the Tx and Rx arrays are assumed to be fully calibrated with known geometries measured with respect to their own reference points. The Cartesian coordinates of these two arrays are represented, in meters, by the matrices $\overline{\mathbf{r}} \in \mathcal{R}^{3\times\overline{N}}$ and $\mathbf{r} \in \mathcal{R}^{3\times N}$, respectively.

3.2.1 Transmit

Consider the Tx-array transmits a vector of rectangular pulses modulated by a vector symbol $\underline{a}[n] \in \mathcal{C}^{\overline{N}\times 1}$ in the n-th PRI. Moreover, the sequence of these vector symbols is assumed to be periodic with a period equal to $\mathcal{N}_s$. Without loss of generality, let's consider a complete frame of the transmit waveform, which comprises $\mathcal{D}$ subframes. Each subframe contains a full period of vector symbols $\underline{a}[1], \underline{a}[2], \ldots, \underline{a}[\mathcal{N}_s]$, collectively forming the matrix $\mathbb{A}$, denoted as $\mathbb{A} \triangleq [\underline{a}[1], \underline{a}[2], \ldots, \underline{a}[\mathcal{N}_s]]$. These symbols are commonly referred to as STCs. That is, there are $\mathcal{D}\mathcal{N}_s$ PRIs per frame. Additionally, each vector symbol undergoes modulation using a pulse compression code consisting of $\mathcal{N}_c$ chips to enhance range resolution. This pulse compression code is also known as the fast time code (FTC). Therefore, the transmit data sequence in the n-th PRI can be modelled as

$\underline{a}[n]\underline{\mathfrak{c}}^T$ where the vector $\underline{\mathfrak{c}} \in \mathcal{R}^{L\times 1}$ is defined as

$$\underline{\mathfrak{c}} \triangleq [\underbrace{\mathfrak{c}[1], \mathfrak{c}[2], \ldots, \mathfrak{c}[\mathcal{N}_c]}_{\text{pulse compression code}}, \underbrace{0, 0, \ldots, 0}_{L-\mathcal{N}_c}]^T, \tag{3.1}$$

where $L > \mathcal{N}_c$ is the number of compressed range bins within each PRI. Given that the duration of each pulse compression code symbol is T_c (as shown in Equation 3.1), the PRI can be expressed as PRI $= LT_c$. Additionally, the uncompressed pulse duration T_p is assumed to be equal to $\mathcal{N}_c T_c$.

3.2.2 Receive

Consider that the radar operates in the presence of K targets. Then, the n-th discrete received data matrix $\mathbb{X}[n] \in \mathcal{C}^{N\times L}$ associated with the n-th PRI can be modelled as

$$\begin{aligned}\mathbb{X}[n] = \sum_{k=1}^{K} &\beta_k \exp\left(j2\pi\mathfrak{f}_k(n-1)LT_c\right) \\ &\underline{S}_k\underline{\overline{S}}_k^H \underline{a}[n]\left(\mathbb{J}^{l_k}\underline{\mathfrak{c}}\right)^T + \mathbb{N}[n],\end{aligned} \tag{3.2}$$

where β_k is the complex path gain/coefficient, which is a function of the k-th target's bistatic RCS, and $\mathfrak{f}_k$ denotes the bistatic Doppler frequency. In Equation 3.2, the vectors $\underline{\overline{S}}_k$ and $\underline{S}_k$ represent the k-th target's Tx and Rx array manifold vectors, respectively, which can be expressed as

$$\underline{\overline{S}}_k \triangleq \underline{\overline{S}}\left(\overline{\theta}_k\right) = \exp\left(+j\frac{2\pi F_c}{c}\overline{\mathbf{r}}^T\underbrace{[\cos\overline{\theta}_k, \sin\overline{\theta}_k, 0]^T}_{=\underline{u}(\overline{\theta}_k)}\right), \tag{3.3}$$

$$\underline{S}_k \triangleq \underline{S}\left(\theta_k\right) = \exp\left(-j\frac{2\pi F_c}{c}\mathbf{r}^T\underbrace{[\cos\theta_k, \sin\theta_k, 0]^T}_{=\underline{u}(\theta_k)}\right), \tag{3.4}$$

where F_c is the carrier frequency, c represents the velocity of light, $\overline{\mathbf{r}}$ and $\mathbf{r}$ are the 3D coordinate matrices for the Tx and Rx antenna arrays, while $\overline{\theta}_k$ and θ_k denote the k-th target's azimuth DOD and DOA, respectively. Note that in Equations 3.3

and 3.4, zero elevation has been assumed for simplicity. Furthermore, l_k denotes the quantised propagation delay of the k-th target τ_k relative to the direct Tx-Rx path, i.e. $l_k = \lceil \tau_k / T_c \rceil$, and the matrix $\mathbb{J}$ is a $L \times L$ lower shift matrix defined as

$$\mathbb{J} \triangleq \begin{bmatrix} \underline{0}_{L-1}^T & 0 \\ \mathbb{I}_{L-1} & \underline{0}_{L-1} \end{bmatrix} = \begin{bmatrix} 0, & 0, & \cdots & 0, & 0 \\ 1, & 0, & \cdots & 0, & 0 \\ 0, & 1, & \cdots & 0, & 0 \\ \vdots & \vdots & \ddots & \vdots & \vdots \\ 0, & 0, & \cdots & 1, & 0 \end{bmatrix}. \tag{3.5}$$

Finally, the matrix $\mathbb{N}[n] \in \mathcal{C}^{N \times L}$ contains the received snapshots during the n-th PRI, representing the additive white Gaussian noise (AWGN) of zero mean and covariance matrix $\sigma_n^2 \mathbb{I}_N$. For notational convenience, it is assumed that the clutter has been removed using FFT (in the case of static clutter) or using the clutter pre-processing scheme presented in [31].

3.3 Manifold Extender

An array "manifold extender" [78] incorporates additional system parameters into the original Rx array manifold, forming the extended array manifolds. This can be achieved via a group of Tapped Delay Lines (TDLs) or through certain mathematical operations, e.g. [31]. In this section, a novel "manifold extender" is proposed based on re-arrangement of the received PRI data matrices. It can be proven (see Appendix A) that the data matrix $\mathbb{X}[n] \in \mathcal{C}^{N \times L}$ modelled by Equation 3.2 can be rewritten as

$$\begin{aligned} \mathbb{X}[n] = \sum_{k=1}^{K} & \beta_k \exp\left(j 2\pi \mathfrak{f}_k (n-1) L T_c\right) \\ & \left(\underline{a}^T[n] \otimes \mathbb{I}_N\right) \underline{S}_{\mathrm{v},k} \left(\mathbb{J}^{l_k} \underline{\mathfrak{c}}\right)^T + \mathbb{N}[n], \end{aligned} \tag{3.6}$$

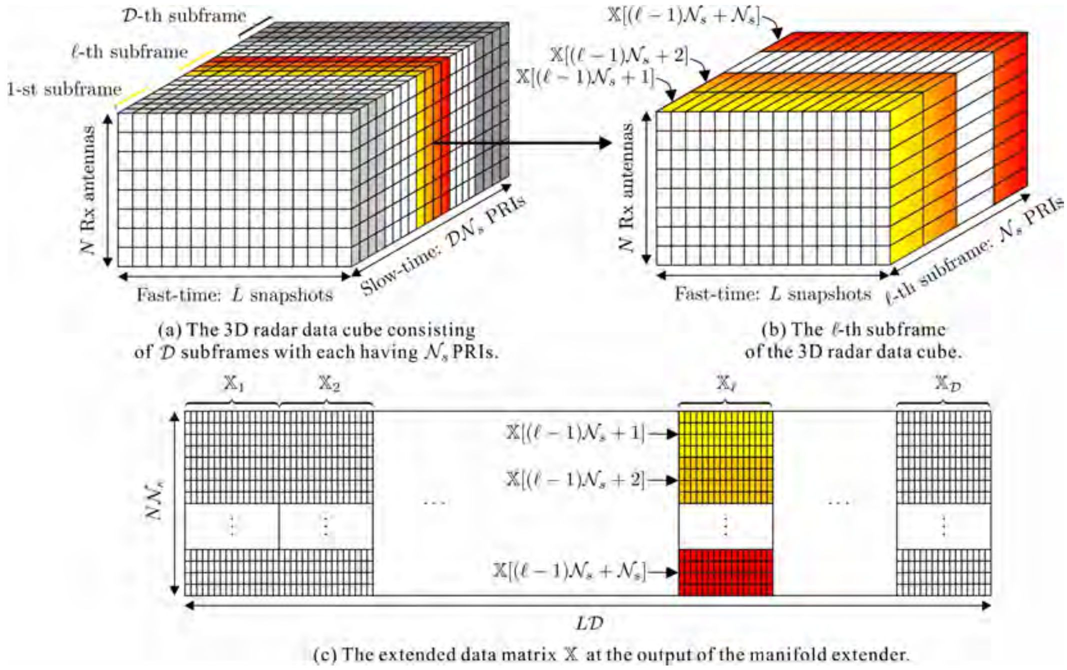

Figure 3.1: Manifold extender through PRI data matrices re-arrangement.

where $\underline{S}_{\mathrm{v},k} \triangleq \underline{S}_{\mathrm{v}}\left(\theta_k, \overline{\theta}_k\right) \in \mathcal{C}^{N\overline{N}\times 1}$ represents the virtual manifold vector of the k-th target and is given as

$$\begin{aligned}\underline{S}_{\mathrm{v},k} &= \underline{\overline{S}}^{*}\left(\overline{\theta}_k\right) \otimes \underline{S}\left(\theta_k\right) \\ &= \exp\left(-j\frac{2\pi F_c}{c}\left(\overline{\mathbf{r}}^T\underline{u}\left(\overline{\theta}_k\right) \oplus \mathbf{r}^T\underline{u}\left(\theta_k\right)\right)\right)\end{aligned} \tag{3.7}$$

where the symbols $\otimes$ and $\oplus$ represent Kronecker product and sum, respectively.

With reference to Figure 3.1, by vertically concatenating the received $\mathcal{N}_s$ PRI data matrices corresponding to the ℓ-th subframe of the transmit symbols, the extended data matrix $\mathbb{X}_\ell$ can be obtained and written explicitly as

$$\begin{aligned}\mathbb{X}_\ell &\triangleq \begin{bmatrix} \mathbb{X}[(\ell-1)\mathcal{N}_s+1] \\ \mathbb{X}[(\ell-1)\mathcal{N}_s+2] \\ \vdots \\ \mathbb{X}[(\ell-1)\mathcal{N}_s+\mathcal{N}_s] \end{bmatrix} \in \mathcal{C}^{N\mathcal{N}_s\times L} \\ &= \sum_{k=1}^{K}\beta_k \underbrace{\left(\mathrm{diag}\left(\underline{\mathcal{F}}_{\ell k}\right)\mathbb{A}^T \otimes \mathbb{I}_N\right)\underline{S}_{\mathrm{v},k}}_{=\underline{h}_{\ell k}\triangleq\underline{h}_{\ell}\left(\theta_k,\overline{\theta}_k,\mathfrak{f}_k\right)}\left(\mathbb{J}^{l_k}\underline{\mathfrak{c}}\right)^T + \mathbb{N}_\ell,\end{aligned} \tag{3.8}$$

where

$$\underline{\mathcal{F}}_{\ell k} = \underbrace{\begin{bmatrix} 1 \\ \exp(j2\pi\mathfrak{f}_k LT_c) \\ \vdots \\ \exp(j2\pi\mathfrak{f}_k(\mathcal{N}_s - 1)LT_c) \end{bmatrix}}_{\triangleq \underline{\mathcal{F}}(\mathfrak{f}_k)} \exp(j2\pi\mathfrak{f}_k(\ell-1)\mathcal{N}_s LT_c) \tag{3.9}$$

represents the Doppler shifts over $\mathcal{N}_s$ PRIs within the ℓ-th subframe and

$$\mathbb{N}_\ell \triangleq \begin{bmatrix} \mathbb{N}[(\ell-1)\mathcal{N}_s + 1] \\ \mathbb{N}[(\ell-1)\mathcal{N}_s + 2] \\ \vdots \\ \mathbb{N}[(\ell-1)\mathcal{N}_s + \mathcal{N}_s] \end{bmatrix} \in \mathcal{C}^{N\mathcal{N}_s \times L} \tag{3.10}$$

is the extended noise matrix. Note that, by neglecting the scalar Doppler shift associated with the ℓ-th subframe, i.e. $\exp\left(j2\pi\mathfrak{f}_k(\ell-1)\mathcal{N}_s LT_c\right)$, the virtual array manifold vector $\underline{S}_{\mathrm{v},k}$ in Equation 3.8 is transformed by a transformation matrix $\mathbb{T}_k$ defined as

$$\mathbb{T}_k \triangleq \mathbb{T}\left(\mathfrak{f}_k\right) = \mathrm{diag}\left(\underline{\mathcal{F}}\left(\mathfrak{f}_k\right)\right) \mathbb{A}^T \otimes \mathbb{I}_N \in \mathcal{C}^{N\mathcal{N}_s \times N\overline{N}}, \tag{3.11}$$

Therefore, the extended manifold vector, that is common to each one of the $\mathcal{D}$ subframes, $\underline{h}_k \triangleq \underline{h}(\theta_k, \overline{\theta}_k, \mathfrak{f}_k) \in \mathcal{C}^{N\mathcal{N}_s \times 1}$ in Equation 3.8 can be written as

$$\begin{aligned} \underline{h}_k &= \mathbb{T}\left(\mathfrak{f}_k\right) \underline{S}_{\mathrm{v}}\left(\theta_k, \overline{\theta}_k\right) \\ &= \mathrm{diag}\left(\underline{\mathcal{F}}\left(\mathfrak{f}_k\right)\right) \mathbb{A}^T \underline{\overline{S}}^*\left(\overline{\theta}_k\right) \otimes \underline{S}\left(\theta_k\right). \end{aligned} \tag{3.12}$$

Then, by repeating the above data re-arrangement for all the available $\mathcal{D}$ subframes, the overall received data matrix can be obtained and written as

$$\begin{aligned} \mathbb{X} &\triangleq [\mathbb{X}_1, \mathbb{X}_2, \ldots, \mathbb{X}_\ell, \ldots, \mathbb{X}_\mathcal{D}] \in \mathcal{C}^{N\mathcal{N}_s \times L\mathcal{D}} \\ &= \sum_{k=1}^{K} \beta_k \underline{h}_k \underline{F}_k^T + \mathbb{N}, \end{aligned} \tag{3.13}$$

where

$$\begin{aligned}\underline{F}_k &\triangleq \underline{F}(\mathfrak{f}_k, l_k) \in \mathcal{C}^{L\mathcal{D}\times 1}\\ &= \begin{bmatrix} 1 \\ \exp(j2\pi\mathfrak{f}_k\mathcal{N}_s LT_c) \\ \vdots \\ \exp(j2\pi\mathfrak{f}_k(\mathcal{D}-1)\mathcal{N}_s LT_c) \end{bmatrix} \otimes \left(\mathbb{J}^{l_k}\underline{\mathfrak{c}}\right)\end{aligned} \tag{3.14}$$

represents the k-th target's Doppler-delay response vector. Moreover, the noise matrix $\mathbb{N}$ is defined as

$$\mathbb{N} \triangleq [\mathbb{N}_1, \mathbb{N}_2, \ldots, \mathbb{N}_\ell, \ldots, \mathbb{N}_\mathcal{D}] \in \mathcal{C}^{N\mathcal{N}_s\times L\mathcal{D}}. \tag{3.15}$$

Note that the signal model in Equation 3.13 can be written in a compact matrix format as follows:

$$\mathbb{X} = \mathbb{H}\,\mathrm{diag}(\underline{\beta})\mathbb{F}^T + \mathbb{N} \in \mathcal{C}^{N\mathcal{N}_s\times L\mathcal{D}}, \tag{3.16}$$

where

$$\begin{aligned}\mathbb{H} &\triangleq \left[\underline{h}\left(\theta_1, \overline{\theta}_1, \mathfrak{f}_1\right), \underline{h}\left(\theta_2, \overline{\theta}_2, \mathfrak{f}_2\right), \ldots, \underline{h}\left(\theta_K, \overline{\theta}_K, \mathfrak{f}_K\right)\right],\\ \mathbb{F} &\triangleq \left[\underline{F}(\mathfrak{f}_1, l_1), \underline{F}(\mathfrak{f}_2, l_2), \ldots, \underline{F}(\mathfrak{f}_K, l_K)\right],\\ \underline{\beta} &\triangleq [\beta_1, \beta_2, \ldots, \beta_K]^T.\end{aligned}$$

3.4 Parameter Estimation

Based on the signal modelled by Equation 3.16, subspace-based methods are proposed in this section to estimate the delay l_k, Doppler frequency $\mathfrak{f}_k$, DOA θ_k, DOD $\overline{\theta}_k$ and the complex path coefficient β_k for the k-th target, $\forall k$.

3.4.1 Joint Doppler and Delay Estimation

First, consider the transpose of the data matrix in Equation 3.16, i.e.

$$\mathbb{X}^T = \mathbb{F}\,\mathrm{diag}\left(\underline{\beta}\right)\mathbb{H}^T + \mathbb{N}^T \in \mathcal{C}^{L\mathcal{D}\times N\mathcal{N}_s}, \tag{3.17}$$

it can be seen that the targets lie in a subspace spanned by columns of the matrix $\mathbb{F}$. Therefore, the delay and Doppler frequency for all the K targets can be estimated by searching for the peaks of the following 2-dimensional cost function

$$\xi_{\text{DOP-DELAY}}(\mathfrak{f}, l) = \frac{\underline{F}(\mathfrak{f}, l)^H \underline{F}(\mathfrak{f}, l)}{\underline{F}(\mathfrak{f}, l)^H \mathbb{P}_{\mathbb{E}_n} \underline{F}(\mathfrak{f}, l)}, \tag{3.18}$$

where $\underline{F}(\mathfrak{f}, l)$ is the target's Doppler-delay response vector given in Equation 3.14 and $\mathbb{P}_{\mathbb{E}_n}$ is the projection operator onto the subspace spanned by columns of noise eigenvectors $\mathbb{E}_n$ of the following covariance matrix

$$\mathbb{R} = \frac{1}{N\mathcal{N}_s}\mathbb{X}^T\mathbb{X}^* \tag{3.19}$$

That is,

$$\mathbb{P}_{\mathbb{E}_n} = \mathbb{E}_n(\mathbb{E}_n^H\mathbb{E}_n)^{-1}\mathbb{E}_n^H \tag{3.20}$$

3.4.2 Joint DOA and DOD Estimation

Next, in order to estimate the DOA and DOD of the k-th target, the interfering echoes from the other $K-1$ targets should be removed from the received data matrix $\mathbb{X}$ in Equation 3.16. Based on the delay and Doppler frequency estimates obtained in Section 3.4.1 for the other $K-1$ targets, the following matrix can be constructed

$$\mathbb{F}_k = \left[\underline{F}_1, \underline{F}_2, \ldots, \underline{F}_{k-1}, \underline{F}_{k+1}, \ldots, \underline{F}_K\right], \tag{3.21}$$

where the Doppler-delay response vector of the k-th target $\underline{F}_k$ has been excluded. Then, by applying the following projection operator

$$\mathbb{P}^{\perp}_{\mathbb{F}_k} = \mathbb{I}_{L\mathcal{D}} - \mathbb{F}_k(\mathbb{F}_k^H\mathbb{F}_k)^{-1}\mathbb{F}_k^H \tag{3.22}$$

onto $\mathbb{X}^T$ in Equation 3.17, i.e. $\mathbb{P}^{\perp}_{\mathbb{F}_k}\mathbb{X}^T$, the contribution from the other $K-1$ targets having different delays and/or Doppler frequencies can be removed from $\mathbb{X}^T$. Therefore, based on the data matrix $\mathbb{X}$ modelled by Equation 3.16 with interferences from other targets removed, i.e. $\mathbb{X}\mathbb{P}^{\perp T}_{\mathbb{F}_k}$, the following covariance matrix can be calculated

$$\mathbb{R}_k = \frac{1}{L\mathcal{D}} \mathbb{X}\mathbb{P}^{\perp *}_{\mathbb{F}_k}\mathbb{X}^H, \tag{3.23}$$

and the DOA and DOD of the k-th target are indicated by the peak of the following 2-dimensional cost function

$$\xi_{\text{DOA}-\text{DOD},k}\left(\theta,\overline{\theta}\right) = \left.\frac{\underline{h}(\theta,\overline{\theta},\mathfrak{f})^H \underline{h}\left(\theta,\overline{\theta},\mathfrak{f}\right)}{\underline{h}(\theta,\overline{\theta},\mathfrak{f})^H \mathbb{P}_{\mathbb{E}_{n,k}} \underline{h}\left(\theta,\overline{\theta},\mathfrak{f}\right)}\right|_{\mathfrak{f}=\mathfrak{f}_k}, \tag{3.24}$$

where $\underline{h}\left(\theta,\overline{\theta},\mathfrak{f}\right)$, given $\mathfrak{f}=\mathfrak{f}_k$, is the extended array manifold vector (i.e. transformed virtual array manifold vector) given by Equation 3.12 and $\mathbb{P}_{\mathbb{E}_{n,k}}$ is the projection operator onto the subspace spanned by columns of noise eigenvectors $\mathbb{E}_{n,k}$ of the covariance matrix $\mathbb{R}_k$ (see Equation 3.23), i.e.

$$\mathbb{P}_{\mathbb{E}_{n,k}} = \mathbb{E}_{n,k}(\mathbb{E}^H_{n,k}\mathbb{E}_{n,k})^{-1}\mathbb{E}^H_{n,k} \tag{3.25}$$

It is important to note that the proposed parameter estimation algorithm automatically associates the estimated Doppler frequency, delay, DOA and DOD to the same target.

3.4.3 Complex Path Coefficient Estimation

With reference to Equation 3.16, based on the previously estimated DOA, DOD, Doppler frequency and delay, the targets' complex path coefficients can be estimated as

$$\underline{\beta} = \underline{\text{diag}}\left(\mathbb{H}^{\#}\mathbb{X}\left(\mathbb{F}^T\right)^{\#}\right), \tag{3.26}$$

where $\#$ represents pseudo-inverse, the matrices $\mathbb{F}$ and $\mathbb{H}$ are constructed using the parameters estimated in Sections 3.4.1 and 3.4.2, respectively.

3.5 Computer Simulation Studies

In this section, computer simulation studies are provided to demonstrate the performance of the proposed multi-target parameter estimation algorithms using a bistatic MIMO radar. The radar operates in the presence of $K = 12$ targets, whose parameters are given in Table 3.1 and Figure 3.2 below.

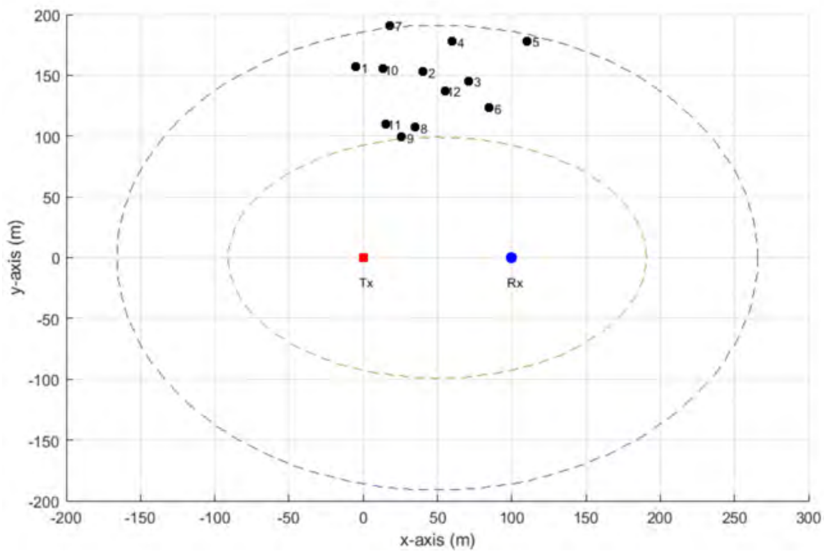

Figure 3.2: Bistatic MIMO radar and targets' location.

Without loss of generality, both the Tx and Rx arrays are uniform circular arrays (UCAs) with $\overline{N} = N = 8$ antenna element and reference points set at the array centroids, as shown in Figure 3.3 below. The figure shows the Tx and Rx arrays relative to their own local reference points; thus, the bistatic distance between the Tx and Rx arrays is not depicted.

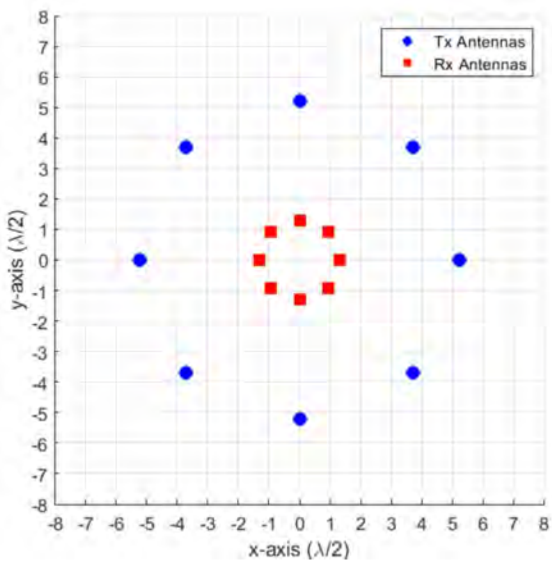

Figure 3.3: Bistatic MIMO radar Tx and Rx antenna arrays.

Table 3.1: Targets' environment

Target Index	Delay (T_c)	DOA (deg)	DOD (deg)	Doppler (Hz)	Complex Path Coefficient
1	21	124	92	-493	$1.33\angle-44.5°$
2	17	111	75	-362	$0.41\angle-37.9°$
3	15	101	64	-552	$0.54\angle30.6°$
4	25	103	71	-407	$0.70\angle14.1°$
5	28	87	58	-600	$0.96\angle61.1°$
6	9	97	55	-494	$1.09\angle-43.9°$
7	30	113	85	-628	$1.19\angle35.4°$
8	3	121	72	-580	$1.18\angle151.6°$
9	1	127	75	-291	$0.92\angle-15.2°$
10	19	119	85	-719	$0.49\angle-168.1°$
11	5	128	82	-407	$1.65\angle-111.0°$
12	12	108	68	-447	$1.10\angle113.6°$

Table 3.2: Bistatic MIMO radar system specifications

Parameter	Notation	Value
Transmit vector symbol	$\underline{a}[n], \forall n$	Hadamard codes
Carrier frequency	F_c	10 GHz (X-band)
Chip duration	T_c	20 ns
Pulse Repetition Interval (PRI)	LT_c	10 μs
Range resolution		3 m
Baseline distance		100 m
Wave propagation speed	c	3×10^8 m/s

The pulse compression code uses an m-sequence of length $\mathcal{N}_c = 31$ described by the primitive polynomials D^5+D+1 in Galois field 2. The transmit vector symbols $\underline{a}[n], \forall n$ are Hadamard codes with period $\mathcal{N}_s = 64$. Others adopted simulation parameters are summarised in Table 3.2.

The number of transmit subframes is $\mathcal{D} = 10$, that is 10 full periods of the employed Hadamard codes and in total $\mathcal{D}\mathcal{N}_s = 640$ vector symbols. For 20 dB Signal-to-Noise Ratio (SNR), Figures 3.4 and 3.5 present the 2D contour and surface diagrams for joint Doppler and delay estimation and joint DOA and DOD estimation, respectively. Finally, the targets' complex path coefficients can be obtained using Equation 3.26 and estimated values are shown in Figure 3.6.

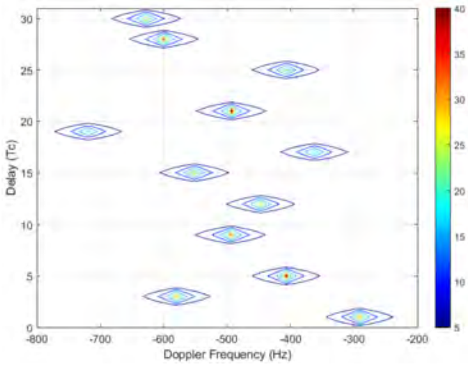

(a) Contour plot.

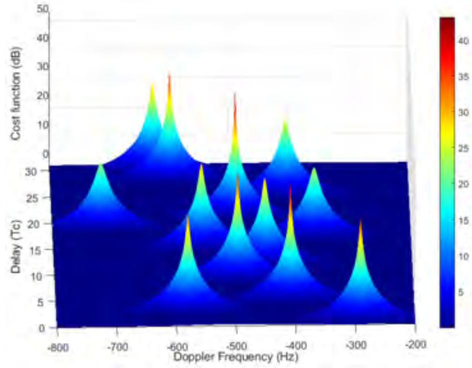

(b) Surface plot.

Figure 3.4: Joint delay and Doppler frequency estimation with SNR = 20 dB and UCA of Figure 3.3.

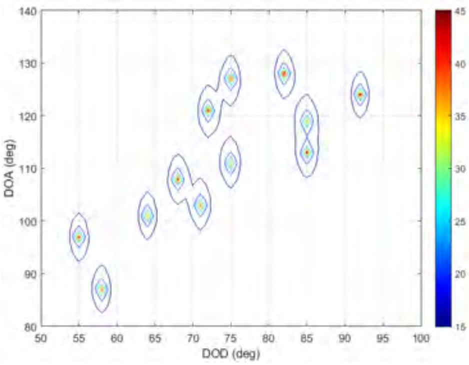

(a) Contour plot.

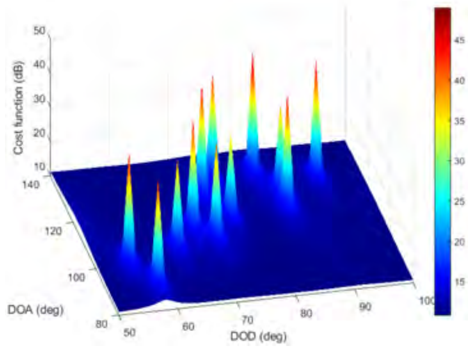

(b) Surface plot.

Figure 3.5: Joint DOA and DOD estimation with SNR = 20 dB and UCA of Figure 3.3.

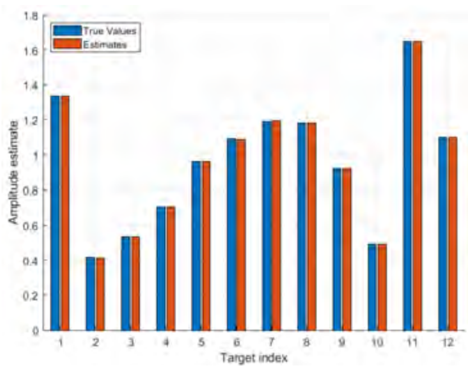

(a) Magnitude

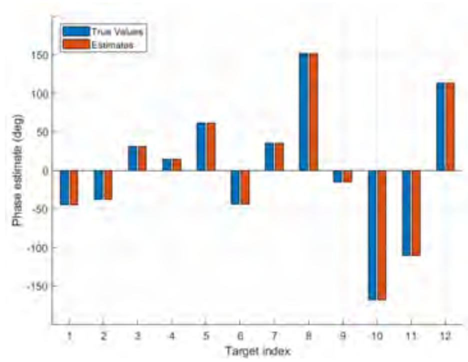

(b) Phase

Figure 3.6: Path gain estimation with SNR = 20 dB and UCA of Figure 3.3.

It is important to note that Figure 3.5 presents the sum of the cost functions in Equation 3.24 for all the 12 targets. In fact, for each target, there is only one sharp peak appear on the spectrum of the cost function $\xi_{\text{DOA}-\text{DOD},k}\left(\theta,\overline{\theta},\mathfrak{f}_k\right)$ indicating its DOA and DOD. Therefore, the association problem between the estimated Doppler-delay and DOA-DOD is avoided.

3.5.1 Second Simulation

The performance of the algorithms discussed above was also evaluated using the uniform linear antenna array (ULA) depicted in Figure 2.9 (Chapter 2). This configuration utilises a transmitter array with $\overline{N}' = 12$ elements and a receiver array with $N' = 24$ elements. However, combiners are employed at the receiver to generate $N = 12$ receiver streams. Initial simulations with the ULA failed to detect the 5^{th} target at 20 dB SNR. Even increasing the SNR to 30 dB did not yield successful estimation of the 5th target's direction (see Figures 3.7, 3.8, and 3.9 for details).

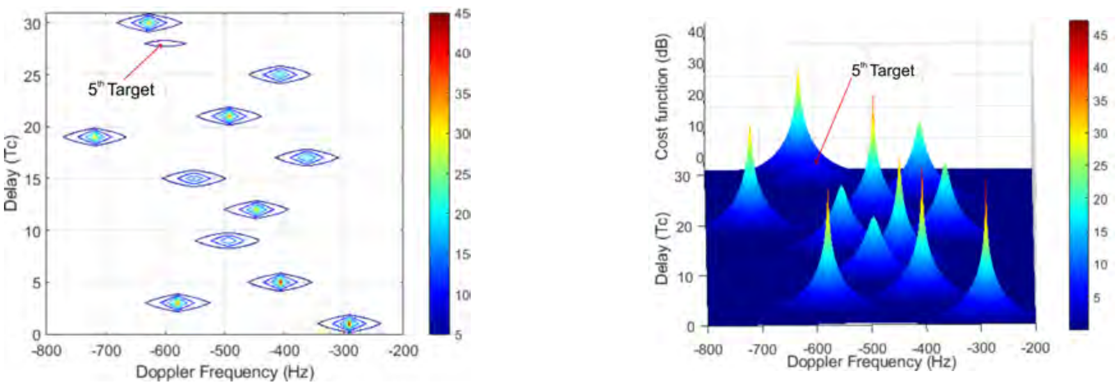

(a) Contour plot. (b) Surface plot.

Figure 3.7: Joint delay and Doppler frequency estimation with SNR = 30 dB and ULA of Figure 2.9.

These simulations highlight a crucial aspect: despite having more antenna elements and streams, the ULA exhibited poor performance for target detection in certain directions. This observation aligns with the inherent omnidirectional gain pattern of UCAs, suggesting their suitability for scenarios where uniform performance across all directions is desired. Consequently, the ULA will be excluded from further comparisons using Monte Carlo simulations in the next section.

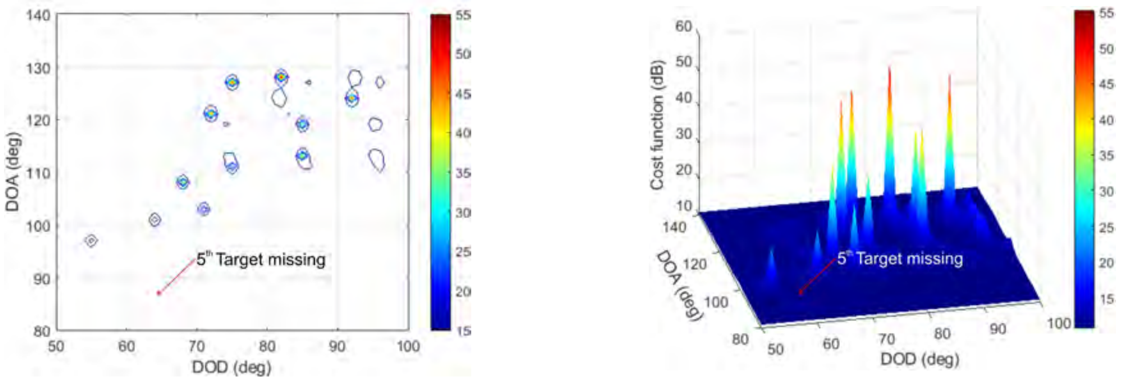

(a) Contour plot. (b) Surface plot.

Figure 3.8: Joint DOA and DOD estimation with SNR = 30 dB and ULA of Figure 2.9.

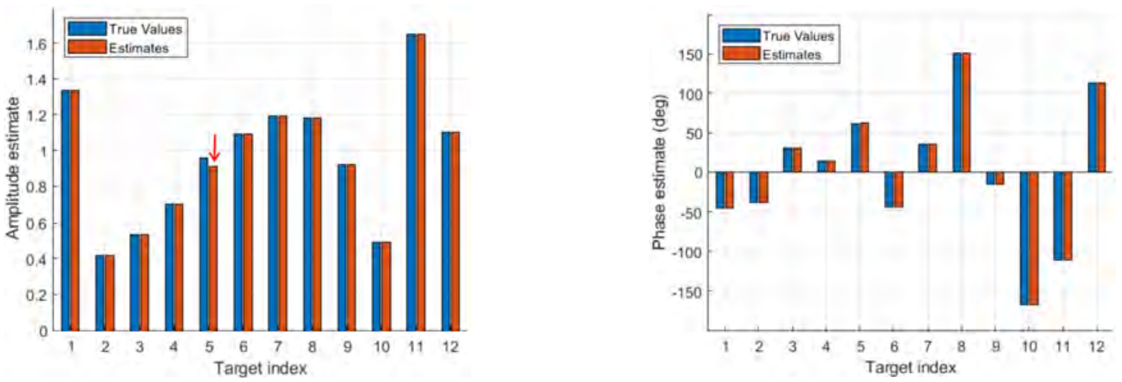

(a) Magnitude (b) Phase

Figure 3.9: Path gain estimation with SNR = 30 dB and ULA of Figure 2.9.

3.5.2 Monte-Carlo simulation

Consider the target environment specified in Table 3.3, the Monte-Carlo simulation has been carried out to evaluate the performance of the proposed algorithm based on the RMSE criterion defined as follows:

$$\mathrm{RMSE}_p = \frac{1}{K}\sum_{k=1}^{K}\sqrt{\frac{1}{I}\sum_{i=1}^{I}\{|\widehat{p}_k - p_{k,i}|^2\}}, \tag{3.27}$$

here, $p_{k,i}$ represents the general parameter of interest for the k-th target and i-th iteration, while $\widehat{p}_k$ is the corresponding estimate. The number of Monte-Carlo trials, I, is 200. Figures 3.10, 3.11 and 3.12 present the Doppler frequency, DOA & DOD and complex path coefficient RMSE curves as a function of SNR, respectively. It can be clearly observed that with the use of the pulse compression code (m-sequence), the parameter estimation accuracy can be significantly improved.

Table 3.3: Targets' environment for Monte-Carlo simulations

Target Index	Delay (T_c)	DOA (deg)	DOD (deg)	Doppler (Hz)	Complex Path Coefficient
1	21	86	55	-520	$0.75\angle 57.0°$
2	17	96	60	-428	$0.77\angle 170.3°$
3	15	120	83	-474	$0.64\angle 65.6°$

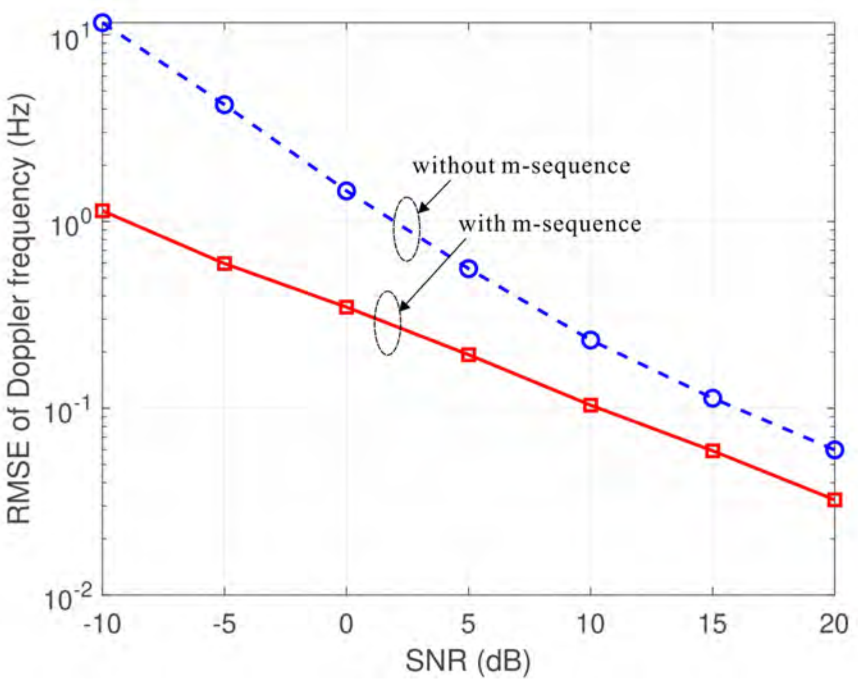

Figure 3.10: RMSE of Doppler frequency estimation versus SNR.

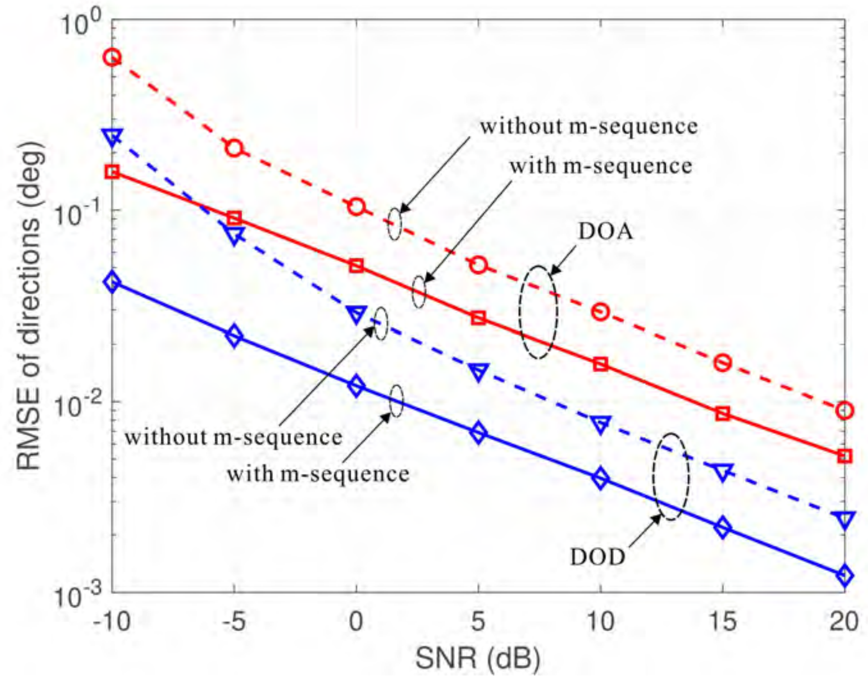

Figure 3.11: RMSE of DOA and DOD estimation versus SNR.

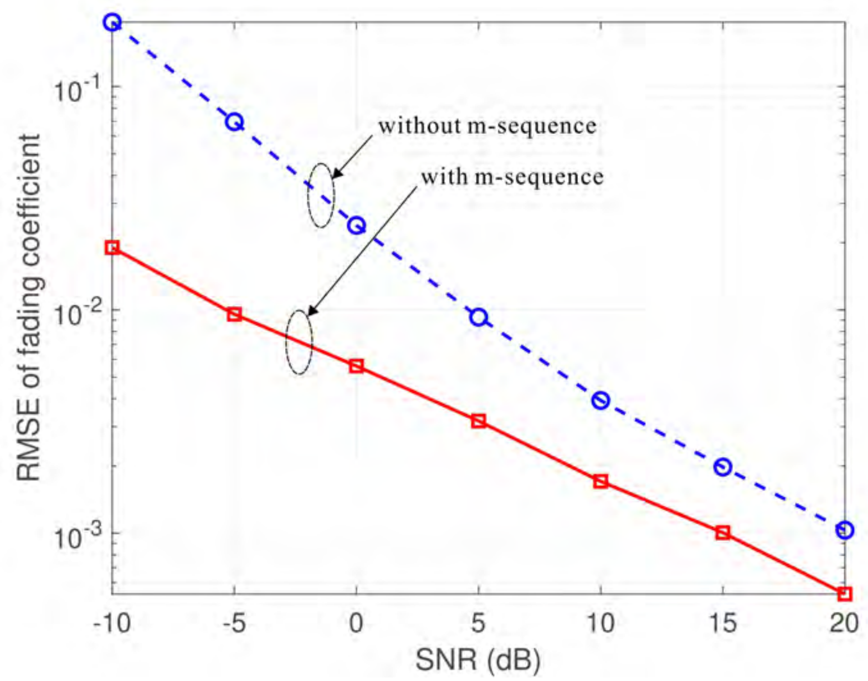

Figure 3.12: RMSE of path coefficient estimation versus SNR.

3.6 Summary

This chapter investigated the multi-target parameter estimation problem in bistatic pulse MIMO radar based on parametric modelling of the radar received signal. Subspace-based super-resolution algorithms are proposed in conjunction with a novel array "manifold extender" to estimate the delay/range, Doppler frequency, DOA, DOD and complex path coefficient of multiple targets. Most importantly, the proposed approach does not suffer from multiple parameter estimates association problem.

3.7 Appendices

Appendix 3.A

The following identities are used in this chapter to derive the expressions (mathematical models) for the data matrix $\mathbb{X}[n]$:

$$\underline{a}^H \underline{b} = \left(\underline{a}^* \odot \underline{b}\right)^T \underline{1}, \tag{3.28}$$

$$\text{vec}\left(\mathbb{ABC}\right) = \left(\mathbb{C}^T \otimes \mathbb{A}\right) \text{vec}\left(\mathbb{B}\right), \tag{3.29}$$

$$\left(\underline{a} \odot \underline{b}\right) \otimes \left(\underline{c} \odot \underline{d}\right) = \left(\underline{a} \otimes \underline{c}\right) \odot \left(\underline{b} \otimes \underline{d}\right), \tag{3.30}$$

$$\left(\mathbb{A} \otimes \mathbb{B}\right)\left(\mathbb{C} \otimes \mathbb{D}\right) = \left(\mathbb{AC}\right) \otimes \left(\mathbb{BD}\right), \tag{3.31}$$

Using the above identities, the data matrix $\mathbb{X}[n]$ as in Equation 3.2 can be re-expressed as follows:

$$\begin{aligned}
\mathbb{X}[n] &= \sum_{k=1}^{K} \beta_k \exp\left(j2\pi \mathfrak{f}_k (n-1) L T_c\right) \mathbb{I}_N \underline{S}_k \left(\overline{\underline{S}}_k^* \odot \underline{a}[n]\right)^T \underline{1}_{\overline{N}} \left(\mathbb{J}^{l_k} \underline{\mathfrak{c}}\right)^T + \mathbb{N}[n] \\
&= \sum_{k=1}^{K} \beta_k \exp\left(j2\pi \mathfrak{f}_k (n-1) L T_c\right) \text{vec}\left(\mathbb{I}_N \underline{S}_k \left(\overline{\underline{S}}_k^* \odot \underline{a}[n]\right)^T \underline{1}_{\overline{N}}\right) \left(\mathbb{J}^{l_k} \underline{\mathfrak{c}}\right)^T + \mathbb{N}[n] \\
&= \sum_{k=1}^{K} \beta_k \exp\left(j2\pi \mathfrak{f}_k (n-1) L T_c\right) \left(\underline{1}_{\overline{N}}^T \otimes \mathbb{I}_N\right) \text{vec}\left(\underline{S}_k \left(\overline{\underline{S}}_k^* \odot \underline{a}[n]\right)^T\right) \left(\mathbb{J}^{l_k} \underline{\mathfrak{c}}\right)^T + \mathbb{N}[n] \\
&= \sum_{k=1}^{K} \beta_k \exp\left(j2\pi \mathfrak{f}_k (n-1) L T_c\right) \left(\underline{1}_{\overline{N}}^T \otimes \mathbb{I}_N\right) \left(\left(\overline{\underline{S}}_k^* \odot \underline{a}[n]\right) \otimes \left(\underline{S}_k \odot \underline{1}_N\right)\right) \left(\mathbb{J}^{l_k} \underline{\mathfrak{c}}\right)^T + \mathbb{N}[n] \\
&= \sum_{k=1}^{K} \beta_k \exp(j2\pi \mathfrak{f}_k (n-1) L T_c) \left(\underline{1}_{\overline{N}}^T \otimes \mathbb{I}_N\right) \left(\left(\underbrace{\overline{\underline{S}}_k^* \otimes \underline{S}_k}_{=\underline{S}_{\mathrm{v},k}}\right) \odot \left(\underline{a}[n] \otimes \underline{1}_N\right)\right) \left(\mathbb{J}^{l_k} \underline{\mathfrak{c}}\right)^T + \mathbb{N}[n]
\end{aligned} \tag{3.32}$$

and this could be further simplified as follows:

$$\begin{aligned}
&= \sum_{k=1}^{K} \beta_k \exp\left(j2\pi \mathfrak{f}_k (n-1) L T_c\right) \left(\underline{1}_{\overline{N}}^T \otimes \mathbb{I}_N\right) \left(\text{diag}\left(\underline{a}[n]\right) \otimes \mathbb{I}_N\right) \underline{S}_{\mathrm{v},k} \left(\mathbb{J}^{l_k} \underline{\mathfrak{c}}\right)^T + \mathbb{N}[n] \\
&= \sum_{k=1}^{K} \beta_k \exp\left(j2\pi \mathfrak{f}_k (n-1) L T_c\right) \left(\underline{a}^T[n] \otimes \mathbb{I}_N\right) \underline{S}_{\mathrm{v},k} \left(\mathbb{J}^{l_k} \underline{\mathfrak{c}}\right)^T + \mathbb{N}[n].
\end{aligned} \tag{3.33}$$

Chapter 4

Bistatic MIMO Radar: Localisation Using Tx Fast Time Codes

This chapter investigates bistatic MIMO radar for estimating various multi-target parameters of interest in the presence of clutter and noise, employing fast time codes. The parameters of interest include DOD, DOA, range and velocity and a novel algorithm is proposed for estimating these target parameters based on the concepts of the "array manifold" and "manifold extenders". The performance of the proposed algorithm is evaluated using Monte Carlo simulation studies.

4.1 Introduction

Modern radars operate in the presence of objects/targets, clutter, noise, and interferences [2]. The main objectives of a radar are to detect the presence of targets and estimate their parameters, especially when targets are located close together in space. Once the presence of a target is detected in the clutter, then the aims are:

- to accurately estimate various target parameters, such as range, direction and velocity, and

- to solve the targets' "classification" problem, i.e. identify the type of target by getting its "electronics signature".

The simplest radar architecture is the “monostatic” [91] where the Tx and Rx antennas are “collocated”, and thus the DOD from the radar's Tx to the target is identical to the DOA from the target to the radar's Rx. Some popular examples of DOA estimation for monostatic MIMO radar are the LS, Capon and APES MIMO algorithms [70].

This chapter is concerned with "bistatic" radar where there is some considerable distance between the radar's Tx and Rx. Consequently, the DOA is different from the DOD. Bistatic radars introduce several technical complications, but there are many significant advantages relative to monostatic radar architectures. For instance, bistatic radar can handle stealthy targets, while “jamming” is very difficult. The most powerful and modern monostatic/bistatic radar is the MIMO radar, which employs antenna arrays of known geometries at both the Tx and Rx sides. As the title of the chapter suggests, this work is concerned with bistatic MIMO radar, with emphasis given to DOA and DOD estimation. Existing DOA-DOD estimation algorithms in bistatic MIMO radar have been reported in [92–95].

In [92], a joint DOA and DOD estimation algorithm is proposed for bistatic MIMO radar based on a polynomial root-finding subspace method. The main drawback of [92] is that the proposed algorithm is restricted to bistatic MIMO, where both Tx and Rx arrays are uniform linear arrays.

In [93], a two-dimensional DOA and DOD estimation is proposed based on PARAFAC analysis instead of Eigenvector decomposition. The paper claims the computational efficiency using tensor processing, but no computational complexity comparison with any conventional method is presented.

In [94], a DOA-DOD and Range estimation is presented for Frequency Diverse Array FDA-MIMO radar. This is a specific form of MIMO radar which suffers from the "ambiguity problem" where a single target appears to have many ranges and many DOD. Thus, [94] is mainly focused on resolving the ambiguity problem, while it also assumes ULA for both Tx and Rx arrays.

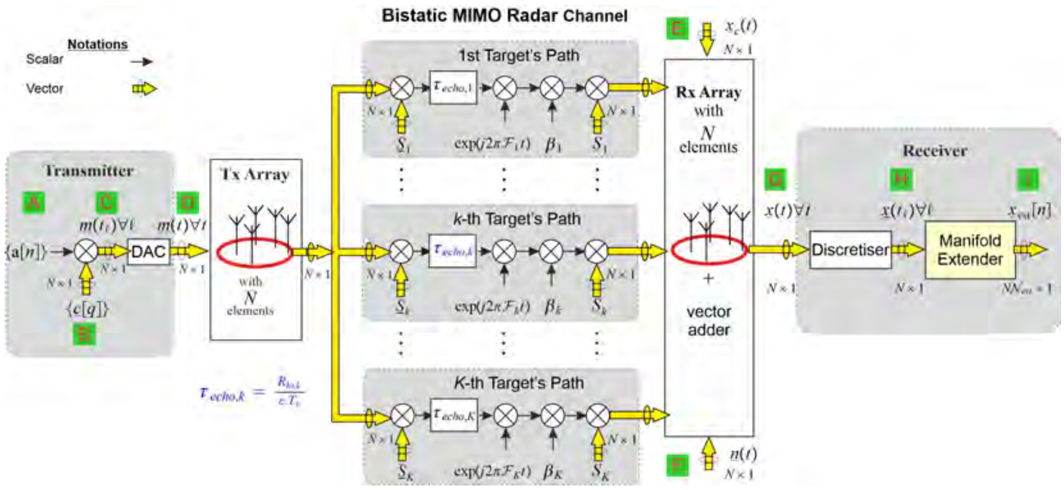

Figure 4.1: Multi-target MIMO radar

In [95], the time synchronisation is proposed between the Tx and Rx sites. First, it estimates the bistatic range through matched filtering and non-linear least squares (NLS) optimisation. Then the DOA and DOD are calculated using the known bistatic geometry i.e., the bistatic baseline, Tx, and Rx array locations. Finally, the synchronisation offset is calculated through the estimated/calculated parameters' variance. This calculation is only possible in the presence of a single target, and the system requires a high SNR to operate reasonably.

As stated before, in this chapter DOA and DOD are the primary parameters to be estimated based on the concept of "extended manifolds" which are functions of the array manifold. For plane-wave propagation, the array manifold is a vector function of the target direction, array geometry and carrier frequency. Array manifolds (or simply manifolds) are mathematical objects such as "curves", "surfaces" etc. (i.e., non-linear subspaces). These manifolds have been analysed in [60] and their shapes and parameters are directly connected to the accuracy, resolution, and detection capabilities of the array.

These days more radar system and target parameters may be added to the array manifold beyond the array geometry, the target direction and the carrier frequency. To distinguish them from standard "spatial" array manifolds, manifolds incorporating additional parameters of interest are termed extended manifolds [78]. Such additional parameters may be polarisation, Doppler, delay, PN-codes, and multi-carriers, etc. Every time a new system parameter is added, instead of having a complex analysis like the one presented in [60], the aim is to express the extended manifold vector as a function of the spatial manifold vector and make a direct connection to the properties and capabilities between the new manifold and the original spatial manifold.

In this chapter, the "manifold extender" will be used by starting with the Rx spatial array manifold and then forming the Rx's extended manifold by adding the following three new but unknown parameters:

- the target's range-bin,
- Doppler frequency (for moving targets),
- The DOD from the Tx to the target.

This chapter builds on the DOA and DOD estimation proposed in [96] for a MIMO communication system. It explores the virtual array concept (a form of extended array manifold [78,79]) to extend the system's observation space from N (number of Rx antennas) to $N\overline{N}$ (i.e. the product of Rx antennas N and the Tx antennas $\overline{N}$), hence enabling to detect and process more targets than Rx antenna elements with greater resolution capabilities[1].

In summary, this chapter builds upon the ideas put forth in previous works, including those by [31, 78, 79, 96, 97], and extends the concept to Multi-target Bistatic MIMO radar. The chapter is structured as follows: In Section 2, the generation of the Tx baseband signal of the proposed system is presented. In Section 3, the MIMO multi-target channel model that will be used in this chapter is discussed. Section 4 is concerned with the modelling of the received array vector signal. Section 5 focuses on the proposed parameter estimation algorithms, while Section 6 details the computer simulation environments and results. The chapter is concluded in Section 7.

[1]The concept of the extended array manifold has been also used in [31] for monostatic MIMO radar and showed that the extended array manifold algorithms outperformed the conventional algorithms/processing with respect to RMSE criterion.

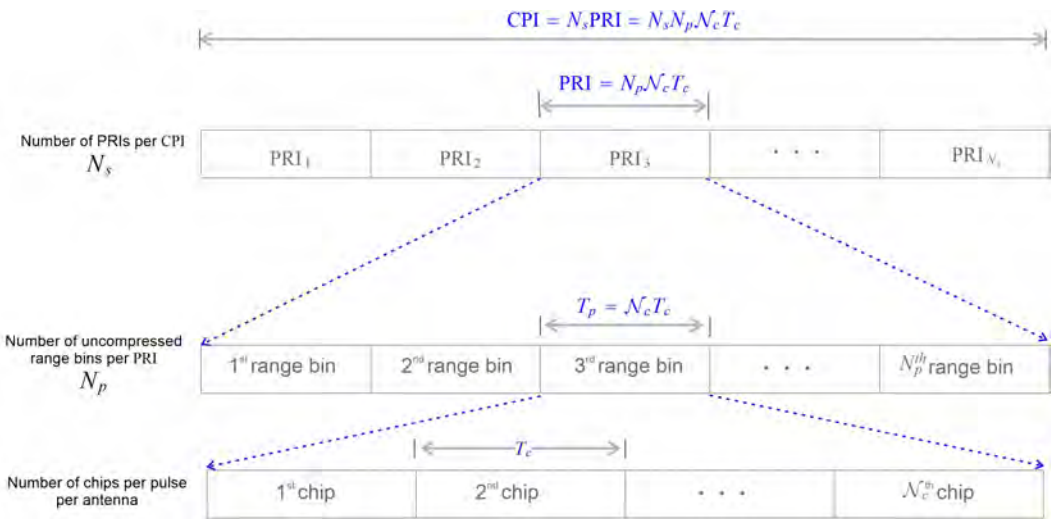

Figure 4.2: Baseband Tx signal generation

4.2 Tx Signal Modelling

Figure 4.1 conceptually illustrates a bistatic MIMO radar architecture, with the yellow arrow representing vectors of parallel signals. At Point-A of the transmitter (Tx), a sequence of N_s symbols $\{a[n] \in \pm 1, \forall n = 1, 2, \ldots N_s\}$ is used with pulse duration T_p. The Tx uses an antenna array of $\overline{N}$ antennas and the sequence $\{a[n] \in \pm 1\}$ is copied to all the $\overline{N}$ RF units. Then, this sequence is spread over a larger bandwidth by utilizing a vector of $\overline{N}$ PN-codes (one PN-code per Tx-antenna), also known as FTC as shown at Point-B. All these PN-codes have length $\mathcal{N}_c$ and chip period T_c with

$$\mathcal{N}_c T_c = T_p \tag{4.1}$$

The radar's PRI is assumed having N_p uncompressed range bins or, equivalently, $N_p \mathcal{N}_c$ compressed range bins. That is

$$\begin{aligned} \text{PRI} &= N_p T_p &(4.2)\\ &= N_p \mathcal{N}_c T_c &(4.3) \end{aligned}$$

Figure 4.2 illustrates the above time frame structure of the radar, considering also that the coherent processing interval over which the radar will estimate the various target parameters has a duration equal to N_sPRI. That is:

$$\begin{aligned} \text{CPI} &= N_s\text{PRI} = N_s N_p \mathcal{N}_c T_c &(4.4)\\ &= N_s N_p \mathcal{N}_c T_c &(4.5)\end{aligned}$$

The number of data symbols generated at Point-C of Figure 4.1 over one CPI can be modelled by the following matrix $\mathbb{M}$:

$$\begin{aligned} \mathbb{M} &\triangleq \begin{bmatrix} \underline{m}_1, & \underline{m}_2, & \ldots, & \underline{m}_{N_s N_p \mathcal{N}_c} \end{bmatrix} &(4.6)\\ &= \underline{\mathrm{a}}^T \otimes \underbrace{\begin{bmatrix} \mathbb{C}, & \mathbb{O}_{\overline{N}\times(N_p\mathcal{N}_c-\mathcal{N}_c)} \end{bmatrix}}_{\triangleq \mathbb{C}_{ex}^T \in \mathcal{R}^{\overline{N}\times N_p\mathcal{N}_c}} \in \mathcal{R}^{\overline{N}\times N_s N_p \mathcal{N}_c} &(4.7)\end{aligned}$$

where the data symbols vector $\underline{\mathrm{a}}$ is defined as

$$\underline{\mathrm{a}} \triangleq \begin{bmatrix} \mathrm{a}[1], & \mathrm{a}[2], & \ldots, & \mathrm{a}[N_s] \end{bmatrix}^T \in \mathcal{R}^{N_s\times 1} \tag{4.8}$$

and the PN-codes matrix has been extended with zeros until the end of each PRI, i.e. $N_p\mathcal{N}_c - \mathcal{N}_c$ columns of $\overline{N}$ zeros

$$\mathbb{C}_{ex}^T = \begin{bmatrix} \underline{c}[1], & \underline{c}[2], & \ldots, & \underline{c}[q], & \ldots, & \underline{c}[N_p\mathcal{N}_c] \end{bmatrix} \in \mathcal{R}^{\overline{N}\times N_p\mathcal{N}_c} \tag{4.9a}$$

$$= \left[\begin{array}{c} \underbrace{\begin{matrix} \alpha_1[1], & \alpha_1[2], & \cdots & \alpha_1[\mathcal{N}_c], \\ \alpha_2[1], & \alpha_2[2], & \cdots & \alpha_2[\mathcal{N}_c], \\ \vdots & \vdots & & \vdots \\ \alpha_{\overline{N}}[1], & \alpha_{\overline{N}}[2], & \cdots & \alpha_{\overline{N}}[\mathcal{N}_c], \end{matrix}}_{\triangleq \mathbb{C}^T} \underbrace{\begin{matrix} 0, & 0, & \cdots & 0 \\ 0, & 0, & \cdots & 0 \\ \vdots & \vdots & & \vdots \\ 0, & 0, & \cdots & 0 \end{matrix}}_{\substack{N_p\mathcal{N}_c - \mathcal{N}_c \\ \text{columns of } \overline{N} \text{ zeros}}} \end{array}\right] \tag{4.9b}$$

As shown at Point-B of Figure 4.1, the q-th column of the $\mathbb{C}_{ex}^T$ above matrix is the vector $\underline{c}[q]$. The ℓ-th column[2] of the matrix $\mathbb{M}$ (i.e. $\underline{m}_\ell$) representing the

[2]Note that ℓ is an integer taking values $1, 2, ..., N_s N_p \mathcal{N}_c$.

symbols that appear at Point-C during the chip interval ℓT_c. It is important to point out that the PN-code matrix $\mathbb{C}$ has a covariance matrix approximately equals to an identity matrix (almost orthogonal PN-codes). That is:

$$\mathbb{R}_{\mathbb{CC}} = \frac{1}{\mathcal{N}_c}\mathbb{C}^T\mathbb{C} \approx \mathbb{I}_{\overline{N}} \in \mathcal{R}^{\overline{N}\times\overline{N}} \tag{4.10}$$

Then it is easy to see (using Equation 4.7) that the covariance matrix for the data matrix M is

$$\mathbb{R}_{\mathbb{MM}} = \frac{1}{\mathcal{N}_c\ N_s}\mathbb{M}\mathbb{M}^T \approx \mathbb{I}_{\overline{N}} \in \mathcal{R}^{\overline{N}\times\overline{N}} \tag{4.11}$$

At Point-D in Figure 4.1, after the DAC (digital to analogue converter) block, the analogue baseband transmitted vector signal is represented as follows:

$$\underline{m}(t) = \left[m_1(t),\quad m_2(t),\quad ...,\quad m_{\overline{N}}(t)\right]^T \tag{4.12}$$

4.3 Radar Channel Model

The wireless MIMO channel is modelled as shown in Figure 4.1 between Points-D and G. It considers a bistatic MIMO pulse radar operating in the presence of K moving targets. The geometry of the k-th moving target is shown in Figure 4.3 having velocity v_k at a bistatic range $R_{bi,k}$.

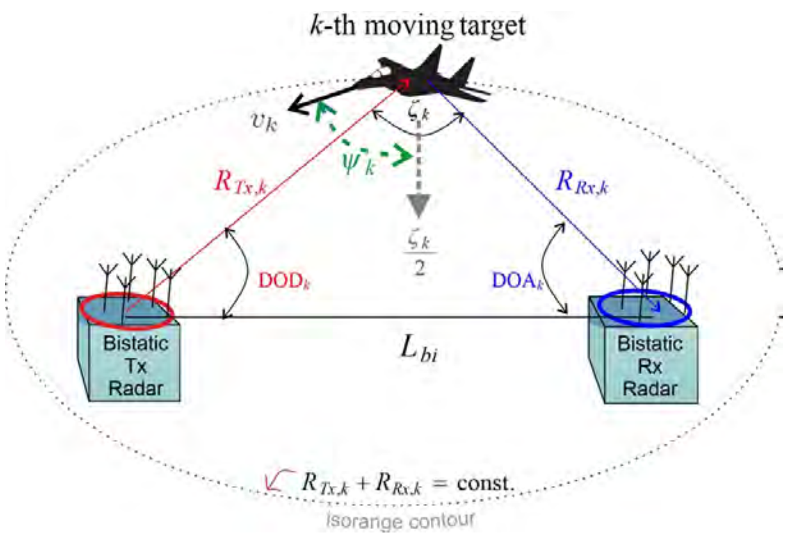

Figure 4.3: Bistatic radar's target

The vector-signal at the output Point-D in Figure 4.1 is transformed by the Tx antenna array to a vector of $\overline{N}$ electromagnetic waves (one per antenna) which will propagate through our 3D physical space. The various "displacements" of these electromagnetic waves at the Tx antennas are a function of

- the Tx-array geometry, and
- their direction of propagation $\left(\overline{\theta}_k, \overline{\phi}_k\right)$, where $\overline{\theta}_k$ represents azimuth and $\overline{\phi}_k$ elevation angles.

These electromagnetic "displacements" for the k-th target's direction $(\overline{\theta}_k, \overline{\phi}_k)$ are modelled by the Tx manifold vector:

$$\begin{aligned} \overline{\underline{S}}_k &\triangleq \overline{\underline{S}}(\overline{\theta}_k, \overline{\phi}_k) \in \mathcal{C}^{\overline{N}\times 1} \\ &= \exp\left(+j\left[\overline{\underline{r}}_x, \quad \overline{\underline{r}}_y, \quad \overline{\underline{r}}_z\right]\underline{k}(\overline{\theta}_k, \overline{\phi}_k)\right) \end{aligned} \tag{4.13}$$

where

$$\left[\overline{\underline{r}}_x, \quad \overline{\underline{r}}_y, \quad \overline{\underline{r}}_z\right] = \text{Tx antenna array geometry} \tag{4.14}$$

$$\underline{k}(\overline{\theta}_k, \overline{\phi}_k) = \frac{2\pi}{\lambda}\underline{u}(\overline{\theta}_k, \overline{\phi}_k) \text{ is wavenumber vector} \tag{4.15}$$

with $\underline{u}(\overline{\theta}_k, \overline{\phi}_k)$ being a unity norm vector pointing towards the direction of departure, i.e.

$$\underline{u}(\overline{\theta}_k, \overline{\phi}_k) = \begin{bmatrix} \cos\overline{\theta}_k \cos\overline{\phi}_k \\ \sin\overline{\theta}_k \cos\overline{\phi}_k \\ \sin\overline{\phi}_k \end{bmatrix} \tag{4.16}$$

The transmitted electromagnetic waves will be reflected by the k-th target and the echo will be received by the radar's Rx antenna array after a propagation time

$$\tau_{echo,k} = \frac{R_{Tx,k} + R_{Rx,k}}{c}, \forall k, \tag{4.17}$$

$$d_k = \left\lfloor \frac{\tau_{echo,k}}{T_c} \right\rfloor \tag{4.18}$$

where c is the speed of light. Figure 4.1 shows the delay $\tau_{echo,k}$, the path gain β_k and the effects of the target's Doppler frequency $\mathcal{F}_k$. Note that the parameter β_k in Figure 4.1 is modelled as follows:

$$\beta_k = |\beta_k| \exp(j\angle\beta_k) \tag{4.19}$$

where

$$|\beta_k| = \sqrt{\frac{G_{Tx}G_{Rx}}{(4\pi)^3}} \left(\frac{\lambda}{R_{Tx}R_{Rx}}\right) \sqrt{\mathrm{RCS}_k} \tag{4.20}$$

$$\angle\beta_k = \angle\left(-j2\pi F_c \frac{R_{bi,k}}{c}\right) + \angle(j\psi_k) + \angle(j2\pi\mathcal{F}_k t) \tag{4.21}$$

where F_c is the carrier frequency and ψ_k is random phase. Thus, the parameter β_k of the k-th target is a function of:

- the target's radar cross-section (RCS_k),
- the antenna gains of the Tx and Rx, i.e. G_{Tx} and G_{Rx} respectively,
- the Tx to target range $R_{Tx,k}$ and target to Rx range R_{Rx}.

The channel model also considers targets' movement and resulting Doppler shift on the Tx carrier frequency. In Figure 4.1 the Doppler shift of the k-th moving target is represented by the term $\exp(j2\pi\mathcal{F}_k t)$. For the bistatic geometry of Figure 4.3, this Doppler shift is given as follows [2]:

$$\mathcal{F}_k = \frac{2v_k}{\lambda} \cos\psi_{bi,k} \cos\frac{\zeta_k}{2} \tag{4.22}$$

where the subscript k signifies the k-th target, v_k denotes its velocity, ζ_k is the angle between incident and reflected wave, and $\psi_{bi,k}$ represents the angle between the discontinuous $\frac{\zeta_k}{2}$ and the direction of movement.

Similarly, for the k-th target, the various "displacements" of the electromagnetic waves arriving at the Rx antenna array with direction of arrival θ_k, ϕ_k is modelled by the Rx manifold vector:

$$\underline{S}_k \triangleq \underline{S}(\theta_k, \phi_k) \in \mathcal{C}^{N\times 1} \tag{4.23}$$

$$= \exp\left(-j\left[\underline{r}_x, \quad \underline{r}_y, \quad \underline{r}_z\right] \underline{k}(\theta_k, \phi_k)\right) \tag{4.24}$$

where the matrix $\left[\underline{r}_x, \underline{r}_y, \underline{r}_z\right]^T$ denotes the Cartesian coordinates of the Rx antenna array elements and $\underline{k}(\theta_k, \phi_k)$ is the wavenumber vector corresponding to the Direction of Arrival (DOA).

Based on the above, the impulse response (IR) of a MIMO radar channel can be summarised using the following equation:

$$IR(t) = \sum_{k=1}^{K} \beta_k \exp(j2\pi\mathcal{F}_k t)\underline{S}_k \underline{\overline{S}}_k^H \underline{\delta}(t - \tau_{echo,k}) \tag{4.25}$$

4.4 Radar Receiver based on "Manifold Extender"

At Point-G of Figure 4.1, based on the radar's channel modelling presented in Section III, the analogue received vector-signal $\underline{x}(t) \in \mathcal{C}^{N\times 1}$ at the output of the Rx antenna array can be written as:

$$\underline{x}(t) = \left[x_1(t), \quad x_2(t), \quad ..., \quad x_N(t)\right]^T \in \mathcal{C}^{N\times 1} \tag{4.26}$$

$$= \sum_{k=1}^{K} \underbrace{\sqrt{P_{Tx}}\beta_k \exp(j2\pi\mathcal{F}_k t)\underline{\overline{S}}_k^H \underline{m}(t - \tau_{echo,k})}_{\text{scalar signal (echo) from the } k\text{-th target}} \underline{S}_k + \underline{x}_c(t) + \underline{\mathrm{n}}(t) \tag{4.27}$$

where $\underline{x}_c(t)$ represents the "clutter" effects and $\underline{\mathrm{n}}(t)$ is the complex additive white Gaussian noise (AWGN) of $\mathcal{CN}(\underline{0}, \ \sigma_{\mathrm{n}}^2\mathbb{I}_N)$, i.e. of zero mean and covariance matrix $\mathbb{R}_{\mathrm{nn}} = \sigma_{\mathrm{n}}^2\mathbb{I}_N$. Remember that the subscript k refers to the k-th target, and a bar on top of a symbol represents a Tx parameter.

The analogue vector-signal $\underline{x}(t)$ at Point-G of Figure 4.1 is then digitised to pro-

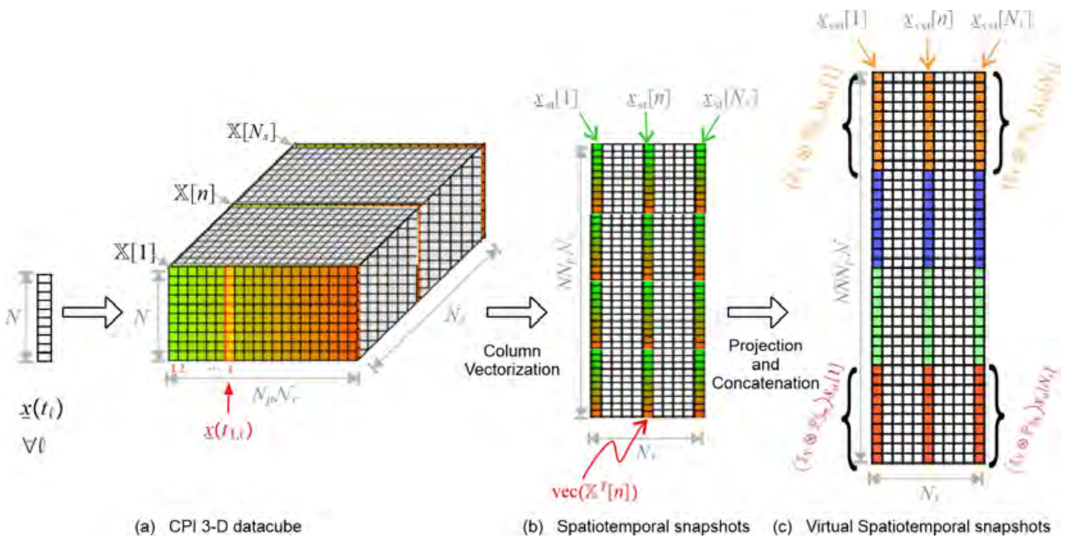

Figure 4.4: MIMO radar Rx 3-D data cube $\mathbb{X}$ for one CPI and extended snapshots formation

duce at Point-H the ℓ-th snapshot vector $\underline{x}(t_\ell), \forall \ell = 1, 2, \ldots$, which is represented as:

$$\underline{x}(t_\ell) = \left[x_1(t_\ell), \quad x_2(t_\ell), \quad \ldots, \quad x_N(t_\ell) \right]^T \in \mathcal{C}^{N\times 1} \tag{4.28}$$

These snapshots, $\forall \ell$, at Point-H are then driven to a suitable "manifold extender" block which is going to be employed by the proposed novel algorithm for estimating both DOA and DOD of all targets.

4.4.1 Manifold Extender

The manifold extender involves a complex mapping of spatial manifold to extended manifold using additional system parameters. In this chapter these additional parameters are the DOD, radar's range bins, the PN-code matrix $\mathbb{C}$ and the Doppler frequency. That is

$$\boxed{\underline{S}_k\text{: is a function of DOA}_k,\ F_c,\ c \text{ and array geometry}} \tag{4.29}$$

$$\boxed{\underline{h}_k\text{: is a function of } \underline{S}_k \text{ (see Equ. 4.29) plus DOD}_k,\ \mathbb{C},\ \ell_k,\ \mathcal{F}_k} \tag{4.30}$$

This implies that:

- at Point-H of Figure 4.1: $\underline{x}(t_\ell) \in \mathcal{C}^{N\times 1}$, with

$$\underline{x}(t_\ell) = \left(\sum_{k=1}^{K} \text{function of } \underline{S}_k\right) + \text{clutter} + \text{ noise} \tag{4.31}$$

- at Point-I of Figure 4.1: $\underline{x}_{\text{vst}}[n] \in \mathcal{C}^{NN_{ext}\times 1}$, with

$$\underline{x}_{\text{vst}}[n] = \left(\sum_{k=1}^{K} \text{function of } \underline{h}_k\right) + \text{clutter} + \text{ noise} \tag{4.32}$$

where

$$N_{ext} = \overline{N} N_p \mathcal{N}_c$$

To go from Equation 4.31 to Equation 4.32 the input data at Point-H should be re-arranged in a suitable way so that Equation 4.29 is transformed to Equation 4.30. This re-arrangement of data is shown in Figure 4.4 and is described as follows:

- The snapshot at time instant t_ℓ is denoted so far by $\underline{x}(t_\ell)$ where ℓ takes values $1, 2, ..., N_s N_p \mathcal{N}_c$ representing the whole CPI. However, for every PRI we collect its $N_p \mathcal{N}_c$ snapshot vectors. To reflect this collection of snapshots to a specific PRI, the notation of the snapshot $\underline{x}(t_\ell)$ with ℓ taking values $1, 2, ..., N_p \mathcal{N}_c$ is updated by adding a second subscript, n, i.e. $\underline{x}(t_{n,\ell})$, to indicate the ℓ^{th} snapshot in the n^{th} PRI, with ℓ now taking values $1, 2, \ldots,$ $N_p \mathcal{N}_c$ and $n = 1, 2, \ldots, N_s$. This snapshot can be modelled as:

$$\begin{aligned}
\underline{x}(t_{n,\ell}) &= \sum_{k=1}^{K} \underbrace{\sqrt{P_{Tx}}\beta_k \mathrm{a}[n] \exp(j2\pi\mathcal{F}_k \ell T_c) \underline{\overline{S}}_k^H \left[\left(\mathbb{J}^{d_k}\mathbb{C}_{ex}\right)^T\right]}_{\text{scalar}_{k_{n,\ell}}} \underline{S}_k && \text{(4.33a)} \\
&\quad + \underline{x}_c(t_{n,\ell}) + \underline{\mathrm{n}}(t_{n,\ell}) \\
&= \sum_{k=1}^{K} \text{scalar}_{k_{n,\ell}} \; \underline{S}_k + \underline{x}_c(t_{n,\ell}) + \underline{\mathrm{n}}(t_{n,\ell}) && \text{(4.33b)}
\end{aligned}$$

where $\underline{\text{col}}_\ell \left[\left(\mathbb{J}^{d_k}\mathbb{C}_{ex}\right)^T\right]$ denotes the ℓ-th column of the matrix $\left(\mathbb{J}^{d_k}\mathbb{C}_{ex}\right)^T \in$

$\mathcal{R}^{\overline{N}\times N_p\mathcal{N}_c}$

$$\left(\mathbb{J}^{d_k}\mathbb{C}_{ex}\right)^T = \begin{bmatrix} \underbrace{\begin{matrix} 0, & \cdots & 0, \\ 0, & \cdots & 0, \\ \vdots & & \vdots \\ 0, & \cdots & 0, \end{matrix}}_{\substack{d_k \text{ columns} \\ \overline{N} \text{ zeros}}} & \overbrace{\begin{matrix} \alpha_1[1], & & \alpha_1[\mathcal{N}_c], \\ \alpha_2[1], & \cdots & \alpha_2[\mathcal{N}_c], \\ \vdots & & \vdots \\ \alpha_{\overline{N}}[1], & \cdots & \alpha_{\overline{N}}[\mathcal{N}_c], \end{matrix}}^{\triangleq\mathbb{C}^T} & \underbrace{\begin{matrix} 0, & \cdots & 0 \\ 0, & \cdots & 0 \\ \vdots & & \vdots \\ 0, & \cdots & 0 \end{matrix}}_{\substack{N_p\mathcal{N}_c-\mathcal{N}_c-d_k \\ \text{columns of } \overline{N} \text{ zeros}}} \end{bmatrix} \tag{4.34}$$

Note that the shifting matrix $\mathbb{J} \in \mathcal{R}^{N_p\mathcal{N}_c\times N_p\mathcal{N}_c}$ is defined as

$$\mathbb{J} = \begin{bmatrix} \underline{0}^T_{N_p\mathcal{N}_c-1}, & 0 \\ \mathbb{I}_{N_p\mathcal{N}_c-1}, & \underline{0}_{N_p\mathcal{N}_c-1} \end{bmatrix} \tag{4.35}$$

and the operation of the $\mathbb{J}^{d_k}\mathbb{C}_{ex}$ is down shifting the columns of the code matrix $\mathbb{C}_{ex}$ by d_k elements, which is the amount of discrete delay d_k corresponding to the k-th target.

- the snapshots are assembled first into PRIs and then CPI interval, as shown in Figure 4.4a. The ℓ^{th} snapshot of the 1^{st} PRI is also shown in Figure 4.4a as $\underline{x}(t_{1,\ell})$. Thus during an observation interval of $N_p\mathcal{N}_c$ snapshots, corresponding to the data matrix of the n^{th} PRI $\mathbb{X}[n] \in \mathcal{C}^{N\times N_p\mathcal{N}_c}$ can be modelled as follows:

$$\begin{aligned} \mathbb{X}[n] &= \left[\underline{x}(t_{n,1}), \quad ..., \quad \underline{x}(t_{n,\ell}), \quad ..., \quad \underline{x}(t_{n,N_p\mathcal{N}_c})\right] && \text{(4.36a)} \\ &= \overbrace{\sum_{k=1}^{K}\sqrt{P_{Tx}}\beta_k\mathrm{a}[n]\underline{S}_k\underline{\overline{S}}_k^H\left(\overbrace{\left(\mathbb{J}^{d_k}\mathbb{C}_{ex}\right)^T\odot\left(\underline{1}_{\overline{N}}\underline{\mathcal{F}}^T_{c,k}\right)}^{\triangleq\mathbb{T}(d_k,\mathcal{F}_k)}\right)}^{\text{(echoes from } K\text{-targets)}} \\ &\quad +\mathbb{X}_c[n] \quad \text{(clutter term)} \\ &\quad +\mathbb{N}[n] \quad \text{(noise term)} && \text{(4.36b)} \end{aligned}$$

where

$$\underline{\mathcal{F}}_{c,k} \triangleq \exp\left(j2\pi\mathcal{F}_k \begin{bmatrix} 1 \\ 2 \\ \vdots \\ N_p\mathcal{N}_c \end{bmatrix} T_c \right) \in \mathcal{C}^{N_p\mathcal{N}_c\times 1} \tag{4.37}$$

$$\mathbb{X}_c[n] = \left[\underline{x}_c(t_{n,1}), \quad \ldots, \quad \underline{x}_c(t_{n,\ell}), \quad \ldots, \quad \underline{x}_c(t_{n,N_p\mathcal{N}_c})\right] \tag{4.38}$$

$$\mathbb{N}[n] = \left[\underline{\mathrm{n}}(t_{n,1}), \quad \ldots, \quad \underline{\mathrm{n}}(t_{n,\ell}), \quad \ldots, \quad \underline{\mathrm{n}}(t_{n,N_p\mathcal{N}_c})\right] \tag{4.39}$$

- Vectorisation of Equation 4.36a will provide the n^{th} column (associated with n^{th} PRI) of Figure 4.4b represented by the vector $\underline{x}_{\text{st}}[n]$ which is modelled as follows:

$$\underline{x}_{\text{st}}[n] = \operatorname{vec}\left(\mathbb{X}^T[n]\right) \in \mathcal{C}^{NN_p\mathcal{N}_c\times 1} \tag{4.40a}$$

$$= \sum_{k=1}^{K} \sqrt{P_{Tx}}\beta_k \mathrm{a}[n] \underbrace{\underline{\overline{S}}_k^H \underline{1}_{\overline{N}}}_{\text{scalar}} \left(\underbrace{\underline{S}_k \otimes \left(\mathbb{J}^{d_k}\underline{c}_s \odot \underline{\mathcal{F}}_{c,k}\right)}_{\underline{h}_{\text{st},k}} \right) \tag{4.40b}$$

with the composite code vector $\underline{c}_s$ defined as the addition of all the $\overline{N}$ PN-codes that is:

$$\underline{c}_s \triangleq \mathbb{C}_{ex}\underline{1}_{\overline{N}} \in \mathcal{R}^{N_p\mathcal{N}_c\times 1} \tag{4.41}$$

- Finally the vec $\left(\mathbb{X}^T[n]\right)$ is projected as follows to provide one column of Figure 4.4c

$$\underline{x}_{\text{vst}}[n] = \begin{bmatrix} \left(\mathbb{I}_N \otimes \mathbb{P}^{\perp}_{\mathbb{B}_1}\right) \\ \left(\mathbb{I}_N \otimes \mathbb{P}^{\perp}_{\mathbb{B}_2}\right) \\ \vdots \\ \left(\mathbb{I}_N \otimes \mathbb{P}^{\perp}_{\mathbb{B}_m}\right) \\ \vdots \\ \left(\mathbb{I}_N \otimes \mathbb{P}^{\perp}_{\mathbb{B}_{\overline{N}}}\right) \end{bmatrix} \underbrace{\operatorname{vec}\left(\mathbb{X}^T[n]\right)}_{\triangleq \underline{x}_{\text{st}}[n]} \tag{4.42a}$$

$$= \sum_{k=1}^{K} \sqrt{P_{Tx}}\beta_k \mathrm{a}[n]\mathbb{P}_{\mathbb{B}}^{\perp}\underline{h}_k + \underline{x}_{\mathrm{v,c}}[n] + \underline{\mathrm{n}}_{\mathrm{v}}[n] \tag{4.42b}$$

where

$$\underline{h}_k \triangleq \underline{S}_k \otimes \underline{\overline{S}}_k^* \otimes \left(\mathbb{J}^{d_k}\underline{c}_s \odot \underline{\mathcal{F}}_{c,k}\right) \tag{4.43}$$

and $\mathbb{P}_{\mathbb{B}_m}^{\perp} \in \mathcal{C}^{N_p\mathcal{N}_c \times N_p\mathcal{N}_c}$ is a complement subspace projection operator to isolate the signal from m-th Tx antenna from the rest and is defined as

$$\mathbb{P}_{\mathbb{B}_m}^{\perp} \triangleq \mathbb{I}_{N_p\mathcal{N}_c} - \mathbb{B}_m \left(\mathbb{B}_m^H\mathbb{B}_m\right)^{-1}\mathbb{B}_m^H \tag{4.44}$$

with

$$\mathbb{B}_m = \begin{bmatrix} \mathbb{J}^{d_1}\mathbb{C}_m \odot \left(\underline{\mathcal{F}}_{c,1}\underline{1}_{\overline{N}-1}^T\right) \\ \mathbb{J}^{d_2}\mathbb{C}_m \odot \left(\underline{\mathcal{F}}_{c,2}\underline{1}_{\overline{N}-1}^T\right) \\ \vdots \\ \mathbb{J}^{d_K}\mathbb{C}_m \odot \left(\underline{\mathcal{F}}_{c,K}\underline{1}_{\overline{N}-1}^T\right) \end{bmatrix}^T \tag{4.45}$$

note that the matrix $\mathbb{B}_m \in \mathcal{C}^{N_p\mathcal{N}_c \times K(\overline{N}-1)}$ represents the part of extended array response vector covering delay and Doppler parameters for K targets. where $\mathbb{C}_m \in \mathcal{C}^{N_p\mathcal{N}_c \times (\overline{N}-1)}$ is the code matrix $\mathbb{C}_{ex,m}$ with m-th antenna's code removed as shown below:

$$\mathbb{C}_m = \left[\underline{c}_1, \quad \cdots, \quad \underline{c}_{m-1}, \quad \underline{c}_{m+1}, \quad \cdots, \quad \underline{c}_{\overline{N}}\right] \tag{4.46}$$

A similar projection operator matrix $\mathbb{P}_{\mathbb{B}}^{\perp} \in \mathcal{C}^{N\overline{N}N_p\mathcal{N}_c \times N\overline{N}N_p\mathcal{N}_c}$ can be formed for every m, that is for all antennas, and the overall operator for the whole array can be represented as follows:

$$\mathbb{P}_{\mathbb{B}}^{\perp} = \begin{bmatrix} \mathbb{I}_N \otimes \mathbb{P}_{\mathbb{B}_1}^{\perp}, & \mathbb{O}_{NN_p\mathcal{N}_c}, & \cdots, & \mathbb{O}_{NN_p\mathcal{N}_c}, \\ \mathbb{O}_{NN_p\mathcal{N}_c}, & \mathbb{I}_N \otimes \mathbb{P}_{\mathbb{B}_2}^{\perp}, & \cdots, & \mathbb{O}_{NN_p\mathcal{N}_c}, \\ \vdots & \vdots & \ddots & \vdots \\ \mathbb{O}_{NN_p\mathcal{N}_c}, & \mathbb{O}_{NN_p\mathcal{N}_c}, & \cdots, & \mathbb{I}_N \otimes \mathbb{P}_{\mathbb{B}_{\overline{N}}}^{\perp} \end{bmatrix} \tag{4.47}$$

Equation 4.42b reveals that $\underline{x}_{\mathrm{vst}}[n]$ is a function of the extended array manifold vector $\underline{h}_k \in \mathcal{C}^{N\overline{N}N_p\mathcal{N}_c\times 1}$

4.4.2 Joint Range and Doppler Estimation

First, the range $= d_k T_c c$ and the Doppler $\mathcal{F}_k \forall k$, can be estimated using the following cost function:

$$(\underline{d}, \underline{\mathcal{F}}) = \arg \max_{d,\mathcal{F}} \xi(d, \mathcal{F}), \forall d, \mathcal{F} \tag{4.48}$$

where

$$\xi(d, \mathcal{F}) = \frac{\det\left(\mathbb{T}(d, \mathcal{F})^H \mathbb{T}(d, \mathcal{F})\right)}{\det\left(\mathbb{T}(d, \mathcal{F})^H \mathbb{P}_n \mathbb{T}(d, \mathcal{F})\right)}, \forall d, \mathcal{F} \tag{4.49}$$

with

$$\mathbb{T}(d, \mathcal{F}) = \mathbb{J}^d \mathbb{C}_{ex} \odot (\underline{1}_{\overline{N}} \underline{\mathcal{F}}_c) \tag{4.50}$$

$\mathbb{T}(d, \mathcal{F})$ is the transformation matrix defined in Equation 4.36a. Furthermore, the matrix $\mathbb{P}_n$ in Equation 4.49, is the projection operator to the noise subspace, spanned by the "noise" eigenvalues of the data covariance matrix

$$\mathbb{R}_{\mathbb{X}\mathbb{X}} = \frac{1}{N.N_s} \sum_{n=1}^{N_s} \mathbb{X}[n]\mathbb{X}[n]^H \tag{4.51}$$

4.4.3 Joint DOA and DOD Estimation

Using the above-estimated delay and Doppler, the complement projection operator $\mathbb{P}_{\mathbb{B}}^{\perp}$ can be constructed to form the virtual spatiotemporal snapshot vector $\underline{x}_{\text{vst}}[n]$. This enables to estimate the DOA and DOD using the cost function below:

$$(\underline{\theta}, \underline{\overline{\theta}}) = \arg \max_{\forall(\theta,\overline{\theta})} \left. \xi(\theta, \overline{\theta}) \right|_{d=d_k,,\mathcal{F}=\mathcal{F}_k}, \forall \theta, \overline{\theta} \tag{4.52}$$

and $\xi(\theta, \overline{\theta})$ can be defined as below:

$$\xi(\theta, \overline{\theta}) \triangleq \sum_{k=1}^{K} \left(\frac{\left\| \mathbb{P}_{\mathbb{B}}^{\perp} \underline{h}_k(\theta, \overline{\theta}) \right\|^2}{\left(\mathbb{P}_{\mathbb{B}}^{\perp} \underline{h}_k(\theta, \overline{\theta})\right)^H \mathbb{P}_{n\text{v}} \left(\mathbb{P}_{\mathbb{B}}^{\perp} \underline{h}_k(\theta, \overline{\theta})\right)} \right), \forall \theta, \forall \overline{\theta} \tag{4.53}$$

where $\mathbb{P}_{n\mathrm{v}}$ is the projection operator to the noise subspace spanned by the "noise" eigenvector of the covariance matrix of the virtual-spatio-temporal snapshots given by Equation 4.42a

$$\mathbb{R}_{xx} = \frac{1}{N_s} \sum_{n=1}^{N_s} \underline{x}_{\mathrm{vst}}[n] \underline{x}_{\mathrm{vst}}[n]^H \tag{4.54}$$

4.5 Computer Simulations

In this section, the performance of the proposed approach is examined using computer simulation studies. Table 4.1 lists the system's parameters. The RF carrier frequency is 1.3 GHz. The DAC and ADC sampling interval, T_s, equals the chip interval, T_c. The unambiguous range, R_u, encompassing 262 compressed range bins, and the PRI of $2R_uT_c$ are assumed. A 15-chip PN code is utilised for pulse compression. Given the far-field target locations, a plane wave propagation model is adopted. The simulations assume successful target detection before parameter estimation. All subspace algorithms rely on accurate target count estimation. For simplicity, the elevation angle is assumed to be zero during signal modelling and estimation.

As shown in Figure 4.5, both the radar's Tx and Rx use UCAs. The Rx antenna array elements are separated by a distance $d = \frac{\lambda}{2}$ while the Tx elements are separated by $3d$ and each element has a unity gain ($G_{Tx} = G_{Rx} = 1$). Equations 4.55a and 4.56a provide the Tx and Rx antenna array geometries (Cartesian coordinates) on a 3-D real space in meters. The Tx and Rx arrays or sites are separated by $L_{bi} = 95$ units of compressed range bins. All antenna array elements are along the x and y-axis, and no element is across the z-axis.

Table 4.1: System's parameters

Parameter	Value	Comment
F_c	1.3 GHz	RF Carrier Frequency
T_c, T_s	$T_s = T_c$	Chip interval = Sampling frequency
B	$\frac{1}{T_c}$	RF bandwidth
$\overline{N}, N$	5	Tx and Rx UCAs elements
Rx SNR	20 dB	Rx Signal to Noise Ratio
SCR	$-5dB$	Rx Signal to Clutter Ratio
$\mathcal{N}_c$	15	PN-code length/period
T_p	$T_c\mathcal{N}_c$	Pulse duration
R_u	262	Unambiguous range (in units of compressed range bins)
PRI	$2R_uT_c$	
PRF	$\frac{1}{\text{PRI}}$	
L	$\frac{\text{PRI}}{T_c}$	Compressed Range bins per PRI
N_s	256	Number of PRIs per CPI

$$\underline{\underline{\overline{\mathbf{r}}}} = \left[\underline{\overline{r}}_1, \quad \underline{\overline{r}}_2, \quad \ldots, \quad \underline{\overline{r}}_{\overline{N}}\right] \tag{4.55a}$$

$$= \begin{bmatrix} 0.28, & 0.09, & -0.22, & -0.22, & 0.09 \\ 0, & 0.26, & 0.16, & -0.16, & -0.26 \\ 0, & 0, & 0, & 0, & 0 \end{bmatrix} \tag{4.55b}$$

$$\underline{\underline{\mathbf{r}}} = \left[\underline{r}_1, \quad \underline{r}_2, \quad \ldots, \quad \underline{r}_N\right] \tag{4.56a}$$

$$= \begin{bmatrix} 0.092, & 0.028, & -0.074, & -0.074, & 0.028 \\ 0, & 0.087, & 0.054, & -0.054, & -0.087 \\ 0, & 0, & 0, & 0, & 0 \end{bmatrix} \tag{4.56b}$$

where d is defined as:

$$d = \frac{\lambda}{2} = \frac{c}{2F_c}$$

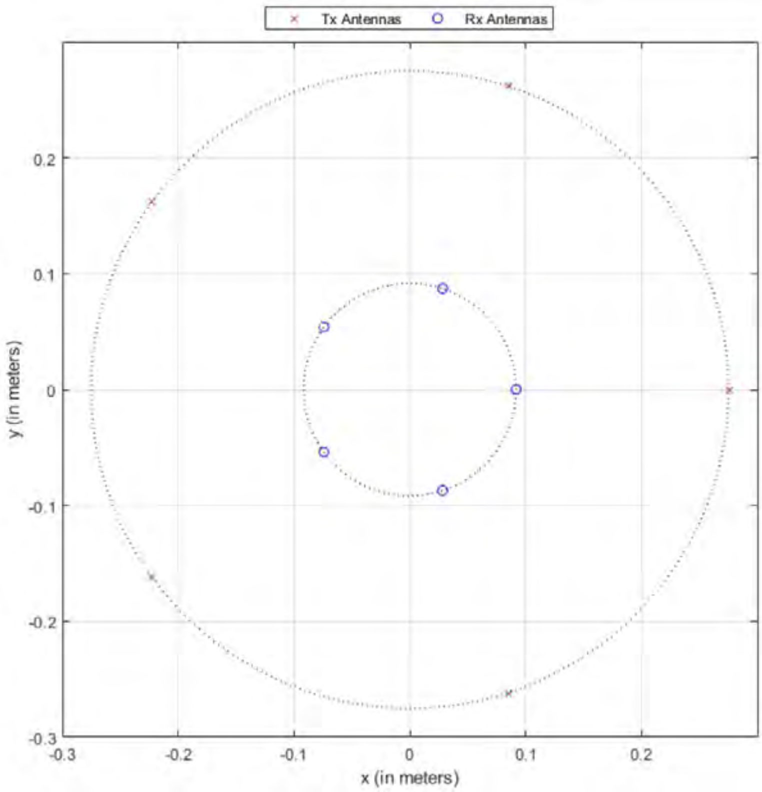

Figure 4.5: Tx and Rx UCAs

Figure 4.5 shows both antenna arrays with reference to their own local reference points. The figure does not show the distance between the Tx and Rx array. Figure 4.6 shows a bistatic radar system with Tx and Rx Cartesian coordinate location and three targets on the (x, y) plane. The elevation angle is assumed zero.

Table 4.2 summarises the geometric parameters of three targets along with their RCS model and average values. From this table,

RCS values in conjunction with the Swerling probability density functions, are used to generate the received reflections (random numbers) for each target.

As described in Section 2, the transmitted waveform with PN-codes (either m-code or Gold codes) for pulse compression provides orthogonality within a PRI period. The period could be adjusted for required target illumination and the resulting signal-to-noise ratio.

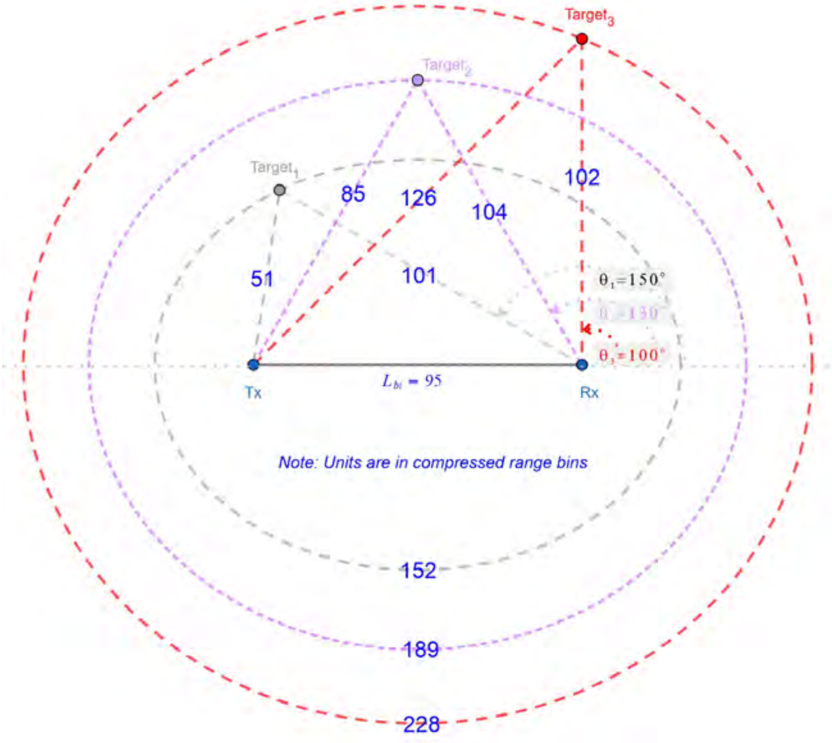

Figure 4.6: Targets' geometry

The radar also is assumed to operate in the presence of ground clutter and AWGN. The ground clutter can be modelled using various other PDFs such as K-distribution and Weibull etc. It is often challenging to model and filter various types of clutters accurately because different objects/terrains cannot be represented by a single model. One effective approach is to transform the clutter PDFs to Gaussian, i.e. transform the coloured clutter to white noise (isotropic) and then filter it out the same way as white noise [31]. The clutter transformation for this experiment is implemented as described in [31].

Table 4.2: Targets' parameters

Parameter	Target-1	Target-2	Target-3	Comments
R_{Tx}	51	85	126	Tx to Target range (in compressed range bins)
R_{Rx}	101	104	102	Rx to Target range (in compressed range bins)
R_{bi}	152	189	228	Bistatic range = $R_{Tx} + R_{Rx}$ (in compressed range bins)
θ	150°	130°	100°	DOA
$\overline{\theta}$	81.20°	70.83°	52.31°	DOD
ζ	68.80°	59.17°	47.69°	Bistatic Angle
RCS	1.0 m^2	1.5 m^2	2 m^2	
Swerling Model	1st model	2nd model	3rd model	Swerling model for RCS
v	-60 m/sec	20 m/sec	60 m/sec	Radial Velocity

4.5.1 Range and Doppler Estimation

The range and Doppler can be estimated jointly by just utilising temporal dimension of the data and array manifold. Therefore, the cost function of Equation 4.49 is used for the estimation. Figure 4.7 shows that the peaks are sharp, and the estimates are very close to the range and Doppler resolution error. The results are summarised in Table 4.3 below.

Table 4.3: Bistatic range and Doppler estimations

	$R_{bi}(T_c)$		Doppler (Hz)	
Target	True	Estimated	True	Estimated
1	152	152	-429.37	-428.37
2	189	189	150.84	151.13
3	228	228	475.94	475.13

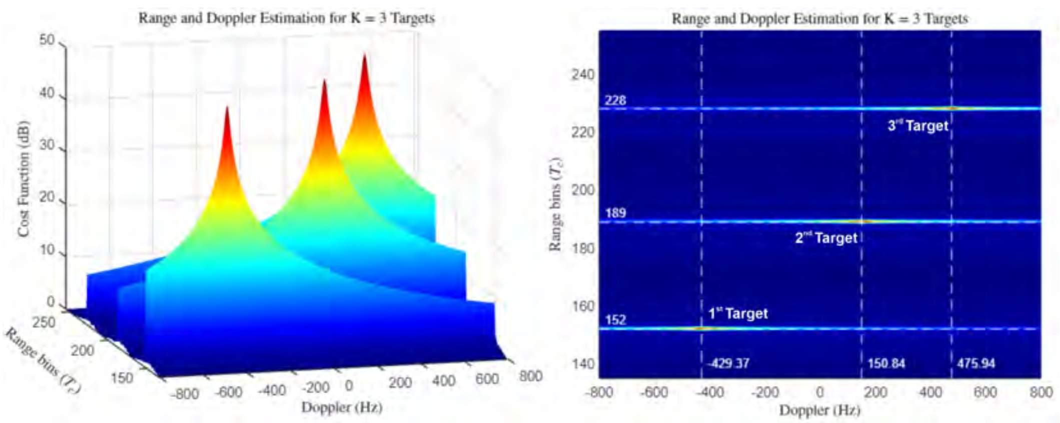

Figure 4.7: Range and Doppler estimation.

4.5.2 DOA and DOD Estimation

A joint DOA and DOD estimation is performed using the cost function of Equation 4.53. As shown in Figure 4.8 and Table 4.4 below, the estimates are very close.

4.5.3 RMSE and Comparison

The algorithm, as described in Equation 4.53, has been rigorously evaluated using Monte Carlo simulations and the RMSE metric. A comparative analysis has been

Table 4.4: DOA and DOD estimations

	$\bar{\theta}$		θ	
Target	True	Estimated	True	Estimated
1	81.20°	81.20°	150.00°	150.01°
2	70.83°	70.83°	130.00°	130.01°
3	52.31°	52.31°	100.00°	100.02°

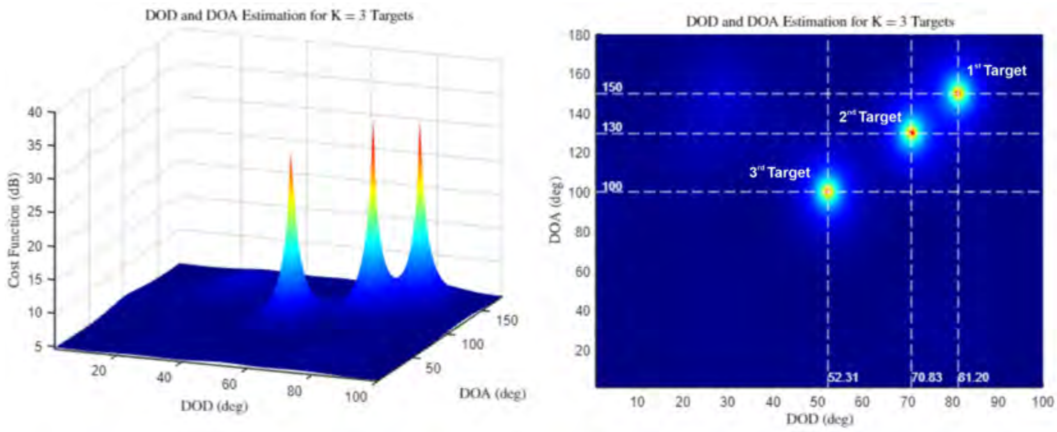

Figure 4.8: DOA and DOD estimation.

performed against the standard bistatic radar estimation method provided in Appendix A. The error metric for the parameter of interest, p, is defined in Equation 3.27 of Chapter 3.

The comparison depicted in Figure 4.9 is annotated with subscript letters corresponding to the DOD and DOA values in the legend, represented as follows:

- $\text{DOD}_{\text{v-ST}}$: DOD with v-ST algorithm.
- $\text{DOA}_{\text{v-ST}}$: DOA with v-ST algorithm.
- DOD_{m}: DOD with MUSIC algorithm and bistatic geometry.
- DOA_{m}: DOA with MUSIC algorithm.

The performance depicted in the figure demonstrates the superior efficacy of the proposed virtual Spatiotemporal (v-ST) algorithm when compared to conventional bistatic estimation techniques. It is noteworthy that the DOD_{m} exhibits a floor-

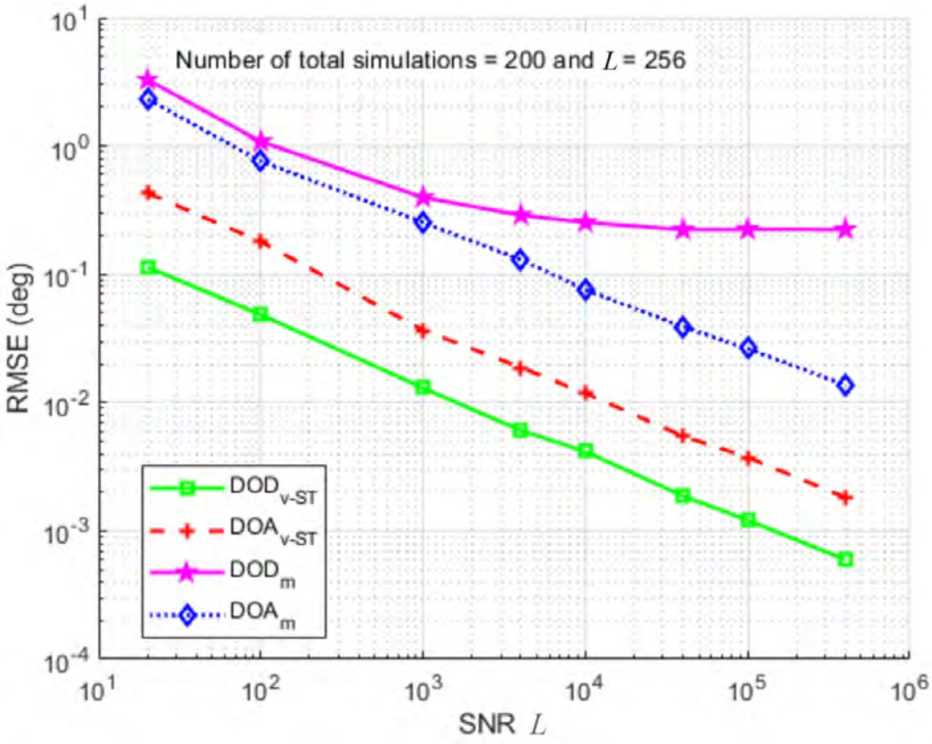

Figure 4.9: DOA and DOD RMSE

level trend beyond the mid-trace, attributable to range floor-level quantization error limitations.

Next, the v-ST algorithm will be compared with the DOA and DOD estimation algorithm presented in Chapter 3. To ensure a fair comparison, the system parameters were aligned with those used in Chapter 3. The modified parameters are listed below:

- Both systems utilized UCA antenna arrays with $N = \overline{N} = 5$ and $d = \frac{\lambda}{2}$ and 2λ respectively.
- Fc = 10 GHz
- Target's beta and RCS are the same as in Chapter 3
- Number of pulses in one frame, i.e. $L = 160$ (for STC system code period = 16 and subframes = 10)

Figure 4.10 shows the RMSE comparison between the MUSIC, v-ST, and the algorithm presented in Chapter 3, with legend's entries subscripted with 'stc'. It

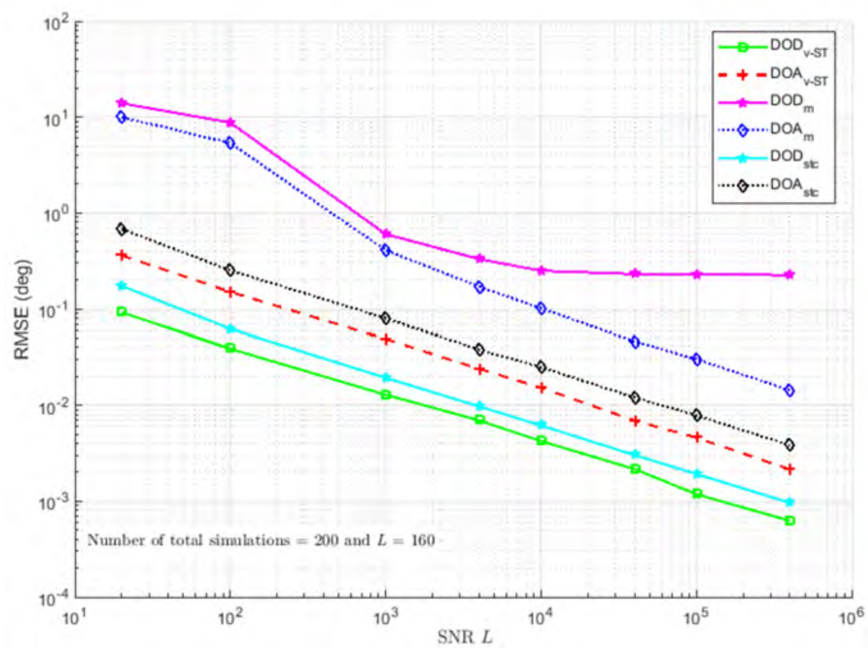

Figure 4.10: Comparison of RMSE for DOD and DOA in STC and FTC systems.

is clear that the v-ST algorithm performed better, as expected, due to its use of a longer extended array. However, the STC algorithm also performed well, closely following the performance of the v-ST algorithm.

4.6 Summary

In conclusion, this chapter investigated the application of novel subspace algorithms for parameter estimation in MIMO bistatic pulse radar systems. The proposed approach uses a unique PN-code for each transmit chain, maximising the observation space by utilising both the Tx and Rx observation spaces. The channel model incorporates K moving targets with Swerling-distributed RCS and accounts for clutter and noise. The received signal model is constructed, and a 3D radar data cube is assembled. This data undergoes processing through Spatiotemporal and Virtual Spatiotemporal manifold extenders to increase the degree of freedom and improved parameter estimation.

Computer simulations were conducted to evaluate the performance of the proposed DOA and DOD estimation algorithm. Using Monte Carlo simulations and

RMSE as metrics, the proposed system in this chapter was compared with the bistatic MIMO radar equations, the MUSIC algorithm, and the algorithm presented in Chapter 3. The results demonstrated the superior performance of the system proposed in this chapter.

4.7 Appendices

Appendix 4.A: Bistatic Estimation Process

1. Compute the bistatic range estimation (R_{bi}) using Equation 4.49.

2. Using L_{bi} and R_{bi}, determine the following bistatic target's ellipse parameters:

   - semi-major axis a
   - semi-minor axis b, and
   - its eccentricity ε,

   using Equations 4.59-4.61 of Appendix B.

3. Calculate the Tx to Target Range (R_{Tx}) and Target to Rx Range (R_{Rx}) using Equations 4.62 and 4.63 of Appendix B.

4. Using the MUSIC algorithm, estimate the $\mathrm{DOA_m}$.

5. Estimate the $\mathrm{DOD_m}$ using Equation 4.64 given in Appendix B

Appendix 4.B: Bistatic Equations

The estimated target delay parameters d_k can be converted to bistatic range R_{bi} as follows.

$$R_{bi,k} = d\ c\ T_c\ |_{d=d_k}, \forall k \tag{4.57}$$

$$R_{bi,k} = R_{Tx,k} + R_{Rx,k} \tag{4.58}$$

With reference to Figure 4.11 which shows a bistatic ellipse and its parameters, the values $R_{bi,k}$ and L_{bi} can be used to estimate the parameters a_k, b_k and ε_k as follows:

$$\text{semi-major axis } a_k = \frac{R_{bi,k}}{2}, \forall k \tag{4.59}$$

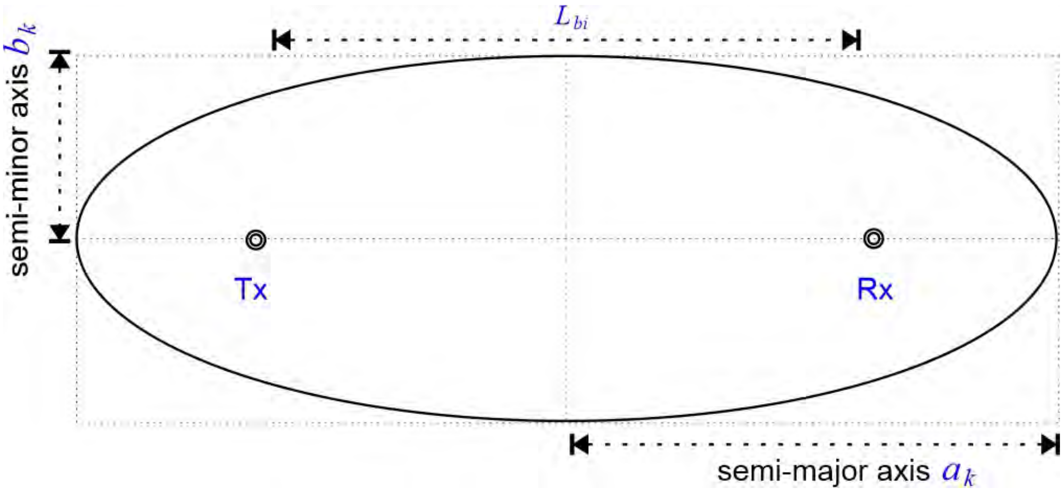

Figure 4.11: Ellipse notations

$$\text{semi-minor axis } b_k = \sqrt{R_{bi,k}^2 - \frac{L_{bi}^2}{4}} \tag{4.60}$$

$$\text{eccentricity ratio } \varepsilon_k = \frac{L_{bi}/2}{a_k} \tag{4.61}$$

Furthermore, the bistatic ranges R_{Rx} and R_{Tx} for each target can be estimated using the following equations:

$$R_{Rx,k} = \frac{a_k(\varepsilon_k^2 - 1)}{\varepsilon_k \cos(\theta_k) + 1}, \forall k \tag{4.62}$$

$$R_{Tx,k} = R_{bi,k} - R_{Rx,k} \tag{4.63}$$

Finally, using the above equation, the DOD $\overline{\theta}_k$ $\forall k$ can be estimated as follows:

$$\overline{\theta}_k = \arccos\left(\frac{1}{\varepsilon_k}\left(\frac{a_k(\varepsilon_k^2 - 1)}{R_{Tx,k}} + 1\right)\right) \tag{4.64}$$

Chapter 5

Performance Analysis

Chapter 4 describes array manifolds and extended array manifolds. Here, we revisit these concepts from a different perspective. The array response vector, $\underline{S}_k$ of N omnidirectional antennas, resides in an N-dimensional complex nonlinear subspace (think of it as a specific curved region within the N-dimensional complex space, $\in \mathcal{C}^{N\times 1}$). This subspace can be described using nonlinear mathematical objects (manifolds), such as Grassmannian manifolds commonly used in signal processing [98]. To investigate the properties of these mathematical objects (space, curves, and surfaces), differential geometry is a powerful tool [99,100]. This chapter analyses the theoretical performance limitations of the antenna arrays employed in Chapters 2, 3, and 4 in the context of MIMO radar, focusing on two key aspects crucial for accurate target tracking and localisation:

- **Cramer-Rao Lower Bound (CRB):** This bound establishes a fundamental limit on the accuracy achievable when estimating target parameters, such as direction of arrival and range.
- **Resolution Capability:** This refers to the ability to distinguish between closely spaced targets, which is essential for accurate target tracking and separation in scenarios with multiple targets.

While performance analysis is a vast subject area [60], a concise overview of the relevant expressions is provided here. The principal curvature, denoted by κ_1, of the manifold-curve is leveraged to simplify the calculations associated with the CRB and resolution bounds. These bounds serve as a "figure of merit" [101] for comparing the performance of different array geometries, allowing us to assess their effectiveness in target tracking and localisation tasks. The concept of the "uncertainty sphere," which underpins these bounds, is first introduced in the following section.

5.1 Manifold Curve and Basic Concepts

In the context of MIMO radar, a manifold curve depicts how the array manifold vector changes as a specific parameter is varied. Figure 5.1 shows an example of such a curve, labelled $\mathcal{A}$. This curve represents the path traced by the array manifold vector $\underline{a}(p)$ when a single parameter of interest p, such as the target's DOA, is swept across a range of values. Therefore, the curve $\mathcal{A}$ is defined as:

$$\mathcal{A} \triangleq \underline{a}(p) \in \mathcal{C}^N, \forall p : p \in \Omega_p \tag{5.1}$$

where Ω_p is the parameter space, considered as a regular parametrised differential curve if

$$\underline{\dot{a}}(p) \neq \underline{0}_N, \forall p \in \Omega_p \tag{5.2}$$

Here $\underline{\dot{a}}(p)$ represents differentiation of $\underline{a}(p)$ with respect to the parameter p, it is tangent vector to the curve. The tangent vector exists for all points of the array manifold because of the regularity condition of Equation 5.2. Now, along the curve $\mathcal{A}$, the arc length $s(p)$ can be defined as:

$$s(p) \triangleq \int_0^p \|\underline{\dot{a}}(p)\| \, dp \tag{5.3}$$

and its derivative or rate of change is defined as:

$$\dot{s}(p) = \frac{ds}{dp} \triangleq \|\underline{\dot{a}}(p)\| \tag{5.4}$$

In this chapter, the derivative with respect to s will be denoted by a "prime," such as $\underline{a}' \triangleq \left(\frac{d\underline{a}(s)}{ds}\right)$, while the derivative with respect to parameter p will be denoted by a "dot," such as $\underline{\dot{a}} \triangleq \left(\frac{d\underline{a}(p)}{dp}\right)$. The array manifold is typically expressed in terms of a generic bearing parameter p, such as the DOA. However, parameterisation with respect to arc length s offers several advantages over p. One key benefit is that s is an invariant parameter, meaning that the resulting tangent vector to the curve, with respect to s, always has a unit length. The proof is shown as below:

$$\|\underline{a}'(s)\| = \left\|\frac{d\underline{a}(s)}{ds}\right\| = \left\|\frac{d\underline{a}(p)/dp}{ds/dp}\right\| = \frac{\|\underline{\dot{a}}(p)\|}{\dot{s}(p)} = \frac{\dot{s}(p)}{\dot{s}(p)} = 1, \forall s \tag{5.5}$$

This invariance simplifies the analysis and ensures consistent scaling in the array manifold representation. The unit tangent vector can be defined as:

$$\underline{u}_1(s) = \underline{a}'(s) \tag{5.6}$$

The measure of how fast the curve pulls away from the tangent line at s defines its first or principal curvature. This is given by the norm of the second derivative of the manifold vector, as shown in the equation below:

$$\|\underline{a}''(s)\| = \kappa_1(s) \tag{5.7}$$

5.2 Modelling of the Uncertainty Sphere

Figure 5.1 shows the uncertainty sphere (in arc lengths) which represents the effects of additive noise of power σ^2 on the performance of an antenna array system of N antennas. This uncertainty sphere, which is embedded in an N-dimensional complex space, shrinks (i.e. its radius σ_e is gradually decreased) according to the following model [60]:

$$\sigma_e = \sqrt{\frac{\sigma^2}{2\ L\ P\ C}} = \sqrt{\frac{1}{2(\mathrm{SNR}\ L)C}}; \quad \text{(in arc lengths)} \tag{5.8}$$

The factor of “2” appearing in the denominator arises directly from the use of complex numbers to represent signal envelopes in the array model. This is because complex representations inherently involve both a real and imaginary component, effectively doubling the values compared to a real-valued representation. The symbol "L" denotes the number of snapshots, and "P" represents the signal power.

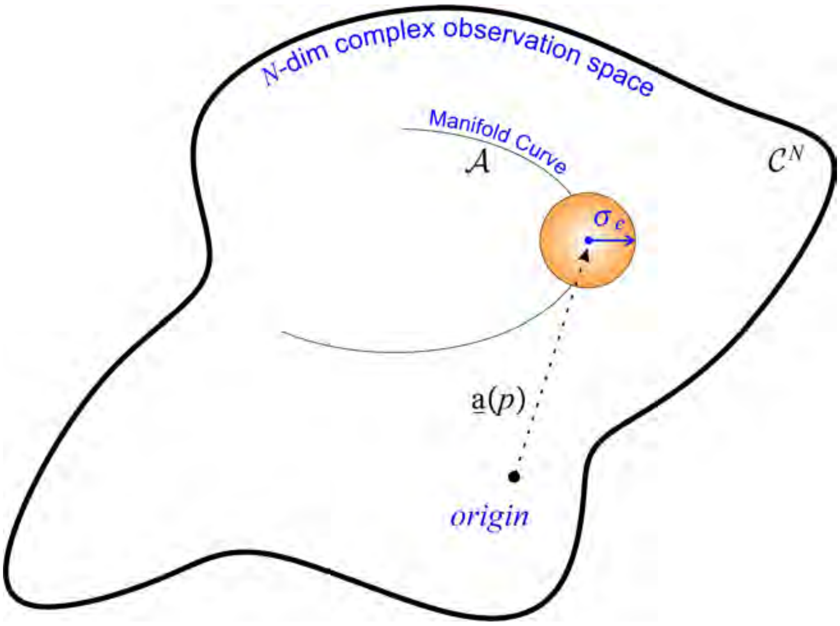

Figure 5.1: Uncertainty sphere at a point (θ, ϕ) on the manifold curve, embeded in an N-dimensional complex observation space.

The shrinking rate of the uncertainty sphere depends also on the estimation algorithm employed. Some algorithms exhibit better properties than others, thereby "masking" the overall array performance. This is modelled by the factor/parameter C where

$$0 < C \leq 1 \tag{5.9}$$

For $C = 1$, the above expression becomes a "lower-bound" and forms a benchmark against which any practical algorithm can be compared. Note that the value $C = 1$ is a theoretical limit achieved by an "ideal" algorithm.

5.3 Accuracy and the Cramer Rao Lower Bound

The CRB [102] sets a lower limit on the error covariance matrix of any unbiased estimate, $\hat{\underline{p}}$, of the true parameter vector $\underline{p} \in \mathcal{R}^M$. In the case of a *single emitter* ($M = 1$), the CRB for the (parameters of interest in this case) ϕ-estimates and

θ-estimates are expressed [60] as follows

$$\mathrm{CRB}[\phi|_{\theta=\theta_o}] = \frac{\sigma_e^2}{\left(\pi \left\|\underline{r}(\theta_o)\right\| \sin\phi\right)^2} = \frac{1}{2\,(\mathrm{SNR}\ L)\ \ \left(\pi \left\|\underline{r}(\theta_o)\right\| \sin\phi\right)^2} \quad (5.10)$$

$$\mathrm{CRB}[\theta|_{\phi=\phi_o}] = \frac{\sigma_e^2}{\left(\pi \left\|\underline{\dot{r}}(\theta)\right\| \cos\phi_o\right)^2} = \frac{1}{2\,(\mathrm{SNR}\ L)\ \ \left(\pi \left\|\underline{\dot{r}}(\theta)\right\| \cos\phi_o\right)^2} \quad (5.11)$$

where if, for example, the array is a planar array on the (x, y) plane, then $\underline{r}(\theta) = \underline{r}_x \cos\theta + \underline{r}_y \sin\theta$. Note that $\underline{\dot{r}}(\theta) = \frac{d\underline{r}(\theta)}{d\theta}$.

Expressions for the CRB become progressively more complicated with increasing numbers of emitters/targets, M, since the accuracy of the bearing estimates is not only a function of the additive sensor noise but also depend on the interactions between the various emitters/targets. If the array only receives a return from a single target, then the above expression simplifies as follows:

$$\begin{aligned}
\mathrm{CRB}[p_1] &= \frac{\sigma_e^2}{2\ L\ P}\frac{1}{\underline{\dot{\mathrm{a}}}^H(p_1)\mathbb{P}_{\mathbb{A}}^{\perp}\underline{\dot{\mathrm{a}}}(p_1)} = \frac{1}{2(\mathrm{SNR}_1\ L)}\frac{1}{\underline{\dot{\mathrm{a}}}^H(p_1)\mathbb{P}_{\mathbb{A}}^{\perp}\underline{\dot{\mathrm{a}}}(p_1)} && (5.12)\\
&= \frac{1}{2(\mathrm{SNR}_1\ L)}\frac{1}{\dot{s}(p_1)^2\underline{u}_1^H(s_1)\mathbb{P}_{\mathbb{A}}^{\perp}\underline{u}_1(s_1)} && (5.13)
\end{aligned}$$

where $\underline{\dot{\mathrm{a}}}(p_1) = \underline{u}_1(s_1)\dot{s}(p_1)$ and $\mathbb{P}_{\mathbb{A}}^{\perp}\underline{u}_1(s_1) = \underline{u}_1(s_1)$

$$\begin{aligned}
\mathbb{A} &= \left[\underline{\mathrm{a}}_1,\ \ \underline{\mathrm{a}}_2,\ \ \ldots,\ \ \underline{\mathrm{a}}_M\right]\\
\dot{\mathbb{A}} &= \left[\underline{\dot{\mathrm{a}}}_1,\ \ \underline{\dot{\mathrm{a}}}_2,\ \ \ldots,\ \ \underline{\dot{\mathrm{a}}}_M\right]\\
\mathbb{P}_{\mathbb{A}}^{\perp} &= \mathbb{I}_N - \mathbb{A}\left(\mathbb{A}^H\mathbb{A}\right)^{-1}\mathbb{A}^H
\end{aligned}$$

and for a single target and parameter $\mathbb{A} = \underline{\mathrm{a}}(p_1)$ and $\dot{\mathbb{A}}$ is its first derivative.

Now, Equation 5.13 can be interpreted for two closely spaced targets ($M = 2$) along the manifold curve $\mathcal{A}$, with the arc length $s(p_1)$ and its rate of change of $\dot{s}(p_1)$ as follows:

$$\boxed{\mathrm{CRB}[p_1|\mathcal{A}] \simeq \frac{1}{(\mathrm{SNR}_1\ L)}\frac{2}{\dot{s}(p_1)^2\ \dot{s}(\breve{p})^2\ \Delta p^2\left(\hat{\kappa}_1^2(\breve{p}) - \frac{1}{N}\right)}} \quad (5.14)$$

where $\hat{\kappa}_1^2(\breve{p})$ is the principal curvature of the manifold curve at $\breve{p}$. Note that the bearing $\breve{p}$ corresponds to the point with arc length $\breve{s}$, and to a first-order approximation, equals $(p_1 + p_2)/2$ or equivalently $\breve{p} = p_1 + \frac{\Delta p}{2}$.

It is important to point out that Equation 5.14 indicates that the CRB is inversely proportional to the square of the emitters' angular separation,

$$\mathrm{CRB}[p_1|\mathcal{A}] \propto \frac{1}{(\Delta p)^2} \tag{5.15}$$

i.e. the accuracy of the system deteriorates rapidly as the emitters approach close to one another.

5.4 Resolution Threshold

Array resolution refers to the ability to distinguish between closely spaced targets and obtain separate, albeit potentially inaccurate, parameter estimates for each target. In simpler terms, targets are considered resolved when the corresponding directions on the array manifold can be estimated. This might manifest as distinct peaks or nulls observed in the spectrum of the employed direction-finding (DF) algorithm.

Two emitters with parameters (directions) p_1 and p_2 are resolved by an "ideal" algorithm (i.e. $C = 1$) if and only if $p_2 - p_1 \geqslant \Delta p_{\text{res-thr}}$ [60] where

$$\boxed{\Delta p_{\text{res-thr}} = \frac{1}{\pi\, \|\underline{r}\|\, \sin \breve{p}} \sqrt[4]{\frac{4}{\hat{\kappa}_1^2 - \frac{1}{N}}} \left(\sqrt{\sigma_{e_{1,r}}} + \sqrt{\sigma_{e_{2,r}}}\right)} \tag{5.16}$$

This implies that the minimum angular separation $\Delta p_{\text{res-thr}}$ required for resolving two sources of powers P_1 and P_2 may be written as:

$$\boxed{\begin{aligned} &\text{Resolution threshold:} \\ &\Delta p_{\text{res-thr}} = \frac{1}{\dot{s}(\breve{p})} \sqrt[4]{\frac{2}{\left(\hat{\kappa}_1^2 - \frac{1}{N}\right)}} \\ &\qquad \times \left(\frac{1}{\sqrt[4]{\mathrm{SNR}_1\ L}} + \frac{1}{\sqrt[4]{\mathrm{SNR}_2\ L}} \right) \end{aligned}} \tag{5.17}$$

where $\dot{s}(\breve{p}) = \pi\|\underline{r}\|\sin\breve{p}$ is the rate of change of manifold arc length and bearing $\breve{p}$ corresponds to the point (to a first order approximation $\breve{p} = (p_1 + p_2)/2$).

Since $\dot{s}(\breve{p}) = \pi\|\underline{r}\|\sin\breve{p}$, Equation (5.17) indicates that the resolution capabilities of a linear array (or ELA of a planar array) are maximum at boresight ($p = 90°$) and zero along the endfire directions ($p = 0°$ or $180°$). Zero resolution along end-fire directions is expected since, due to cylindrical symmetry, two signals at directions which are symmetrical to the array axis cannot be distinguished, irrespective of their angular separation.

For the special case of equi-powered sources ($P_1 = P_2 = P$) the ultimate product (signal-to-noise ratio times L) required to resolve two sources at bearings p_1 and $p_2 = p_1 + \Delta p$ may be written as

$$\Delta p_{\text{res-thr}} \approx \frac{1}{\dot{s}(\breve{p})}\sqrt[4]{\frac{32}{\left(\hat{\kappa}_1^2 - \frac{1}{N}\right)}}\frac{1}{\sqrt[4]{\text{SNR } L}} \tag{5.18}$$

fourth-root law for resolution:

$$\boxed{\Delta p_{\text{res-thr}} \propto (\text{SNR } L)^{-1/4}} \tag{5.19}$$

In other words, the resolution ultimately achievable is inversely proportional to the fourth-root law of

- the signal-to-noise ratio
- the number of snapshots

As shown in Section 8.6.3 of [60], the directional pattern, denoted by $g(p)$, of a directional antenna primarily acts as a "voltage gain" factor that can either amplify or diminish the effective SNR at the array's output. Consequently, equations (5.10), (5.11), (5.14), and (5.17) can be reformulated by substituting SNR_1 and SNR_2 with $\text{SNR}_1 \cdot g^2(p_1)$ and $\text{SNR}_2 \cdot g^2(p_2)$, respectively.

However, for the purpose of comparing the relative performance of different array geometries, the influence of $g(p)$ can be disregarded. While the presence of directional antennas undoubtedly affects the absolute performance metrics, it does not alter the comparative advantages of one geometry over another.

5.5 Comparison of Arrays

This section analyses the theoretical performance limitations of the antenna arrays employed with Saab's data sets A and B. We focus on two key aspects: the CRB, which establishes a fundamental accuracy limit for estimating target parameters, and the resolution capabilities, which refer to the ability to distinguish closely spaced targets.

Following the analysis in the previous section, we will compare the performance of these datasets to an equal-sized UCA with all other system parameters maintained identical to those in each dataset. This comparison is relevant because Chapters 3 and 4 utilised UCA configurations for the investigated systems, allowing us to assess the relative performance under the same conditions.

In this section only azimuth direction (θ) is analysed assuming elevation angle $\phi = 0$. While performance bound analysis is a vast subject [60], we provide a concise overview of the relevant expressions here.

5.5.1 Data Set-A

In this data set, which has 22 frames, there are two UAVs (targets) and we will examine the error (lower bound) in the estimation of the 1st UAV's direction θ_1 in the presence of the 2nd UAV with direction $\theta_1 + \Delta\theta$ for variable $\Delta\theta$. This lower bound can be estimated using Equation 5.14 for

$$\theta_1 = \text{variable and } \Delta\theta = 0.1^\circ, 1^\circ, 10^\circ, 20^\circ$$

as this is shown in Figure 5.2. In the same figure, two annotated "square-points" (red and black) are also shown. These represent the estimated location $\hat{\theta}_1$ of the 1st UAV and the estimated $\Delta\hat{\theta} = \hat{\theta}_2 - \hat{\theta}_1 \simeq 2^\circ$ (where $\hat{\theta}_2$ is the estimated direction of the 2nd UAV) for

- the 1st frame - where $\hat{\theta}_1 \simeq 97^\circ$ and $\Delta\hat{\theta} = \hat{\theta}_2 - \hat{\theta}_1 \simeq 2^\circ$ and
- the last frame (22nd frame) - where $\hat{\theta}_1 \simeq 87^\circ$ and $\Delta\hat{\theta} = \hat{\theta}_2 - \hat{\theta}_1 \simeq 23^\circ$

with the values $\hat{\theta}_1$ and $\Delta\hat{\theta}$ provided by the MIMO algorithms for this set of data (*Set-A*). Note that the SNR_1 and SNR_2 of the two UAVs have been measured using the APES algorithm as follows: 1st frame $\text{SNR}_1 \approx \text{SNR}_2 \approx 42$ dB; 22nd frame $\text{SNR}_1 \approx \text{SNR}_2 \approx 23$ dB.

Table-5.1 gives the values of the main parameters that have been used in Equation 5.14 to produce the plots of Figures 5.2 and 5.3. Note that the curvature of the manifold curve has been analytically calculated using the array geometries.

Using the parameters specified in Table 5.1, the resolution threshold derived from Equation 5.17 is plotted in Figures 5.4 and 5.5.

The plots reveal that the original Rx antenna array (ULA) exhibits better estimation and resolution accuracy near the middle of the directional range (around boresight, i.e., θ_1 and $\breve{\theta}$ near 90°), while performance deteriorates at the endfire directional ranges (around 0° and 180°). This behaviour is characteristic of ULAs, which have higher gain along their broadside direction.

In contrast, the plots for the UCA show uniform performance across the entire directional range (θ from 0° to 180°). This is because UCAs provide omnidirectional gain, resulting in consistent performance regardless of the target's direction. Consequently, UCAs are often preferred for applications requiring surveillance or observation across a full 360-degree coverage area.

Table 5.1: Parameters used in the evaluation of the CRB lower bound and resolution-threshold for data Set-A

Symbols	Description	Values
L	Snapshots	160
N	Rx antenna elements	12
p_1	θ_1	variable
$\breve{p} = p_1 + \frac{\Delta p}{2}$	$\breve{\theta} = \theta_1 + \frac{\Delta\theta}{2}$	variable $+\frac{\Delta\theta}{2}$
$p_2 = p_1 + \Delta p$	$\theta_2 = \theta_1 + \Delta\theta$	variable$+\Delta\theta$
$\Delta p = p_2 - p_1$	$\Delta\theta = \theta_2 - \theta_1$	$0.1°; 1°; 10°; 20°$

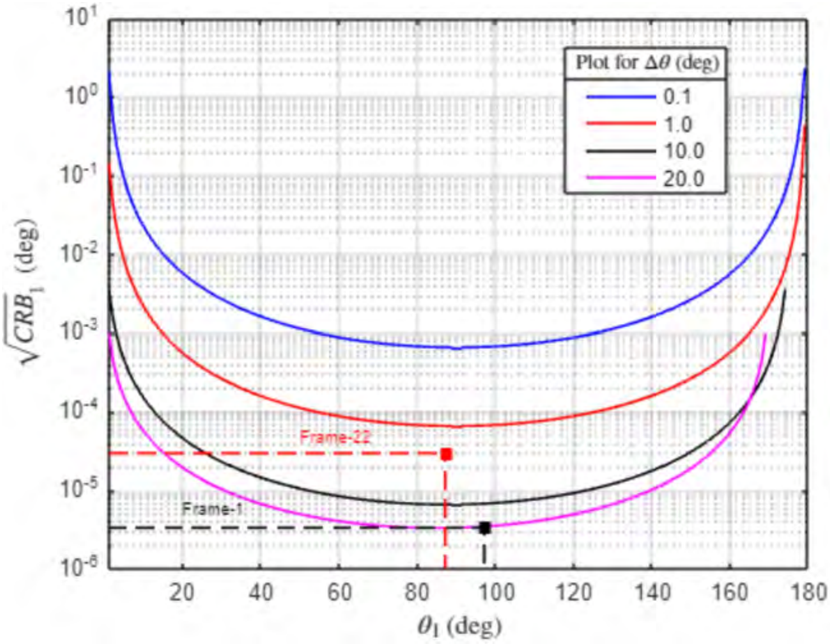

Figure 5.2: Evaluation of the CRB lower bound (estimation error), given by Equation 5.14 for the 1st target's direction θ_1 (variable) in the presence of a 2nd target with direction $\theta_1 + \Delta\theta$, for the array geometry used in data Set-A(Figure 2.5) and SNR of 1st frame.

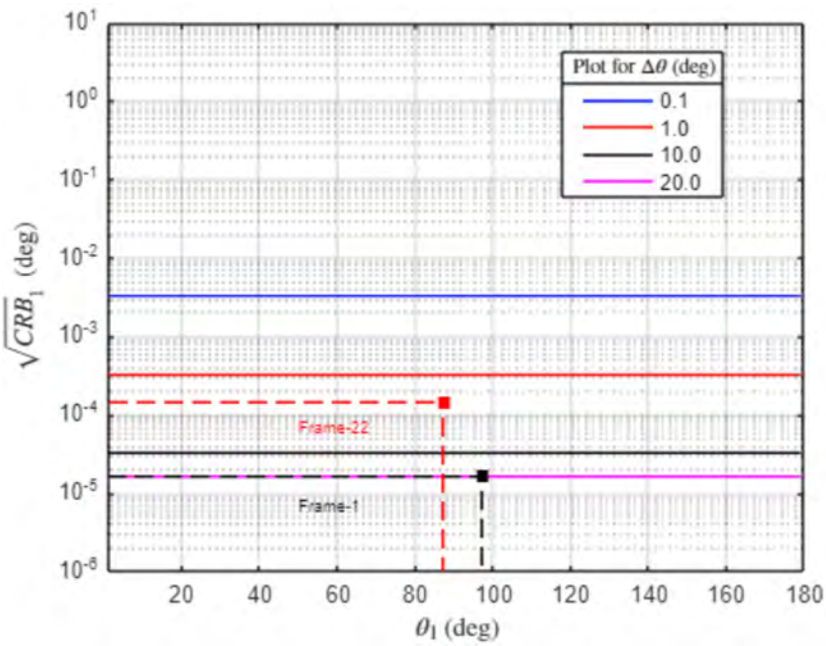

Figure 5.3: Evaluation of the CRB lower bound (estimation error), given by Equation 5.14 for the 1st target's direction θ_1 (variable) in the presence of a 2nd target with direction $\theta_1 + \Delta\theta$, for the UCA with $N = 12$ and SNR of 1st frame.

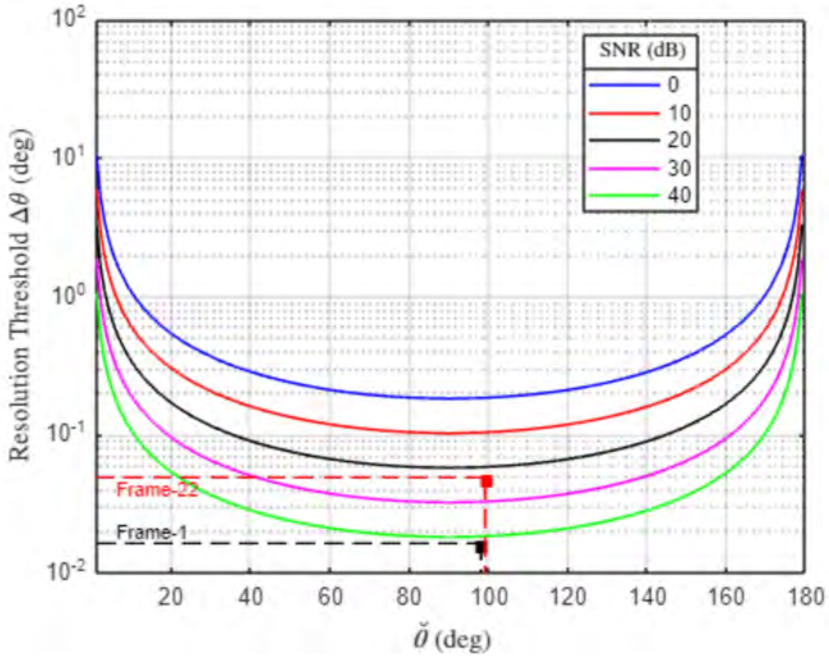

Figure 5.4: Evaluation of the resolution-threshold $\Delta\theta$, with $\breve{\theta}$ variable, given by Equation 5.17 for the array geometry used in the data Set-A(Figure 2.5).

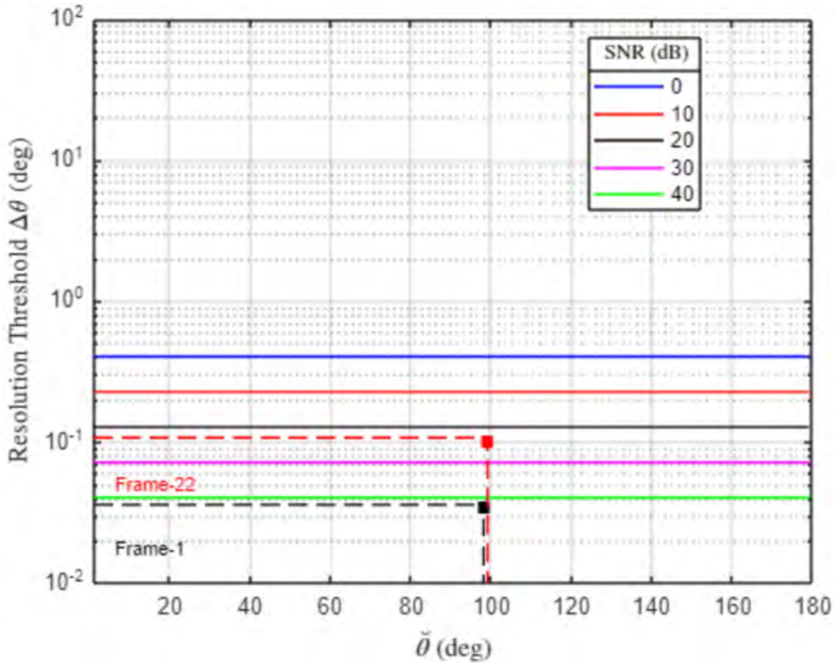

Figure 5.5: Evaluation of the resolution-threshold $\Delta\theta$, with $\breve{\theta}$ variable, given by Equation 5.17 for UCA with $N = 12$.

5.5.2 Data Set-B

This section analyses the performance of Saab's data Set-B, which contains a single UAV (target) and only 4 frames with $L = 511$. Since there is only a single target, the resolution threshold is not applicable. Therefore, we focus solely on the estimation accuracy for the direction of arrival (θ) of a single UAV (with θ variable) using the CRB as in Equation 5.11.

Figure 5.6 presents the CRB for the original array geometry (ULA), while Figure 5.7 shows the CRB for an equal-sized UCA. Both figures indicate an estimated UAV location of $\hat{\theta} = 67°$ (represented by the "square-black" annotation). It's important to note that the original Rx array geometry is identical to the one used in data Set-A. For the 4 frames in data Set-B, the estimated SNRs obtained using the APES algorithm are approximately 13.9, 14.3, 14.9, and 29.5 dB, respectively. The ULA and UCA plots show a similar trend, as discussed in the data Set-A section.

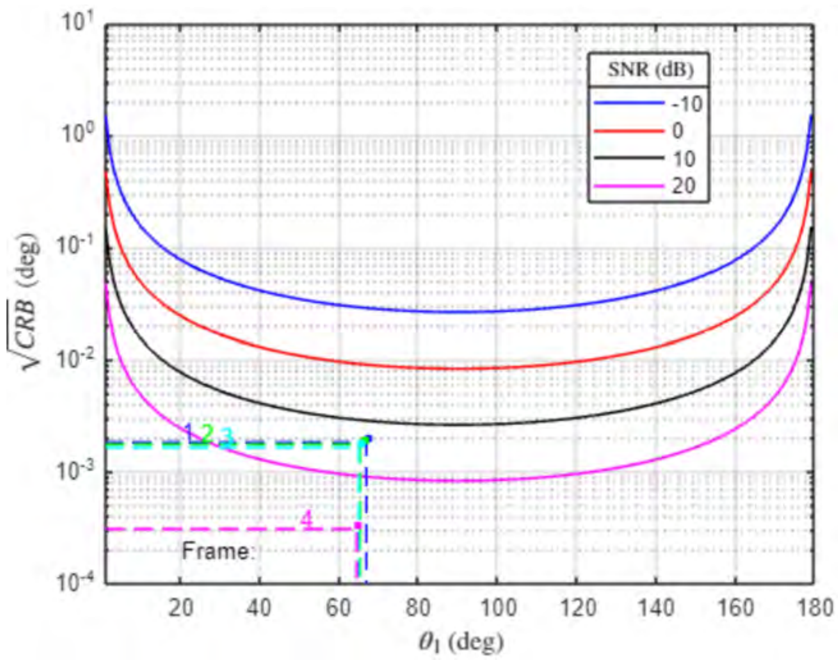

Figure 5.6: Single target CRB for the array geometry used in data Set-B(Figure 2.9.

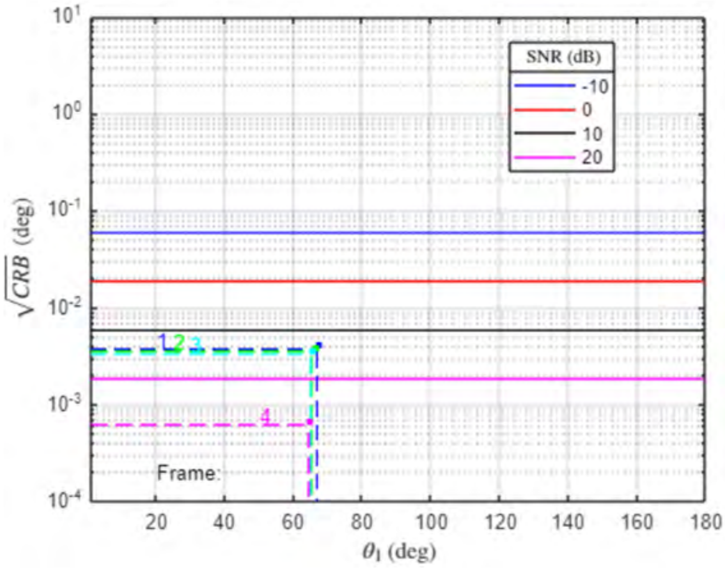

Figure 5.7: Single target CRB for the UCA with $N = 12$.

5.6 Summary

This section analysed the theoretical performance limitations of the antenna arrays employed with Saab's data sets A and B. The focus was on two key aspects:

- **Estimation Accuracy:** The CRB was used to establish a fundamental limit for the accuracy of estimating target parameters (direction of arrival, etc.).
- **Resolution Capability:** The ability to distinguish closely spaced targets was assessed based on the resolution threshold.

The concept of the uncertainty sphere was introduced to visualize the theoretical limits on parameter estimation. Equations 5.2 to 5.6 derived the CRB lower bound, while Equations 5.7 to 5.10 determined the resolution threshold.

Furthermore, the performance of data sets A and B was compared with an equal-sized UCA. This comparison revealed that the UCA exhibits similar performance across all directional ranges, unlike the original arrays, which showed better performance near boresight and worse performance at endfire directions. This behaviour is expected due to the inherent characteristics of UCA and ULA geometries.

Chapter 6

Conclusions, Further Work and List of Contributions

This thesis explored the potential of MIMO radar systems and parameter estimation algorithms to address the challenges and demands of modern radar applications. The research focused on investigating MIMO radar capabilities for detecting and estimating parameters of multiple targets. Traditional radars are designed for high-altitude, fast-moving targets like aeroplanes and fighter jets, where detecting and tracking a few objects is sufficient. However, modern scenarios involving low-cost, low-altitude, slow-speed, and numerous targets significantly exceed the capabilities of conventional radar systems.

To address these limitations, this research involved two monostatic MIMO radar experiments conducted at Saab Gothenburg, each with distinct system configurations. These experiments aimed to demonstrate the potential of MIMO radar technology in tackling the aforementioned challenges. This collaborative effort, spanning approximately nine months, involved Saab, DASA, and Imperial College London. The insights and expertise gained from these experiments laid the groundwork for further exploration and development of innovative radar architectures and parameter estimation algorithms.

6.1 Thesis Summary and Conclusions

This thesis explored MIMO radar system architectures and parameter estimation algorithms with the aim of addressing contemporary challenges and requirements. Chapter 1 delved into the recent developments in this field, providing a comprehensive literature review and introducing the core technologies and concepts necessary for understanding the subsequent chapters. This foundational chapter covered antenna arrays, array manifolds, extended array manifolds, and classical MIMO algorithms, while also highlighting the existing challenges and research gaps in the field.

Chapter 2 provided an in-depth examination of the Saab experimental monostatic MIMO radar, offering insights into its conceptual model encompassing transmitter, receiver, and multi-target channel models. Through the application of classical MIMO algorithms on real radar data, detailed analysis was conducted, shedding light on estimated parameters and their performance. The chapter further introduced and implemented virtual MIMO radar concepts to enhance estimation performance, with a comparative evaluation between classical and virtual MIMO algorithms.

Chapter 3 introduced novel subspace-based algorithms specifically designed for parameter estimation of multiple targets in bistatic MIMO radar systems. This approach leveraged a single fast time PN-code and N Hadamard codes of length N_s also referred to as slow time codes, achieving orthogonality between PRIs and sub-frames. The proposed algorithm utilised the concept of virtual array manifolds and effectively employed these slow time codes to further extend the array manifold from N to $N.N_s$. This innovative approach extended the observation space by a factor of N_s and enabled accurate estimation of key parameters like DOA, DOD, delay/range, and Doppler frequency. The approach also effectively overcomes the estimated parameters' association problem. Rigorous computer simulations validated the algorithm's effectiveness.

Chapter 4 introduced a novel subspace algorithm specifically designed for parameter estimation in bistatic MIMO radars. This algorithm integrated virtual spatiotemporal array manifold concepts to estimate multi-target parameters even in the presence of clutter and noise. Utilising $\overline{N}$ fast time PN-codes to achieve orthogonality within PRIs and provide Tx diversity, the algorithm aimed to estimate parameters including DOA, DOD, range, and Doppler. Drawing upon principles of array manifold extension, the observation space was extended from N to $N.\overline{N}.N_p\mathcal{N}_c$, where N_p is the number of pulse durations in one PRI and $\mathcal{N}_c$ is the length of the PN-codes. This transformation significantly expanded the observation space, potentially enabling the detection of numerous targets. Comprehensive Monte Carlo simulations were conducted to assess the effectiveness of the proposed algorithm, with RMSE used as a performance metric. The results clearly showed a significant improvement in the accuracy of estimated parameters compared to the conventional estimation method.

Chapter 5 investigated the theoretical performance limitations of antenna arrays used in previous chapters within the context of MIMO radar. This analysis focused on key aspects crucial for accurate target tracking and localisation, including the CRB and the Resolution threshold. Additionally, the concept of the "uncertainty sphere" was introduced to provide a foundational understanding of these theoretical bounds. The performance of Saab data sets A and B was compared to an equal-sized UCA. This comparison revealed that while the UCA maintains consistent performance across all directional ranges, the original arrays showed better performance near boresight but degraded performance at endfire. This behaviour aligns with the inherent characteristics of UCA and ULA geometries.

6.2 List of Contributions

Through extensive exploration and analysis in this thesis, several significant contributions have been made toward advancing MIMO radar technology, addressing system architectures, parameter estimation algorithms, and theoretical performance limitations. The key contributions are summarised as follows:

- Conducted a detailed study of Saab's experimental monostatic MIMO radar, performing comprehensive experiments to gain insights into its capabilities. Two experiments were conducted with low-altitude, small UAV targets, providing practical insights.

- Developed detailed models for Saab's experimental monostatic MIMO radar and its subsystems, enabling a deeper understanding and thorough analysis of the system.
- Analysed two distinct sets of radar data from these experiments, yielding valuable insights into the radar's real-world performance and behaviour under different conditions.
- Applied classical MIMO algorithms to the collected radar data, estimating key parameters such as Doppler, range, and directions. Performance comparisons showed that while most algorithms were effective, the LS algorithm performed the least reliably.
- Virtual algorithms were utilised, and their performance was compared with classical algorithms, demonstrating the effectiveness and advantages of virtual techniques. The virtual algorithms produced results that were highly consistent with each other and exhibited less variance compared to the classical approaches. Additionally, these algorithms successfully estimated the elevation angle for data Set-B due to the planar configuration of the virtual array.
- Proposed a novel algorithm for bistatic MIMO radars, leveraging slow time codes to expand the observation space and enhance estimation performance. RMSE tests indicated that this algorithm outperformed the standard subspace MUSIC algorithm.
- Proposed a second novel algorithm for bistatic MIMO radars, using fast time codes and virtual spatiotemporal array manifold concepts to significantly extend the observation space. RMSE tests confirmed that this algorithm outperformed both the standard subspace MUSIC and STC algorithms.
- Evaluated various array geometries used in this thesis and assessed their performance against theoretical lower bounds, offering insights into design

considerations and performance trade-offs. Results revealed that ULA arrays perform best around the boresight direction but degrade at endfire directions, as shown in both CRB and resolution threshold measures. By contrast, UCA arrays exhibited uniform performance across all directions.

6.3 Suggestions for Further Work

Moving forward, there are several avenues for further research that can build upon the findings of this thesis and contribute to the ongoing advancement of MIMO Radar systems:

- Expanding Algorithmic Exploration: Chapter 2 compared classical MIMO algorithms with virtual MIMO algorithms. Further research could extend this comparison by applying more advanced algorithms introduced in Chapters 3 and 4. This would provide deeper insights into the performance and capabilities of these algorithms in various scenarios.
- Optimization of Experimental Setup: The radar experiments conducted in this study utilised very long PN-codes and many Tx and Rx antennas/streams. Future experiments could explore designs with shorter PN-codes and fewer antennas/streams to demonstrate the efficacy of advanced algorithms with limited hardware resources.
- Early Consideration of Hardware Resources: Lessons learned from this research highlight the importance of setting up the MATLAB environment on hardware platforms with sufficient processing power, such as PCs with Nvidia GPUs or servers with cluster processing support, at an early stage of development. This proactive approach can prevent resource limitations encountered during late-stage algorithm implementation.
- Exploration of Bistatic and Multistatic Configurations: Future work could extend the investigation from monostatic to bistatic and multistatic MIMO radar configurations and architectures. This expansion would broaden the

scope of applicability and provide insights into the performance of MIMO radar systems in diverse operational scenarios.

- Validation of Advanced Algorithms: Applying the advanced algorithms presented in Chapters 3 and 4 to bistatic/multistatic MIMO radar actual data would validate their effectiveness and provide valuable insights into the accuracy of receive signal models proposed in this thesis. This validation process would contribute to enhancing confidence in the proposed algorithms and their applicability in real-world scenarios.

References

[1] M. I. Skolnik, *Introduction to Radar Systems*, 3rd ed. New York, NY, USA: McGraw-Hill, 2001.

[2] M. A. Richards, J. A. Scheer, W. A. Holm, E. Al., E. al., J. A. Scheer, W. A. Holm, E. Al., J. A. Scheer, and W. A. Holm, *Principles of Modern Radar: Basic Principles.* Institution of Engineering and Technology, Jan 2010.

[3] O. Blumtritt, "A Radar History of World War II: Technical and Military Imperatives (review)," *Technology and Culture*, vol. 42, pp. 372 – 373, 2001.

[4] M. Guarnieri, "The Early History of Radar [Historical]," *IEEE Industrial Electronics Magazine*, vol. 4, pp. 36–42, 2010.

[5] C. Hulsmeyer, "Radar in the Twentieth Century," *IEEE Aerospace and Electronic Systems Magazine*, vol. 15, pp. 27–46, 2000.

[6] H. Ng, M. Kucharski, W. Ahmad, and D. Kissinger, "Multi-Purpose Fully Differential 61- and 122-GHz Radar Transceivers for Scalable MIMO Sensor Platforms," *IEEE Journal of Solid-State Circuits*, vol. 52, pp. 2242–2255, 2017.

[7] D. K. Barton, *Radar System Analysis and Modeling.* Norwood, MA, USA: Artech House, 2004.

[8] S. Sun, A. Petropulu, and V. Poor, "MIMO Radar for Advanced Driver-Assistance Systems and Autonomous Driving: Advantages and Challenges," *IEEE Signal Processing Magazine*, vol. 37, pp. 98–117, 2020.

[9] S. Saponara, M. Greco, and F. Gini, "Radar-on-Chip/in-Package in Autonomous Driving Vehicles and Intelligent Transport Systems: Opportunities and Challenges," *IEEE Signal Processing Magazine*, vol. 36, pp. 71–84, 2019.

[10] "ETSI - Automotive Intelligent Transport | Intelligent Transport Systems (ITS)." [Online]. Available: https://www.etsi.org/technologies/automotive-intelligent-transport?jjj=1720978964046

[11] C. Waldschmidt, J. Hasch, and W. Menzel, "Automotive Radar ‚Äî From First Efforts to Future Systems," *IEEE Journal of Microwaves*, vol. 1, no. 1, pp. 135–148, 2021.

[12] Q. Lu, C. Liu, Y. Wang, S. Liu, Z. Zeng, X. Feng, and S. She, "Ground Penetrating Radar Applications in Mapping Underground Utilities," in *2018 17th International Conference on Ground Penetrating Radar (GPR)*, 2018, pp. 1–4.

[13] L. Miccinesi and M. Pieraccini, "Bridge Monitoring by a Monostatic/Bistatic Interferometric Radar Able to Retrieve the Dynamic 3D Displacement Vector," *IEEE Access*, vol. 8, pp. 210 339–210 346, 2020.

[14] F. Lombardi, H. D. Griffiths, M. Lualdi, and A. Balleri, "Characterization of the Internal Structure of Landmines Using Ground-Penetrating Radar," *IEEE Geoscience and Remote Sensing Letters*, vol. 18, no. 2, pp. 266–270, 2021.

[15] T. Jin, J. Lou, and Z. Zhou, "Extraction of Landmine Features Using a Forward-Looking Ground-Penetrating Radar With MIMO Array," *IEEE Transactions on Geoscience and Remote Sensing*, vol. 50, pp. 4135–4144, 2012.

[16] M. Garcia-Fernandez, Y. A. Lopez, and F. Andres, "Airborne Multi-Channel Ground Penetrating Radar for Improvised Explosive Devices and Landmine Detection," *IEEE Access*, vol. 8, pp. 165 927–165 943, 2020.

[17] J. Qian, Z. Liu, K. Wang, N. Fu, and J. Wang, "Transmission Design for Radar and Communication Spectrum Sharing Enhancement," *IEEE Transactions on Vehicular Technology*, vol. 72, pp. 2723–2727, 2023.

[18] F. Liu, C. Masouros, A. P. Petropulu, H. Griffiths, and L. Hanzo, "Joint Radar and Communication Design: Applications, State-of-the-Art, and the Road Ahead," *IEEE Transactions on Communications*, vol. 68, no. 6, pp. 3834–3862, 2020.

[19] X. Liu, T. Huang, Y. Liu, and J. Zhou, "Joint Transmit Beamforming for Multiuser MIMO Communications and MIMO Radar," *IEEE Transactions on Signal Processing*, vol. 68, pp. 3929–3944, 2019.

[20] M. A. Romeh, K. H. Moustafa, F. M. Ahmed, and W. Mehany, "A simple mimo radar architecture for drone detection," in *2024 14th International Conference on Electrical Engineering (ICEENG)*, 2024, pp. 187–189.

[21] T. Multerer, A. Ganis, U. Prechtel, E. Miralles, A. Meusling, J. Mietzner, M. Vossiek, M. Loghi, and V. Ziegler, "Low-cost jamming system against small drones using a 3D MIMO radar based tracking," *2017 European Radar Conference (EURAD)*, pp. 299–302, 2017.

[22] F. Yang, K. Qu, M. Hao, Q. Liu, X. Chen, and F. Xu, "Practical Investigation of a MIMO Radar System for Small Drones Detection," *2019 International Radar Conference (RADAR)*, pp. 1–5, 2019.

[23] J. M. Urco, J. Chau, T. Weber, J. Vierinen, and R. Volz, "Sparse Signal Recovery in MIMO Specular Meteor Radars With Waveform Diversity," *IEEE Transactions on Geoscience and Remote Sensing*, vol. 57, pp. 10 088–10 098, 2019.

[24] Q. Zhang, X. Wang, H. Liang, R. Li, Y. Dai, J. Liu, F. Li, and X. Liu, "Assumption and Discussion of Volume Scanning Strategy of New Generation Weather Radar in China I," in *2021 CIE International Conference on Radar (Radar)*, 2021, pp. 1153–1158.

[25] T. Matsuda and H. Hashiguchi, "DDMA-MIMO Observations With the MU Radar: Validation by Measuring a Beam Broadening Effect," *IEEE Journal of Selected Topics in Applied Earth Observations and Remote Sensing*, vol. 16, pp. 3083–3091, 2023.

[26] H. Griffiths and C. J. Baker, *An Introduction to Passive Radar*. Boston, MA, USA: Artech House, 2017.

[27] M. I. Skolnik, *Radar Handbook*, 3rd ed. New York, NY, USA: McGraw-Hill, 2008.

[28] M. A. Richards, *Fundamentals of Radar Signal Processing*, 2nd ed. New York, NY, USA: McGraw-Hill, 2014.

[29] V. C. Chen, *The Micro-Doppler Effect in Radar*. Boston, MA, USA: Artech House, 2011.

[30] F. Gini, A. De Maio, and L. Patton, *Waveform Design and Diversity for Advanced Radar Systems*. London, U.K.: IET, 2012.

[31] H. Ren and A. Manikas, "MIMO Radar With Array Manifold Extenders," *IEEE Transactions on Aerospace and Electronic Systems*, vol. 56, no. 3, pp. 1942–1954, Dec 2020.

[32] A. Manikas, *Beamforming: Sensor Signal Processing for Defence Applications*, 5th ed., ser. Communications and Signal Processing (London, England). London: Imperial College Press, 2015.

[33] N. Levanon, *Radar Principles*. Hoboken, NJ, USA: Wiley-Interscience, 1988.

[34] X. Li, X. Wang, Q. Yang, and S. Fu, "Signal Processing for TDM MIMO FMCW Millimeter-Wave Radar Sensors," *IEEE Access*, vol. 9, pp. 167 959–167 971, 2021.

[35] J. Li and P. Stoica, "MIMO Radar Diversity Means Superiority," *Book Chapter*, 2009.

[36] M. Akçakaya and A. Nehorai, "Adaptive MIMO Radar Design and Detection in Compound-Gaussian Clutter," *IEEE Transactions on Aerospace and Electronic Systems*, vol. 47, no. 4, pp. 2200–2207, 2011.

[37] ——, "MIMO radar detection and adaptive design in compound-Gaussian clutter," in *2010 IEEE Radar Conference*, 2010, pp. 236–241.

[38] M. Frankford, K. B. Stewart, N. Majurec, and J. Johnson, "Numerical and experimental studies of target detection with MIMO radar," *IEEE Transactions on Aerospace and Electronic Systems*, vol. 50, no. 4, pp. 1569–1577, 2014.

[39] C. Du, J. S. Thompson, and Y. Petillot, "Predicted Detection Performance of MIMO Radar," *IEEE Signal Processing Letters*, vol. 15, pp. 83–86, 2008.

[40] M. Schurwanz, S. Oettinghaus, J. Mietzner, and P. A. Hoeher, "Using Widely Separated MIMO Antennas for UAV Radar Direction-of-Arrival Estimation," in *2022 19th European Radar Conference (EuRAD)*, 2022, pp. 281–284.

[41] S. Gogineni and A. Nehorai, "Polarimetric MIMO Radar With Distributed Antennas for Target Detection," *IEEE Transactions on Signal Processing*, vol. 58, pp. 1689–1697, 2009.

[42] ——, "Monopulse MIMO Radar for Target Tracking," *IEEE Transactions on Aerospace and Electronic Systems*, vol. 47, pp. 755–768, 2011.

[43] H. Qian, "MIMO Radar Moving Target Detection in Homogeneous Clutter," *IEEE Transactions on Aerospace and Electronic Systems*, vol. 46, pp. 1290–1301, 2010.

[44] L. Cohen, "The generalization of the Wiener-Khinchin theorem," *ICASSP, IEEE International Conference on Acoustics, Speech and Signal Processing - Proceedings*, vol. 3, pp. 1577–1580, 1998.

[45] E. F. Knott, J. F. Shaeffer, and M. T. Tuley, *Radar Cross Section*, 2nd ed. The Institution of Engineering and Technology, 2004.

[46] C. Will, P. Vaishnav, A. Chakraborty, and A. Santra, "Human Target Detection, Tracking, and Classification Using 24-GHz FMCW Radar," *IEEE Sensors Journal*, vol. 19, pp. 7283–7299, 2019.

[47] R. Awadhiya and R. Vehmas, "Analyzing the Effective Coherent Integration Time for Space Surveillance Radar Processing," *2021 IEEE Radar Conference (RadarConf21)*, pp. 1–6, 2021.

[48] J. Lu, F. Liu, H. jun Liu, and Q. Liu, "Target Localization Based on High Resolution Mode of MIMO Radar with Widely Separated Antennas," *Remote. Sens.*, vol. 14, p. 902, 2022.

[49] Z. Tang and A. Manikas, "Multi Direction-of-Arrival Tracking Using Rigid and Flexible Antenna Arrays," *IEEE Transactions on Wireless Communications*, vol. 20, no. 11, pp. 7568–7580, 2021.

[50] M. Jabbarian and H. Khaleghi Bizaki, "Target tracking in pulse-Doppler MIMO radar by extended Kalman filter using velocity vector," in *20th Iranian Conference on Electrical Engineering (ICEE2012)*, 2012, pp. 1373–1378.

[51] Y. Liu and A. Manikas, "Location Tracking of Multiple Targets: an H,àû Approach," in *ICC 2022 - IEEE International Conference on Communications*, 2022, pp. 901–906.

[52] S. Gupta, P. Rai, A. Kumar, P. Yalavarthy, and L. R. Cenkeramaddi, "Target Classification by mmWave FMCW Radars Using Machine Learning on Range-Angle Images," *IEEE Sensors Journal*, vol. 21, pp. 19 993–20 001, 2021.

[53] A. Zyweck and R. Bogner, "Radar Target Classification of Commercial Aircraft," *IEEE Transactions on Aerospace and Electronic Systems*, vol. 32, pp. 598–606, 1996.

[54] I. Bilik, J. Tabrikian, and A. D. Cohen, "Gmm-based target classification for ground surveillance doppler radar," *IEEE Transactions on Aerospace and Electronic Systems*, vol. 42, pp. 267–278, 2006.

[55] M. J. Sagayaraj, V. Jithesh, and D. Roshani, "Comparative Study Between Deep Learning Techniques and Random Forest Approach for HRRP Based Radar Target Classification," in *2021 International Conference on Artificial Intelligence and Smart Systems (ICAIS)*, 2021, pp. 385–388.

[56] Q. J. O. Tan, R. A. Romero, and D. C. Jenn, "Target recognition with adaptive waveforms in cognitive radar using practical target RCS responses," in *2018 IEEE Radar Conference (RadarConf18)*, 2018, pp. 0606–0611.

[57] R. Haupt, *Antenna Arrays: A Computational Approach.* John Wiley & Sons, Ltd, 2010.

[58] J. Li and P. Stoica, "An Adaptive Filtering Approach to Spectral Estimation and SAR Imaging," *IEEE Transactions on Signal Processing*, vol. 44, no. 6, pp. 1469–1484, 1996.

[59] H. Van Trees, *Optimum Array Processing: Part IV of Detection, Estimation, and Modulation Theory*, ser. Detection, Estimation, and Modulation Theory. Wiley, 2004.

[60] A. Manikas, *Differential Geometry in Array Processing.* London, U.K.: Imperial College Press, Aug 2004.

[61] A. N. Atanasov, M. S. Oude Alink, and F. E. van Vliet, "A Figure of Merit for Simultaneous-Multi-Beam Transmit Antenna Arrays," *IEEE Transactions on Radar Systems*, 2023.

[62] M. Rivas-Costa and C. Mosquera, "Direction of Arrival Estimation with Hybrid Digital Analog Arrays: Algorithms and Ziv-Zakai Lower Bound," in *2023 57th Asilomar Conference on Signals, Systems, and Computers*, 2023, pp. 1329–1333.

[63] J. Wang, L. Bacharach, M. N. El Korso, and P. Larzabal, "Barankin Bound vs Cramér-Rao Bound for Interferometric-Like Array Design at Low SNR," in *2023 31st European Signal Processing Conference (EUSIPCO)*, 2023, pp. 1554–1558.

[64] C. A. Kokke, M. Coutino, R. Heusdens, and G. Leus, "Array Design Based on the Worst-Case Cramér-Rao Bound to Account for Multiple Targets," in *2023 57th Asilomar Conference on Signals, Systems, and Computers*, 2023, pp. 1174–1178.

[65] P. Gruner, M. Geiger, and C. Waldschmidt, "Ultracompact Monostatic MIMO Radar With Nonredundant Aperture," *IEEE Transactions on Microwave Theory and Techniques*, vol. 68, pp. 4805–4813, 2020.

[66] Y. Liu, B. Jiu, and H. Liu, "Clutter-based gain and phase calibration for monostatic MIMO radar with partly calibrated array," *Signal Process.*, vol. 158, pp. 219–226, 2019.

[67] X. Wang, W. Wang, J. Liu, X. Li, and J. Wang, "Fast communication: A sparse representation scheme for angle estimation in monostatic MIMO radar," *Signal Processing*, vol. 104, pp. 258–263, 2014.

[68] Y. Liu, N. Dar, and A. Manikas, "Multi-target Parameter Estimation in Bistatic MIMO Radar," *2022 IEEE International Symposium on Phased Array Systems and Technology (PAST)*, pp. 01–06, 2022.

[69] K. Luo and A. Manikas, "Joint Transmitter-Receiver Optimization in Multitarget MIMO Radar," *IEEE Transactions on Signal Processing*, vol. 65, no. 23, pp. 6292–6302, Dec 2017.

[70] ——, "Superresolution Multitarget Parameter Estimation in MIMO Radar," *IEEE Transactions on Geoscience and Remote Sensing*, vol. 51, no. 6, pp. 3683–3693, 2013.

[71] S. M. Stigler, "Gauss and the Invention of Least Squares," *https://doi.org/10.1214/aos/1176345451*, vol. 9, no. 3, pp. 465–474, May 1981.

[72] J. Capon, "High-Resolution Frequency-Wavenumber Spectrum Analysis," *Proceedings of the IEEE*, vol. 57, no. 8, pp. 1408–1418, 1969.

[73] P. Stoica and R. L. Moses, *Introduction to Spectral Analysis.* Prentice Hall, 1997.

[74] L. Xu, J. Li, and P. Stoica, "Target Detection and Parameter Estimation for MIMO Radar Systems," *IEEE Transactions on Aerospace and Electronic Systems*, vol. 44, no. 3, pp. 927–939, 2008.

[75] H. Commin, K. Luo, and A. Manikas, "Arrayed MIMO Radar: Multi-target Parameter Estimation for Beamforming," in *Beamforming - Sensor Signal Processing for Defence Applications.* Imperial College Press, London, Jan 2015, pp. 119–158.

[76] L. Xu, P. Stoica, and J. Li, "A Diagonal Growth Curve Model and Some Signal-processing Applications," *IEEE Transactions on Signal Processing*, vol. 54, no. 9, pp. 3363–3371, Sep 2006.

[77] W. Chen, K. M. Wong, and J. P. Reilly, "Detection of the Number of Signals: A Predicted Eigen-Threshold Approach," *IEEE Transactions on Signal Processing*, vol. 39, no. 5, pp. 1088–1098, 1991.

[78] G. Efstathopoulos and A. Manikas, "Extended Array Manifolds: Functions of Array Manifolds," *IEEE Transactions on Signal Processing*, vol. 59, no. 7, pp. 3272–3287, Jul 2011.

[79] H. Commin and A. Manikas, "Virtual SIMO Radar Modelling in Arrayed MIMO Radar," in *Sensor Signal Processing for Defence (SSPD 2012)*, vol. 2012, no. 3. IET, 2012.

[80] J. Li and P. Stoica, "MIMO Radar with Colocated Antennas," *IEEE Signal Process. Mag.*, vol. 24, no. 5, pp. 106–114, 2007.

[81] H. D. Griffiths, "New Directions in Bistatic Radar," in *Proc. IEEE Radar Conf.*, 2008, pp. 1–6.

[82] J. Li, G. Liao, and H. Griffiths, "Bistatic MIMO Radar Space-time Adaptive Processing," in *Proc. IEEE Radar Conf.*, 2011, pp. 498–502.

[83] H. Yan, J. Li, and G. Liao, "Multitarget Identification and Localization Using Bistatic MIMO Radar Systems," *EURASIP J. Adv. Signal Process.*, vol. 2008, 2007.

[84] B. Tang, J. Tang, Y. Zhang, and Z. Zheng, "Maximum Likelihood Estimation of DOD and DOA for Bistatic MIMO Radar," *Signal Process.*, vol. 93, no. 5, pp. 1349–1357, 2013.

[85] X. Zhang, L. Xu, L. Xu, and D. Xu, "Direction of Departure (DOD) and Direction of Arrival (DOA) Estimation in MIMO Radar with Reduced-Dimension MUSIC," *IEEE Commun. Lett.*, vol. 14, no. 12, pp. 1161–1163, 2010.

[86] F. K. W. Chan, H. C. So, L. Huang, and L.-t. Huang, "Parameter Estimation and Identifiability in Bistatic Multiple-input multiple-output Radar," *IEEE Trans. Aerosp. Electron. Syst.*, vol. 51, no. 3, pp. 2047–2056, 2015.

[87] B. Yao, W. Wang, and Q. Yin, "DOD and DOA Estimation in Bistatic Non-Uniform Multiple-Input Multiple-Output Radar Systems," *IEEE Commun. Lett.*, vol. 16, no. 11, pp. 1796–1799, 2012.

[88] Y. Jia, X. Zhong, Y. Guo, and W. Huo, "DOA and DOD Estimation Based on Bistatic MIMO Radar with Co-prime Array," in *Proc. IEEE Radar Conf.*, 2017, pp. 394–397.

[89] D. Nion and N. D. Sidiropoulos, "A PARAFAC-based Technique for Detection and Localization of Multiple Targets in a MIMO Radar System," in *Proc. IEEE Int. Conf. Acoust., Speech Signal Process.*, 2009, pp. 2077–2080.

[90] F. Xu, S. A. Vorobyov, and X. Yang, "Joint DOD and DOA Estimation in Slow-Time MIMO Radar via PARAFAC Decomposition," *IEEE Signal Process. Lett.*, vol. 27, pp. 1495–1499, 2020.

[91] W. L. Melvin and J. A. Scheer, "Principles of Modern Radar: Advanced Techniques," *Principles of Modern Radar: Advanced Techniques*, pp. 1–846, Jan 2013.

[92] M. Laid Bencheikh, Y. Wang, and H. He, "A Subspace-based Technique for Joint DOA-DOD Estimation in Bistatic MIMO Radar," in *4th Microwave and Radar Week MRW-2010 - 11th International Radar Symposium, IRS 2010 - Conference Proceedings*, 2010, pp. 170–173.

[93] F. Wen, J. Shi, and Z. Zhang, "Joint 2D-DOD, 2D-DOA, and Polarization Angles Estimation for Bistatic EMVS-MIMO Radar via PARAFAC Analysis," *IEEE Transactions on Vehicular Technology*, vol. 69, no. 2, pp. 1626–1638, Feb 2020.

[94] C. Cui, J. Xu, R. Gui, W. Q. Wang, and W. Wu, "Search-Free DOD, DOA and Range Estimation for Bistatic FDA-MIMO Radar," *IEEE Access*, vol. 6, pp. 15 431–15 445, Mar 2018.

[95] A. Sakhnini, A. Bourdoux, and S. Pollin, "Bistatic MIMO Radar with Unsynchronized Arrays," in *2023 IEEE Radar Conference (RadarConf23)*. Institute of Electrical and Electronics Engineers (IEEE), Jun 2023, pp. 1–5.

[96] Z. Tang and A. Manikas, "DOD-DOA Estimation using MIMO Antenna Arrays with Manifold Extenders," *2022 IEEE 33rd Annual International Symposium on Personal, Indoor and Mobile Radio Communications (PIMRC)*, pp. 535–540, Sep 2022.

[97] A. Manikas and M. Sethi, "A Space-time Channel Estimator and Single-user Receiver for Code-reuse DS-CDMA Systems," *IEEE Transactions on Signal Processing*, vol. 51, no. 1, pp. 39–51, 2003.

[98] T. Bendokat, R. Zimmermann, and P.-A. Absil, "A Grassmann Manifold Handbook: Basic Geometry and Computational Aspects," *Advances in Computational Mathematics*, vol. 50, no. 1, Jan 2024.

[99] J. Milnor and J. Stasheff, *Characteristic Classes*, ser. Annals of mathematics studies. Princeton University Press, 1974.

[100] J. Lee, *Introduction to Smooth Manifolds*, ser. Graduate Texts in Mathematics. Springer, 2003.

[101] A. Manikas, A. Alexiou, and H. R. Karimi, "Comparison of the Ultimate Direction-finding Capabilities of a Number of Planar Array Geometries," *IEE Proceedings: Radar, Sonar and Navigation*, vol. 144, no. 6, pp. 321–329, 1997.

[102] H. L. Van Trees, *Detection, Estimation, and Modulation Theory*, ser. Detection, Estimation, and Modulation Theory. Wiley, 1968, no. v. 1.

Imperial College London

Department of Electrical and Electronic Engineering